Ph.D. Dissertation

International Doctorate School in Information and Communication Technologies

DIT - University of Trento

Multi-Resolution Techniques based on Shape-Optimization for the Solution of Inverse Scattering Problems

Manuel Benedetti

Thesis in *co-tutelle* between University of Trento (Italy) and Université Paris Sud XI (France).
Thesis with European Label.

Advisor:
Andrea Massa, Professor
Università degli Studi di Trento
Co-Advisor:
Dominique Lesselier, Directeur de Recherche
Laboratoire des Signaux et Systèmes (Supélec-CNRS-UPS)

December 2008

Faculté des sciences d'Orsay

UNIVERSITÉ PARIS-SUD 11

Thèse de Doctorat

SPECIALITE: PHYSIQUE

Ecole Doctorale "Sciences et Technologies de l'Information des Télécommunications et des Systèmes"

Présentée par Manuel Benedetti

Sujet:

"Techniques Multi-Résolution basées sur l'Optimisation de Forme pour la Résolution de Problèmes Inverses de Diffraction"

Thèse en co-tutelle entre *Université de Paris Sud 11* (France) et *University of Trento* (Italie). Thèse avec le *label européen.*

Soutenue le 1er Decembre 2008 devant les membres du jury:

M. LESSELIER Dominique
M. MASSA Andrea
M. DORN Oliver
M. PICHOT Christian
M. PICHON Lionel
M. AZARO Renzo

Acknowledgements

Arriving at the end of my Ph.D., I would like to express my gratitude to all those who gave me the possibility of carrying out such a wonderful professional experience. First of all, I want to thank my thesis advisors Andrea Massa, Professor of Electromagnetic Fields at the University of Trento and Director of the Electromagnetic Diagnostic Laboratory (ELEDIA Lab.), and Dominique Lesselier, *Directeur de Recherche* at the *Laboratoire des Signaux et Systèmes* (L2S) of *Supélec*, who had confidence in my abilities as well as in the co-tutelle program in which I was involved.

My special thanks also go to my tutors Marc Labert, researcher at L2S, and Massimo Donelli, researcher at the University of Trento and member of the ELEDIA group. Certainly, I will never forget their helpfulness in providing me with so many theoretical suggestions as well as with useful tips at a more practical level.

Moreover, I want to thank all my dear colleagues and friends of the ELEDIA Research Group, whose skills and kindness contribute to make the Ph.D. a great professional experience and a wonderful life experience at the same time. I am deeply indebted to all of them, strictly in alphabetical order by name (I hope not to forget anybody), Andrea Rosani, Anna Martini, Aronne Casagranda, Davide Franceschini, Edoardo Zeni, Federico Caramanica, Federico Viani, Gabriele Franceschini, Giacomo Oliveri, Leonardo Lizzi, Luca Ioriatti, Luca Manica,

Mauro Martinelli, Paolo Rocca, Renzo Azaro, and Riccardo Aramini.

I also have to thank for the kindness the colleagues and friends that I met during my stays at L2S, to be more precise Andrea Cozza, Anthony Bourges, Arnaud Breard, Bernard Duchene, Chin Yuan Chong, Christophe Conessa, Cyril Dahon, Frédéric Brigui, Frédéric Nouguier, Houmam Moussa, Jean-Philippe Groby, Juan Felipe Abascal, Karim Louertani, Nicolas Ribiere-Tharaud, Tommy Gunnarsson, and Rami Kassab. A special thank goes to the administrative staff of the lab as well, namely Daniel Rouet and Maryvonne Giron.

Finally, I am infinitely grateful to my family, Stefano, Pierina, Susanna, and Micòl, whose patient love and ecouragements enabled me to finish this work.

Abstract

In the framework of inverse electromagnetic scattering techniques, the thesis focuses on the development and the analysis of the integration between a multi-resolution imaging procedure and a shape-optimization-based technique. The arising methodology allows, on one hand, to fully exploit the limited amount of information collectable from scattering measurements by means of the iterative multi-scaling approach (IMSA) which enables a detailed reconstruction only where needed without increasing the number of unknowns. On the other hand, the use of shape-optimization, such as the level-set-based minimization, provide an effective description of the class of targets to be retrieved by using "a-priori" information about the homogeneity of the scatterers. In order to assess strong points and drawbacks of such an hybrid approach when dealing with one or multiple scatterers, a numerical validation of the proposed implementations is carried out by processing both synthetic and laboratory-controlled scattering data.

Keywords
Microwave Imaging, Inverse Scattering, Level Sets, Iterative Multi-Scaling Approach, Homogeneous Dielectric Scatterers.

Résumé

La reconstruction non invasive de la position et de la forme d'objets inconnus constitue un thème de grand intérêt dans nombre d'applications, et on citera en particulier l'évaluation et le contrôle non destructif (généralement référés par les abréviations END et CND) pour la surveillance et le contrôle industriel et le diagnostic de sous-surface [1]. Dans un tel cadre intéressant, beaucoup de méthodologies ont été proposées, principalement basées sur les rayons X [2], les ultrasons [3], et les courants de Foucault [4]. Cependant, des approches dans le domaine microonde (*par lequel on entend de 300 MHz à 300 GHz*) ont été récemment reconnues comme offrant des méthodologies d'imagerie efficaces, grâce aux points clés suivants [1][5][8] :

- les ondes électromagnétiques aux fréquences microondes peuvent pénétrer matériaux naturels et artificiels sous réserve qu'ils ne soient pas des conducteurs idéaux ;

- les champs diffractés par le ou les objets cibles sont représentatifs non seulement des frontières de celui-ci ou ceux-ci, mais aussi de la ou des structures intérieures ;

- les microondes montrent une grande sensibilité au contenu en eau de la structure que l'on entreprend d'imager ;

- les sondes de ce domaine peuvent être employées sans aucun contact mécanique avec le spécimen testé .

De plus, en comparaison aux rayons X voire aux approches basées sur la résonance magnétique, les méthodes microondes minimisent (ou évitent) des effets collatéraux dans le spécimen testé. Donc, elles peuvent par exemple être mises en œuvre de manière plus sûre en imagerie biomédicale, en limitant entre autre le stress du patient dans la mesure où le contact physique avec le système d'imagerie peut être évité (e.g., le dépistage de cancers du sein [9]), ou dans d'autres applications critiques, telles que l'imagerie à travers les murs (dite Through-Wall Imaging ou TWI) [10].

Une avancée supplémentaire de l'inspection non invasive microonde est représentée par des approches de diffraction inverse qui sont destinées à construire une image de la région sous test qui contiennent de l'information quantitative bien définie [11]. La formulation mathématique du problème de diffraction inverse est présentée au chapitre 2 en se concentrant sur le cas où des informations a priori sur la géométrie sont effectivement disponibles. Puisque les problèmes de diffraction inverse n'ont généralement pas une solution sous une forme analytique, une résolution numérique basée sur la méthode des moments (MoM) est adoptée et les inconvénients principaux du modèle qui apparaissent, tels que la non linéarité, le mauvais conditionnement et la mauvaise localisation, sont discutés [12][13].

En particulier, la mauvaise localisation est causée par la perte d'information entre le problème inverse et le problème direct, alors que la non linéarité est due au fait que la solution ne peut pas être exprimée comme une somme linéaire d'éléments indépendants. Par suite de la mauvaise localisation, le problème inverse souffre également de mauvais conditionnement, puisque la solution ne dépend pas en continuité des données.

Afin de discuter les stratégies de résolution qui ont été développées pour surmonter de tels inconvénients, le chapitre 3 se concentre sur la situation actuelle dans le cadre de la diffraction inverse. En particulier, les solutions régularisées [38] consistent à exprimer quelques propriétés physiques prévues des diffracteurs au moyen de paramètres de régularisation, de ce fait construisant une famille de solutions approchées. Malheureusement, le choix du ou des paramètres de régularisation devient alors le thème principal, particulièrement dans le cas des problèmes non linéaires pour lesquels la littérature ne fournit aucun critère. De façon analogue, l'utilisation des approximations, telles que Born, Rayleigh et Rytov [13], est limitée à une classe spécifique des problèmes de diffraction inverse, c'est-à-dire traitant les diffracteurs de faibles contrastes.

À la différence des techniques et approximations de régularisation, les techniques de minimisation tentent de faire face à la non-linéarité du problème de diffraction inverse. Ces méthodologies reformulent le problème comme une procédure d'optimisation visant à la minimisation de l'écart entre les champs mesurés et la solution d'essai numériquement calculée. À cet effet, une fonction de coût appropriée est définie et l'espace de recherche est exploré au moyen de stratégies adaptées au problème ef-

fectif. Par conséquent, l'exactitude de la solution dépend de l'efficacité de la stratégie de solution, puisque le problème peut posséder des solutions erronées de par sa non-linéarité. Dans le cadre de stratégies de minimisation, la thèse décrit stratégies déterministes et heuristiques de minimisation. Les plus largement connues pour la première catégorie sont les méthodologies basées sur des minimisations par descente selon le gradient ainsi que présentées par Kleinman et al. [54]. Ces méthodologies sont basées sur la définition d'une série de solutions d'essai associées à des valeurs strictement décroissantes de la fonction de coût et elles sont caractérisées par la mise à jour du champ électrique inconnu ainsi que des valeurs des propriétés électromagnétiques (i.e., permittivité diélectrique et conductivité) dans le domaine de recherche. Malheureusement, la convergence de la minimisation déterministe dépend du point d'initialisation, puisque la solution peut être bloquée à des minima locaux par suite de la non-linéarité du problème. Au contraire, les techniques heuristiques peuvent limiter le probléme de minima locaux grâce à leur capacité d'explorer l'espace de recherche en totalité ainsi que à la possibilité d'inclure de l'information a priori dans la solution. Une telle classe de stratégies de minimisation se compose généralement d'algo-rithmes stochastiques inspirés du comportement d'insectes pour la mise à jour des inconnues.

Sans élaborer au delà du nécessaire à ce stade, le caractère mal posé est fortement lié à la quantité d'information que l'on peut collecter lors d'une expérience de diffraction à but d'imagerie, et habituellement le nombre de données indépendantes est plus faible que la dimension de l'espace des solutions;

des systèmes à vue multiple (on collecte le champ diffracté dans plusieurs directions ou sur plusieurs surfaces de l'espace environnant la zone étudiée) ou/et à illumination multiple (on éclaire cette zone d'étude de plusieurs directions ou à partir de sources réparties dans plusieurs domaines) sont donc généralement adoptés. Cependant, il est bien connu que l'information qui est effectivement accessible par ce ou ces moyens est une quantité qui connaît une limite supérieure [14][15]. En conséquence, il est nécessaire d'exploiter de manière efficace toute l'information contenue dans les échantillons recueillis du champ diffracté afin d'atteindre une reconstruction (d'obtenir une image) qui soit satisfaisante. Comme discuté dans le chapitre 3, afin d'exploiter effectivement toute l'information collectée à partir des mesures de diffraction effectuées, des stratégies dites de multi-résolution ont été récemment proposées. L'idée est de viser une résolution spatiale performante (c'est-à-dire améliorée par rapport à celle couramment choisie ou assurée dans la zone d'étude) seulement dans les régions d'intérêt (Regions of Interest dites RoIs) de l'espace où les diffracteurs inconnus sont localisés (plus précisément, où ils sont estimés être par le processus d'imagerie qui est mis en œuvre) [16] et/où des discontinuités entre matériaux apparaissent être présentes [17][18]. Quant aux réalisations pratiques, des stratégies déterministes ou impliquant des analyses statistiques des données ont été proposées afin de déterminer le niveau de résolution optimal, tandis que des approches impliquant des fonctions splines de degrés variés ont été employées afin d'améliorer le niveau de résolution. Par ailleurs, des approches multi-étapes ont été implémentées dans le but d'accroître de manière itéra-

tive la résolution spatiale au moyen d'une procédure analogue à celle d'un zoom [19] en gardant le rapport entre le nombre d'inconnues (e.g., les paramètres électromagnétiques de cellules avec lesquelles on considère que la zone d'étude est divisée) et le nombre de données (e.g., les échantillons recueillis du ou des champs diffractés) suffisamment faible et constant de telle façon que le risque de la survenue de minima locaux d'une fonctionnelle coût (qui traduit de manière usuelle l'écart entre les données et celles que l'on pourrait associer par la simulation numérique aux objets modélisés par la procédure d'inversion, et qui correspond au moins indirectement à la différence entre les objets réels et ceux qui nous apparaissent reconstruits) dans le problème d'optimisation tel que considéré [15].

Par ailleurs, l'absence d'information affectant la bonne résolution du problème inverse a été considérée, particulièrement en END-CND, à travers l'exploitation de la connaissance a priori que l'on peut avoir sur la scène de test, et du scénario de l'interaction électromagnétique mis en jeu, au moyen d'une représentation efficace des inconnues de celle-ci. En effet, dans beaucoup d'applications, le ou les objets inconnus sont caractérisés par des propriétés électromagnétiques connues (i.e., permittivité diélectrique et conductivité) et ils sont localisés dans une région hôte connue au moins à un certain degré (des incertitudes peuvent l'affecter, ceci menant à une complexité additionnelle qui pourrait être significative). De plus, cela dépendant de la précision recherchée, des scénarii plus complexes peuvent être approchés via l'introduction d'un ensemble de régions homogènes caractérisées par des paramètres géométriques (de forme) et électromagnétiques différents [20]. Sous de telles

hypothèses, un problème d'imagerie se réduit à un problème de reconstruction de forme, plus précisément un problème pour lequel ce sont les supports de ces régions homogènes qui doivent être reconstruits. Afin d'atteindre un tel but, des techniques paramétriques qui sont destinées à représenter l'objet inconnu en terme de paramètres descriptifs de formes de référence [21] [22], des approches plus sophistiquées telles que l'évolution contrôlée de courbes de type splines [23][25], des gradients de forme [26][28], ou des méthodes d'évolution d'ensembles de niveaux [31][32], ont été proposées. Plus en détail, quant aux stratégies d'optimisation de forme les plus importantes dans la formation d'images en microonde (le chapitre 4), des approches paramétriques sont basées sur la description des objets au moyen de formes de base qui sont correctement paramétrées. Pour ce qui concerne les méthodes d'ensembles de niveaux, le contour zéro d'un tel ensemble définit la frontière du ou des objets homogènes recherchés, ce qui, en contraste aux stratégies qui impliquent une description en pixels ou paramétriques, permet de représenter des formes complexes ou des régions d'une manière relativement simple (on parlera de méthodes d'inversion libres de contraintes topologie). De plus, à la différence des approches paramétriques, les ensembles de niveau permettent de contrôler la fusion et la division des objets d'une manière naturelle.

Dans le cadre brossé ci-dessus, la thèse se focalise sur le développement et l'analyse de l'intégration d'une stratégie multi-échelle itérative (dite Iterative Multi-Scaling Approach ou IMSA) [19] et de la représentation en ensembles de niveaux (Level-Sets ou LS) [33]. L'implémentation qui en résulte a pour but

d'exploiter de manière profitable tant la connaissance a priori disponible sur le scénario joué (e.g., l'homogé-néité du ou des diffracteurs en est le point clé) que le contenu informatif des mesures effectuées. Par raison de simplicité, et sans prétention à exhaustivité, la formulation du problème inverse est réduite au cas bidimensionnel de polarisation transverse magnétique (TM) quand on traitera d'une ou de plusieurs régions d'intérêt.

En particulier, l'architecture de la stratégie proposée est présentée au chapitre 4. La formulation mathématique de l'approche itérative multi-résolution avec la minimisation basée sur l'ensemble de niveaux (notée IMSA-LS) est concentrée sur l'architecture multi-étape. L'algorithme est basé sur des étapes où la résolution spatiale est itérativement augmentée en concentrant la région d'intérêt sur le secteur où l'objet est localisé. À la première étape, le domaine de recherche est discrétisé et une solution brute est recherchée. Puis, à partir de la première évaluation, la première région d'intérêt est estimée et le niveau de résolution est augmenté seulement à l'intérieur de la région d'intérêt. À cet effet, une nouvelle fonction multi-résolution d'ensemble des niveaux est définie et son évolution est menée en résolvant un problème adjoint qui correspond à la dérivation de la fonction de coût.

L'évaluation des possibilités de reconstruction d'IMSA-LS est effectuée premièrement en considérant des géométries simples, telles qu'un cylindre circulaire avec un rayon de la demi-longueur d'onde, et des données synthétiques. L'algorithme est initialisé avec la solution vraie afin de réaliser un essai de stabilité, puis des reconstructions sans et avec bruit sont effectuées.

Pendant de telles expériences, le comportement de la fonction multi-résolution d'ensemble des niveaux est également discuté. En outre, l'exécution proposée est comparée à l'approche dite "bare", c'est-à-dire la méthode standard. Généralement, l'IMSA-LS semble être plus précis particulièrement avec de faibles rapports signal à bruit. Les mêmes conclusions tiennent également en considérant des formes plus complexes, telles que le cylindre rectangulaire ou le cylindre creux. Pour mieux investiguer l'évaluation, des données acquises en situation contrôlée de laboratoire pour quelques géométries d'essai ont été aussi considérées. Dans de telles expériences, IMSA-LS et l'approche "bare" fournissent des résultats similaires en termes d'exactitude, puisque ces données sont probablement affectées par un faible niveau du bruit.

Le chapitre 5 se concentre sur un développement ultérieur de l'IMSA-LS, caractérisé par la possibilité de traiter des régions d'intérêt multiples, particulièrement pour reconstruire plusieurs objets de façon plus efficace en termes d'attribution des inconnues. Plus en détail, une telle stratégie, appelée IMSMRA-LS, est caractérisée par une architecture multi-étape, où à chaque niveau de résolution différentes régions d'intérêt sont prises en considération simultanément. À la première étape, un problème "bare" est résolu en choisissant le nombre de domaines selon la quantité d'information indépendante dans les données diffractées [14]. Puis, à partir des évaluations brutes des objets, les régions d'intérêt sont définies au moyen d'une stratégie adaptée à nos besoins, basée sur l'identification des contours des formes reconstruites. La résolution spatiale est augmentée dans ces régions en les discrétisant avec une frac-

tion des cellules qui ont été considérées à la premiére étape, afin de maintenir le nombre d'inconnues limité pendant la procédure d'inversion. La reconstruction multi-résolution est réitérée jusqu'à ce que les paramétres des régions d'intérêt, c'est-à-dire leurs barycentres et leurs dimensions, deviennent constants.

Le chapitre 5 discute également la performance de reconstruction de l'implémentation multi-région. Afin de comparer l'exactitude de la reconstruction fournie par IMSMRA-LS aux résultats de l'approche avec une seule région, une validation préliminaire prend en considération un diffracteur simple, tel qu'un cylindre circulaire avec un rayon de la demi-longueur d'onde, situé dans un domaine carré de côté deux longueurs d'onde. Dans une telle expérience, l'IMSMRA-LS s'avère plus efficace que l'IMSA-LS, particulièrement en raison de l'utilisation d'une stratégie de mise à jour de l'ensemble de niveaux plus appropriée. Après la discussion du choix des paramètres pour le critère d'arrêt, ce chapitre 5 propose quelques expériences numériques caractérisées par des diffracteurs multiples, tels que deux cylindres circulaires, deux rectangles, ou trois objets de différentes formes. Dans toutes ces expériences, l'IMSMRA-LS fournit une reconstruction légèrement plus précise que l'approche "bare", alors que l'exactitude des résultats de l'IMSA-LS est raisonnablement inférieure en raison de la résolution spatiale plus élevée. Cependant, en considérant des formes plus complexes, telles que les cylindres creux et des croix, aussi bien que des données bruitées, l'IMSMRA-LS surpasse l'approche "bare". La dernière illustration considérée a trait à la reconstruction réalisée en traitant des données expérimentales de laboratoire. La géométrie de référence se compose de deux

cylindres circulaires diélectriques. Comme dans la dernière expérience du chapitre 4, l'exécution proposée semble fournir des résultats tout à fait similaires à ceux de la méthode avec une seule région, puisque les données expérimentales sont caractérisées par des rapports signal à bruit élevés. Cependant, en ce qui concerne le dernier cas du chapitre 4, l'IMSMRA-LS semble être plus précis en estimant la forme des cibles.

En conclusion, ce travail propose l'intégration entre l'approche multi-échelle et une méthode d'ensemble de niveaux afin d'exploiter de manière profitable la quantité d'information obtenue via les mesures de la diffraction aussi bien que l'information disponible a priori sur le problème considéré. Deux réalisations sont présentées afin de traiter effectivement des configurations caractérisées par un ou plusieurs objets. Les éléments principaux de l'approche peuvent être récapitulés comme suit :

- représentation innovatrice multi-niveau des inconnues du problème dans la technique de reconstruction basée sur les ensembles de niveaux ;
- limitation du risque de blocage en des solutions erronées grâce au rapport réduit entre données et inconnues ;
- exploitation utile d'informations a priori (i.e., homogénéité d'objets) sur le scénario à l'essai ;
- résolution spatiale augmentée seulement dans les régions d'intérêt .

En outre, de la validation numérique et expérimentale proposée, les conclusions suivantes peuvent être tirées :

- l'IMSA-LS s'est habituellement avéré plus efficace que l'approche "bare", particulièrement en traitant des données bruitées diffractées par un objet de géométrie simple aussi bien que complexe ;

- l'IMSMRA-LS a semblé être aussi efficace que l'approche "bare" en traitant des géométries simples, alors qu'une architecture multi-région appropriée a amélioré l'exactitude de la reconstruction avec les diffuseurs multiples ;

- les stratégies intégrées (i.e., IMSA-LS et IMSMRA-LS) ont semblé nécessiter moins de calculs que l'approche standard, en atteignant une reconstruction possédant le même niveau de rêsolution spatiale dans la description de l'objet .

Published Journals Papers

A Two-Step Inverse Scattering Procedure for the Qualitative Imaging of Homogeneous Cracks in Known Host Media—Preliminary Results

Manuel Benedetti, Massimo Donelli, Dominique Lesselier, and Andrea Massa, *Member, IEEE*

***Abstract*—In the framework of nondestructive evaluation and testing, microwave inverse scattering approaches demonstrated their effectiveness and the feasibility of detecting unknown anomalies in dielectric materials. In this letter, an innovative technique is proposed in order to enhance their reconstruction accuracy. The approach is aimed at first estimating the region-of-interest (RoI) where the defect is supposed to be located and then at improving the qualitative imaging of the crack through a level-set-based shaping procedure. In order to assess the effectiveness of the proposed approach, representative numerical results concerned with different scenarios and blurred data are presented and discussed.**

***Index Terms*—Genetic algorithms, level set, microwave imaging, nondestructive testing and nondestructive evaluation (NDT/NDE).**

I. Introduction

NONDESTRUCTIVE testing and nondestructive evaluation (NDT/NDE) techniques are aimed at detecting unknown defects and other anomalies buried in known host objects by means of noninvasive methodologies [1]–[3]. In such a framework, electromagnetic inverse scattering approaches can play an important role. As an example, some approaches that approximate defective regions with rectangular shapes have been proposed [4], [5]. Despite the satisfactory results, such techniques are adequate when facing NDE/NDT problems where the retrieval of the positions and the rough estimation of the sizes of the defects are enough, but they cannot be reliably used when an accurate knowledge of the shapes of the defects is needed as in some industrial processes and usually in biomedical diagnosis. Notwithstanding, they are useful for providing a "first-step" information concerned with a rough localization of the defects to be further improved by means of a successive refinement reconstruction carried out with suitable contour detection methods.

Towards this end, this letter presents a two-step procedure aimed at improving the reconstruction of [4], [5]. More in detail, starting from the knowledge of the scattered field with and without the defect, the approximate problem in which the defect is assumed of simple shape (e.g., a rectangle) is reformulated in terms of an inverse scattering one and successively solved by means of the minimization of a suitably defined cost function [6]. After such a step, the region-of-interest (RoI) where the defect is supposed to be located is determined and the second retrieval phase takes place by applying a shape-based optimization technique based on the numerical evolution of a level-set function [7].

The outline of this letter is as follows. The mathematical formulation of the proposed approach is presented in Section II by focusing on the second step of the reconstruction procedure. Then, the effectiveness of the approach is discussed with reference to a set of representative numerical results in dealing with blurred measurement data (Section III). Finally, some conclusions follow (Section IV).

II. Mathematical Formulation

Let us consider a 2-D scenario where a homogeneous defect (or crack) characterized of unknown position $\underline{r}_c = (x_c, y_c)$ and shape Ω lies in a cylindrical host region D characterized by known relative permittivity ε_D and conductivity σ_D. The defective host medium is probed by V electromagnetic transverse magnetic (TM) plane waves with an incident field $\underline{E}^v_{\rm inc}(\underline{r}) = E^v_{\rm inc}(\underline{r})\hat{\underline{z}}$, and the induced electromagnetic field $\underline{E}^v_{\rm tot}(\underline{r})$ is given by

$$E^v_{\rm tot}(\underline{r}) = E^v_{\rm inc}(\underline{r}) + \iint_D \tau(\underline{r}')E^v_{{\rm tot}(c)}(\underline{r}')G_0(\underline{r}'/\underline{r})d\underline{r}' \quad (1)$$

where G_0 is the free-space Green's function and $\tau(\underline{r}) = \varepsilon(\underline{r}) - 1 - j(\sigma(\underline{r})/2\pi f\varepsilon_0)$ is the object function (f being the working frequency), or analogously, in a more "practical" expression [8]

$$E^v_{\rm tot}(\underline{r}) = E^v_{{\rm inc}(cf)}(\underline{r}) + \iint_\Omega \tau_\Omega(\underline{r}')E^v_{{\rm tot}(c)}(\underline{r}')G_1(\underline{r}'/\underline{r})d\underline{r}' \quad (2)$$

by considering the inhomogeneous Green's function $G_1(\underline{r}'/\underline{r})$ and the total electric field in the scenario without defects $E^v_{{\rm inc}(cf)}(\underline{r})$ defined as follows:

$$E^v_{{\rm inc}(cf)}(\underline{r}) = E^v_{\rm inc}(\underline{r}) + \iint_D \tau_D E^v_{{\rm inc}(cf)}(\underline{r}')G_0(\underline{r}'/\underline{r})d\underline{r}' \quad (3)$$

where $\tau_\Omega(\underline{r})$ is the differential object given by

$$\tau_\Omega(\underline{r}) = \begin{cases} (\varepsilon_C - \varepsilon_D) - j\dfrac{(\sigma_C - \sigma_D)}{2\pi f\varepsilon_0}, & \text{if } \underline{r} \in \Omega \\ 0, & \text{if } \underline{r} \notin \Omega \end{cases}. \quad (4)$$

Manuscript received July 16, 2007; revised October 9, 2007.

M. Benedetti, M. Donelli, and A. Massa are with the Department of Information and Communication Technology, University of Trento, 38050 Trento, Italy (e-mail: manuel.benedetti@dit.unitn.it; massimo.donelli@dit.unitn.it; andrea.massa@ing.unitin.it).

D. Lesselier is with the Département de Recherche en Électromagnétisme-Laboratoire des Signaux et Systèmes, CNRS-SUPELEC-UPS 11, 91192 Gif-sur-Yvette CEDEX, France (e-mail: dominique.lesselier@lss.supelec.fr).

Color versions of one or more of the figures in this letter are available online at http://ieeexplore.ieee.org.

Digital Object Identifier 10.1109/LAWP.2007.910954

With reference to the "differential formulation," the first step of the approach considers the partitioning of D in N_1 and the only one computation of the inhomogeneous Green's matrix $[G_1]$ of $N_1 \times N_1$ entries according to the procedure detailed in [8]. Then, the RoI R is modeled with a rectangular homogeneous shape described through the coordinates of the center $\underline{r}_R = (x_R, y_R)$, its length L_R, its side W_R, and the relative orientation θ_R. Accordingly, R turns out to be fully described by means of the following object function profile:

$$\tau_R(\underline{r}) = \begin{cases} \tau_\Omega(\underline{r}), & \text{if } X \in \left[-\dfrac{L_R}{2}, \dfrac{L_R}{2}\right] \\ & \text{and } Y \in \left[-\dfrac{W_R}{2}, \dfrac{W_R}{2}\right] \\ 0, & \text{otherwise} \end{cases} \tag{5}$$

where $X = (x - x_R)\cos\theta_R + (y - y_R)\sin\theta_R$ and $X = (x - x_R)\sin\theta_R + (y - y_R)\cos\theta_R$. Under these assumptions, the unknown array

$$\chi = \left[x_R, y_R, L_R, W_R, \theta_R, \left\{E^v_{\text{tot}(c)}(\underline{r}_P); p = 1, \ldots, P\right\}\right], \quad \underline{r}_P \in \Omega \tag{6}$$

is determined by solving the inverse scattering problem formulated in terms of an optimization one.

In detail, starting from the knowledge of the data samples collected in the observation domain O (i.e., the total field with the defect $E^v_{\text{tot}}(\underline{r}_m)$ and without the defect $E^v_{\text{tot}(cf)}(\underline{r}_m)$, $m = 1, \ldots, M$) and in the investigation domain D (i.e., $E^v_{\text{inc}}(\underline{r}_n)$, $n = 1, \ldots, N_1$), χ is obtained by minimizing the mismatching between estimated and measured scattering data evaluated through the computation of $\Theta_1(\chi)$, as shown in (7) at the bottom of the page. As far as the minimization process is concerned, Q trial solutions $\underline{\chi}^j = \{\chi^j_q, q = 1, \ldots, Q\}$ are randomly initialized ($j = 0$, j being the iteration index) and an iterative procedure takes place until a stopping criterion holds true ($j = J_{\max}$ or $\Theta_1(\chi_{\text{opt}}) < \gamma^1_{th}$, $\chi_{\text{opt}} = \arg\{\min_{q=1,\ldots,Q}[\min_{j=1,\ldots,J_{\max}} \Theta_1(\chi^j_q)]\}$). At each iteration, the following operations are performed:

1) the iteration index is updated ($j = j + 1$);
2) a set of genetic operators described in [5] is applied to $\underline{\chi}^{j-1}$ in order to generate the jth $[\underline{\chi}^j = \Im(\underline{\chi}^{j-1})]$;
3) the best trial solution achieved so far, $\chi^j_{\text{opt}} = \arg\{\min_{i=1,\ldots,j}[\Theta_1(\chi^i_{\text{opt}})]\}$ being $\chi^i_{\text{opt}} = \arg\{\min_{q=1,\ldots,Q}[\Theta_1(\chi^i_q)]\}$, is stored and its fitness evaluated $\Theta_1(\chi^j_{\text{opt}})$ in order to check the threshold condition for the stopping criterion.

At the end of the first step, the genetic algorithm (GA)-based optimization returns the array χ_{opt} that defines the RoI R

$$\chi_{\text{opt}} = \left[\hat{x}_R, \hat{y}_R, \hat{L}_R, \hat{W}_R, \hat{\theta}_R, \left\{\hat{E}^v_{\text{tot}(c)}(\underline{r}_P); p = 1, \ldots, P\right\}\right] \tag{8}$$

where the superscript $\hat{}$ denotes the estimated values.

The second step of the approach is aimed at refining the estimate of the defect starting from the knowledge coming from the first step (i.e., the homogeneous defect lies in R). Towards this purpose, a level-set-based strategy is employed. The algorithm is initialized by defining an elliptic trial shape Ψ_0 centered at $\hat{\underline{r}}_R$, with axes equal to $\hat{L}_R/2$ and $\hat{W}_R/2$, respectively, and rotated by $\hat{\theta}_R$. Then, the level set ϕ_0 is defined in Ω according to the rule based on the oriented distance function [9]. In particular, $\phi_0(\underline{r}_n)$ is equal to $\min_{\underline{r}_{\partial\Psi_0}} \|\underline{r}_{\partial\Psi_0} - \underline{r}_n\|$ if $\underline{r}_n \in \Psi_0$, and $-\min_{\underline{r}_{\partial\Psi_0}} \|\underline{r}_{\partial\Psi_0} - \underline{r}_n\|$ otherwise, $\underline{r}_{\partial\Psi_0}$ being a point belonging to the contour of Ψ_0 [7], [9]. Concerning the numerical implementation, Ω is discretized in N_2 cells and the following sequence is iteratively applied.

1) The accuracy of the current trial shape Ψ_k in retrieving the actual shape of the defect is evaluated by computing the value of the metric shown in (9) at the bottom of the page, where $\tau^k_\Gamma(\underline{r}_p)$ is the differential object function equal to $(\varepsilon_C - \varepsilon_D) - (j(\sigma_C - \sigma_D)/2\pi f\varepsilon_0)$ if $\phi_k(\underline{r}_p) \leq 0$ and 0

$$\Theta_1(\chi) = \left\{ \frac{\left| \sum_{v=1}^{V} \sum_{m=1}^{M} \left[E^v_{\text{tot}}(\underline{r}_m) - E^v_{\text{tot}(cf)}(\underline{r}_m) - \sum_{p=1}^{P} \tau_R(\underline{r}_p) E^v_{\text{tot}(c)}(\underline{r}_p) G_{1,R}(\underline{r}_m/\underline{r}_p) \right] \right|^2}{\left| \sum_{v=1}^{V} \sum_{m=1}^{M} [E^v_{\text{tot}}(\underline{r}_m) - E^v_{\text{inc}}(\underline{r}_m)] \right|^2} \right\} + \left\{ \frac{\left| \sum_{v=1}^{V} \sum_{n=1}^{N_1} \left[E^v_{\text{tot}(cf)}(\underline{r}_n) + E^v_{\text{tot}}(\underline{r}_n) - \sum_{p=1}^{P} \tau_R(\underline{r}_p) E^v_{\text{tot}(c)}(\underline{r}_p) G_{1,R}(\underline{r}_n/\underline{r}_p) \right] \right|^2}{\left| \sum_{v=1}^{V} \sum_{n=1}^{N_1} E^v_{\text{inc}}(\underline{r}_n) \right|^2} \right\} \tag{7}$$

$$\Theta_2\left(\tau^k_\Gamma\right) = \left\{ \frac{\left| \sum_{v=1}^{V} \sum_{m=1}^{M} \left[E^v_{\text{tot}}(\underline{r}_m) - E^v_{\text{tot}(cf)}(\underline{r}_m) - \sum_{p=1}^{N_2} \tau^k_\Gamma(\underline{r}_p) E^v_{\text{tot}(c)}(\underline{r}_p) G_{1,R}(\underline{r}_m/\underline{r}_p) \right] \right|^2}{\left| \sum_{v=1}^{V} \sum_{m=1}^{M} [E^v_{\text{tot}}(\underline{r}_m) - E^v_{\text{inc}}(\underline{r}_m)] \right|^2} \right\} \tag{9}$$

otherwise. Furthermore, $E^v_{\mathrm{tot}(cf)}(\underline{r}_m)$ is the solution of the following equation:

$$E^v_{\mathrm{tot}(cf)}(\underline{r}_m) = E^v_{\mathrm{inc}}(\underline{r}_m) + \sum_{n=1}^{N_1} \tau_D E^v_{\mathrm{tot}(cf)}(\underline{r}_n) G_0(\underline{r}_m/\underline{r}_n). \tag{10}$$

2) The level-set-based process ends if a fixed number of iteration is performed ($k < K_{\max}$) or $\Theta_2(\tau_k) < \gamma_{th}$ and Ψ_k^{opt} is assumed as the crack profile. Otherwise, the level set function ϕ_k is updated ($k = k+1$) by solving a Hamilton–Jacobi equation

$$\frac{\phi_{k+1}(\underline{r}_q) - \phi_k(\underline{r}_q)}{\Delta t} = -\aleph\left\{\nu_k(\underline{r}_n)\right\} H\left\{\phi_k(\underline{r}_q)\right\} \tag{11}$$

where $H\{\phi_k(\underline{r}_q)\}$ stands for the numerical counterpart of the Hamiltonian operator [9], [10] and Δt is the time-step parameter chosen according to the Courant–Friedrich–Leroy condition [11]. Moreover, $\nu_k(\underline{r}_n)$ is the velocity function determined by solving the adjoint problem as detailed in [7] and [9].

III. Numerical Analysis

This section is devoted to a numerical analysis of the proposed approach. A set of selected and representative numerical results related to a couple of experiments are reported and discussed for pointing out the improvement in the crack detection and shaping.

The first experiment (indicated as the "experiment A") considers an unknown void defect of elliptical cross section that lies in a square lossless host medium of side $L_D = 2.0\lambda$ and characterized by a dielectric permittivity equal to $\varepsilon_D = 2.0$. The defect is located at $\underline{r}_c = (11/30\lambda, 11/30\lambda)$ and rotated by $\pi/4$ with axes equal to $2/5\lambda$ and $11/50\lambda$, respectively. The scenario has been probed by $V = 30$ orthogonal and equally spaced angular directions and the field has been measured at $M = 30$ points. Moreover, the scattering data have been blurred with an additive noise of Gaussian-type characterized by a fixed signal-to-noise ratio (SNR).

Concerning the numerical procedure, D has been discretized in $N_1 = 289$ and Ω in $N_2 = 441$ subdomains.

As an example, Fig. 1(a) shows the reconstruction result from the two-step procedure in correspondence with SNR $= 10$ dB. As it can be observed, the support of the defect (whose actual perimeter is evidenced by the dotted line) belongs to the RoI R (dashed–dotted line) estimated at the end of the first step. However, the crack dimension is largely overestimated. On the contrary, the shape of the crack is more faithfully retrieved, despite the nonfavorable SNR. Such an event is quantitatively quantified by the value of the localization error $\delta_2 = 1.2\%$ [12] that improves by 30% with respect to the single-step inversion. For comparison purposes, Fig. 1(b) shows the reconstruction obtained by the "bare" level-set method setting $R \equiv D$ and discretizing the domain such that the spatial resolution is equal to that of Fig. 1(a). As it can be noticed, the reconstruction worsens.

As far as the area error Δ [12] is concerned, Fig. 2 shows the behavior of the error figure versus the SNR. As it can be noticed, the two-step approach turns out to be more robust than

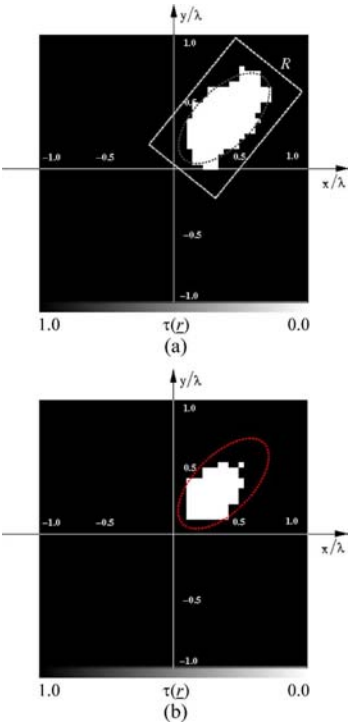

Fig. 1. Experiment A: (a) reconstruction after the first step (i.e., the RoI R) and dielectric distribution estimated at the end of the two-step procedure; (b) dielectric distribution estimated by means of the "bare" level set approach (i.e., $R \equiv D$).

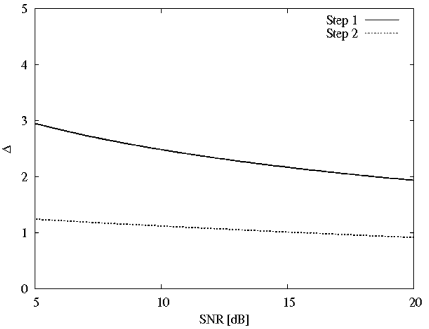

Fig. 2. Experiment A: area error versus SNR.

the blurring on data and the resulting performances are better in an amount between 150% and 100%.

The "experiment B" deals with a more complex cross-section shape of defect indicated by the dotted line in Fig. 3(a). As an example, let us analyze the case of SNR $= 20$ dB, when the profile reconstructed by the proposed method is shown in Fig. 3(a), while Fig. 3(b) gives the dielectric distribution estimated by the "bare" level set. Starting from the estimation of the

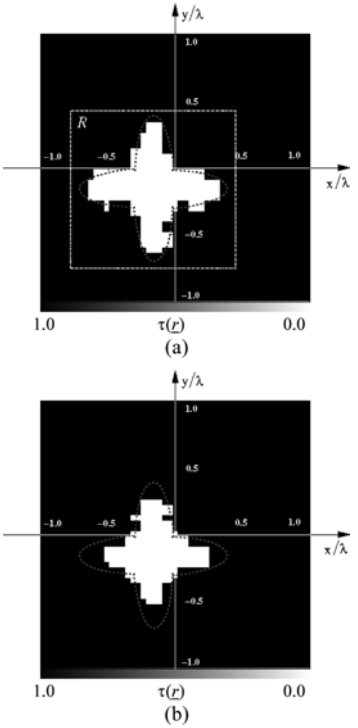

Fig. 3. Experiment B: (a) reconstruction after the first step (i.e., the RoI R) and dielectric distribution estimated at the end of the two-step procedure; (b) dielectric distribution estimated by means of the "bare" level-set approach (i.e., $R \equiv D$).

RoI, the two-step approach provides a satisfactory reconstruction improving both the localization error and the area error with respect to the first step ($\delta_1 = 1.5\%$, $\delta_2 = 0.5\%$; $\Delta_1 = 3.7\%$, $\Delta_2 = 1.5\%$). Similar considerations hold true when smaller SNRs are considered, as pointed out by the values of the area error pictorially reported in Fig. 4.

IV. Conclusion

In this letter, an innovative two-steps procedure for NDE/NDT applications has been proposed and preliminarily assessed. The method consists of a first step aimed at determining the region of interest where the defect is supposed to be located and a successive shaping process for enhancing the qualitative imaging. The approach has been evaluated by considering

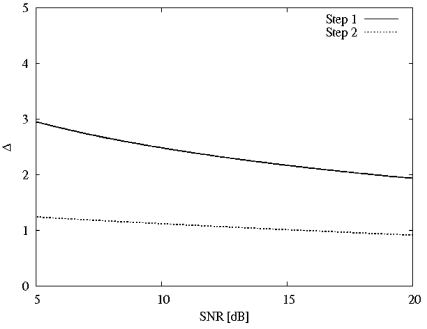

Fig. 4. Experiment B: area error versus SNR.

blurred synthetic data and different crack cross sections. The achieved results have pointed out the effectiveness of the approach, thus suggesting its future employment in biomedical imaging.

References

[1] P. J. Shull, *Nondestructive Evaluation: Theory, Techniques and Applications*. Boca Raton, FL: CRC Press, 2002.

[2] R. Zoughi, *Microwave Nondestructive Testing and Evaluation*. Amsterdam, The Netherlands: Kluwer, 2000.

[3] J. C. Bolomey, "Recent European developments in active microwave imaging for industrial, scientific and medical applications," *IEEE Trans. Microw. Theory Tech.*, vol. 37, no. 12, pp. 2109–2117, Dec. 1989.

[4] K. Meyer, K. J. Langenberg, and R. Schneider, "Microwave imaging of defects in solids," presented at the 21st Annu. Rev. Progr. Quantitative NDE, Snowmass Village, CO, Jul. 31–Aug. 5 1994.

[5] S. Caorsi, A. Massa, M. Pastorino, and M. Donelli, "Improved microwave imaging procedure for nondestructive evaluations of two-dimensional structures," *IEEE Trans. Antennas Propag.*, vol. 52, no. 6, pp. 1386–1397, Jun. 2004.

[6] Y. R. Samii and E. Michielssen, *Electromagnetic Optimization by Genetic Algorithms*. New York: Wiley, 1999.

[7] O. Dorn and D. Lesselier, "Level set methods for inverse scattering," *Inverse Problems*, vol. 22, pp. R67–R131, 2006.

[8] S. Caorsi, G. L. Gragnani, M. Pastorino, and M. Rebagliati, "A model-driven approach to microwave diagnostics in biomedical applications," *IEEE Trans. Microw. Theory Tech.*, vol. 44, no. 10, pt. 2, pp. 1910–1920, Oct. 1996.

[9] A. Litman, D. Lesselier, and F. Santosa, "Reconstruction of a two-dimensional binary obstacle by controlled evolution of a level-set," *Inverse Problem*, vol. 14, pp. 685–706, 1998.

[10] S. Osher and J. A. Sethian, "Fronts propagating with curvature-dependent speed: Algorithms based on Hamilton-Jacobi formulations," *J. Comp. Phys.*, vol. 79, pp. 12–49, 1988.

[11] J. A. Sethian, *Levelset Methods and Fast Marching Methods*, 2nd ed. Cambridge, U.K.: Cambridge Univ. Press, 1999, Monographs on Applied and Computational Mathematics.

[12] S. Caorsi, M. Donelli, and A. Massa, "Detection, location, and imaging of multiple scatterers by means of the iterative multi-scaling method," *IEEE Trans. Microw. Theory Tech.*, vol. 52, no. 4, pp. 1217–1228, Apr. 2004.

A Multi-Resolution Technique based on Shape Optimization for the Reconstruction of Homogeneous Dielectric Objects

M. Benedetti[1,2], D. Lesselier[2], M. Lambert[2], and A. Massa[1]

[1] Department of Information Engineering and Computer Science, *ELEDIA* Research Group, University of Trento, Via Sommarive 14, 38050 Trento - Italy, Tel. +39 0461 882057, Fax. +39 0461 882093

[2]Département de Recherche en Électromagnétisme - Laboratoire des Signaux et Systèmes, CNRS-SUPELEC Univ. Paris Sud 11, 3 rue Joliot-Curie, 91192 Gif-sur-Yvette CEDEX, France

E-mail: *manuel.benedetti@disi.unitn.it, lesselier@lss.supelec.fr, lambert@lss.supelec.fr, andrea.massa@ing.unitn.it*

Abstract. In the framework of inverse scattering techniques, this paper presents the integration of a multi-resolution technique and the level-set method for qualitative microwave imaging. On one hand, in order to effectively exploit the limited amount of information collectable from scattering measurements, the iterative multi-scaling approach (*IMSA*) is employed for enabling a detailed reconstruction only where needed without increasing the number of unknowns. On the other hand, the *a-priori* information on the homogeneity of the unknown object is exploited by adopting a shape-based optimization and representing the support of the scatterer via a level set function. Reliability and effectiveness of the proposed strategy are assessed by processing both synthetic and experimental scattering data for simple and complex geometries, as well.

Key Words **-** Microwave Imaging, Inverse Scattering, Level Sets, Iterative Multi-Scaling Approach, Homogeneous Dielectric Scatterers.

Classification Numbers (MSC) - 45Q05, 78A46, 78M50

1. Introduction

The non-invasive reconstruction of position and shape of unknown targets is a topic of great interest in many applications, such as non-destructive evaluation and testing (NDE/NDT) for industrial monitoring and subsurface sensing [1]. In this framework, many methodologies have been proposed based on x-rays [2], ultrasonics [3], and eddy currents [4]. Furthermore, microwave imaging has been recognized as a suitable methodology since [1][5]: (a) electromagnetic fields at microwave frequencies can penetrate non-ideal conductor materials; (b) the field scattered by the target is representative of its inner structure and not only of its boundary; (c) microwaves show a high sensibility to the water content of the structure under test; (d) microwave sensors can be employed without mechanical contacts with the specimen. In addition, compared to x-ray and magnetic resonance, microwave-based approaches minimize (or avoid) collateral effects in the specimen under test. Therefore, they can be safely employed in biomedical imaging.

A further advance in microwave non-invasive inspection is represented by inverse scattering approaches aimed at reconstructing a complete image of the region under test. Unfortunately, the underlying mathematical model is characterized by several drawbacks preventing their massive employment in NDE/NDT applications. In particular, inverse scattering problems are intrinsically ill-posed [6] as well as non-linear [7].

Since the ill-posedness is strongly related to the amount of collectable information and usually the number of independent data is lower than the dimension of the solution space, multi-view/multi-illumination systems are generally adopted. However, it is well known that the collectable information is an upper-bounded quantity [8]-[10]. Consequently, it is necessary to effectively exploit the overall information contained in the scattered field samples for achieving a satisfactory reconstruction.

Towards this end, multi-resolution strategies have been recently proposed. The idea is that of using an enhanced spatial resolution only in those regions where the unknown scatterers are found to be located. Accordingly, Miller *et al.* [11] proposed a statistically-based method for determining the optimal resolution level, while Baussard *et al.* [12] developed a strategy based on spline pyramids for sub-surface imaging problems. As for an example concerned with qualitative microwave imaging, Li *et al.* [13] implemented a multiscale technique based on Linear Sampling Method (LSM) to effectively reconstruct the contour of the scatterers. Unlike [11]-[13], the iterative multi-scale approach (IMSA)

developed by Caorsi *et al.* [14] performs a multi-step, multi-resolution inversion process in which the ratio between unknowns and data is kept suitably low and constant at each step of the inversion procedure, thus reducing the risk of occurrence of local minima [9] in the arising optimization problem.

On the other hand, the lack of information affecting the inverse problem has been addressed through the exploitation of the *a-priori* knowledge (when available) on the scenario under test by means of an effective representation of the unknowns. As far as many NDE/NDT applications are concerned, the unknown defect is characterized by known electromagnetic properties (i.e., dielectric permittivity and conductivity) and it lies within a known host region. Under these assumptions, the imaging problem reduces to a shape optimization problem aimed at the search of location and boundary contours of the defect. Parametric techniques aimed at representing the unknown object in terms of descriptive parameters of reference shapes [15][16] and more sophisticated approaches such as evolutionary-controlled spline curves [17][18], shape gradients [19]-[21] or level-sets [22]-[30] have then been proposed. As far as level-set-based methods are concerned, the homogeneous object is defined as the zero level of a continuous function and, unlike pixel-based or parametric-based strategies, such a description enables one to represent complex shapes in a simple way.

In order to exploit both the available *a-priori* knowledge on the scenario under test (e.g., the homogeneity of the scatterer) and the information content from the scattering measurements, this paper proposes the integration of the iterative multi-scaling strategy (*IMSA*) [14] and the level-set (*LS*) representation [23].

The paper is structured as follows. The integration between *IMSA* and *LS* is detailed in Sect. 2 dealing with a two-dimensional geometry. In Section 3, numerical testing and experimental validation are presented, a comparison with the standard *LS* implementation being made. Finally, some conclusions are drawn (Sect. 4).

2. Mathematical Formulation

Let us consider a cylindrical homogeneous non-magnetic object with relative permittivity ϵ_C and conductivity σ_C that occupies a region Υ belonging to an investigation domain D_I. Such a scatterer is probed by a set of V transverse-magnetic (TM) plane waves, with electric field directed along the axis of the cylindrical geometry,

namely $\underline{\zeta}^v(\underline{r}) = \zeta^v(\underline{r})\hat{\underline{z}}$ $(v = 1, \ldots, V)$, $\underline{r} = (x, y)$. The scattered field, $\underline{\xi}^v(\underline{r}) = \xi^v(\underline{r})\hat{\underline{z}}$, is collected at $M(v)$, $v = 1, ..., V$, measurement points $\underline{r}_m$ distributed in the observation domain D_O.

In order to electromagnetically describe the investigation domain D_I, let us define the contrast function $\tau(\underline{r})$ given by

$$\tau(\underline{r}) = \begin{cases} \tau_C & \underline{r} \in \Upsilon \\ 0 & \text{otherwise} \end{cases} \tag{1}$$

where $\tau_C = (\epsilon_C - 1) - j\frac{\sigma_C}{2\pi f \varepsilon_0}$, f being the frequency of operation (the time dependence $e^{j2\pi ft}$ being implied).

The scattering problem is described by the well-known Lippmann-Schwinger integral equations

$$\xi^v(\underline{r}_m) = \left(\frac{2\pi}{\lambda}\right)^2 \int_{D_I} \tau(\underline{r}') E^v(\underline{r}') G_{2D}(\underline{r}_m, \underline{r}')\, d\underline{r}', \quad \underline{r}_m \in D_O \tag{2}$$

$$\zeta^v(\underline{r}) = E^v(\underline{r}) - \left(\frac{2\pi}{\lambda}\right)^2 \int_{D_I} \tau(\underline{r}') E^v(\underline{r}') G_{2D}(\underline{r}, \underline{r}')\, d\underline{r}', \quad \underline{r} \in D_I \tag{3}$$

where λ is the background wavelength, E^v is the total electric field, and $G_{2D}(\underline{r}, \underline{r}') = -\frac{j}{4}H_0^{(2)}\left(\frac{2\pi}{\lambda}\|\underline{r} - \underline{r}'\|\right)$ is the free-space two-dimensional Green's function, $H_0^{(2)}$ being the second-kind, zeroth-order Hankel function.

In order to retrieve the unknown position and shape of the target Υ by step-by-step enhancing the spatial resolution only in that region, called region-of-interest (RoI), $R \in D_I$, where the scatterer is located [14], the following iterative procedure of S_{max} steps is carried out.

With reference to Fig. 1(a) and to the block diagram displayed in Fig. 2, at the first step ($s = 1$, s being the step number) a trial shape $\Upsilon_s = \Upsilon_1$, belonging to D_I, is chosen and the region of interest R_s [$R_{s=1} = D_I$] is partitioned into N_{IMSA} equal square sub-domains, where N_{IMSA} depends on the degrees of freedom of the problem at hand and it is computed according to the guidelines suggested in [9].

In addition, the level set function ϕ_s is initialized by means of a signed distance function defined as follows [23][25]:

$$\phi_s(\underline{r}) = \begin{cases} -\min_{b=1,\ldots,B_s} \|\underline{r} - \underline{r}_b\| & \text{if } \tau(\underline{r}) = \tau_C \\ \min_{b=1,\ldots,B_s} \|\underline{r} - \underline{r}_b\| & \text{if } \tau(\underline{r}) = 0 \end{cases} \tag{4}$$

where $\underline{r}_b = (x_b, y_b)$ is the b-th border-cell ($b = 1, \ldots, B_s$) of $\Upsilon_{s=1}$.

Then, at each step s of the process ($s = 1, ..., S_{max}$), the following optimization procedure is repeated (Fig. 2):

- ***Problem Unknown Representation*** - The contrast function is represented in terms of the level set function as follows

$$\widetilde{\tau}_{k_s}(\underline{r}) = \sum_{i=1}^{s} \sum_{n_i=1}^{N_{IMSA}} \tau_{k_i} \mathcal{B}\left(\underline{r}_{n_i}\right) \quad \underline{r} \in D_I \tag{5}$$

where the index k_s indicates the k-th iteration at the s-th step $[k_s = 1, ..., k_s^{opt}]$, $\mathcal{B}\left(\underline{r}_{n_i}\right)$ is a rectangular basis function whose support is the n-th sub-domain at the i-th resolution level $[n_i = 1, ..., N_{IMSA},\ i = 1, ..., s]$, and the coefficient τ_{k_i} is given by

$$\tau_{k_i} = \begin{cases} \tau_C & \text{if } \Psi_{k_i}\left(\underline{r}_{n_i}\right) \leq 0 \\ 0 & \text{otherwise} \end{cases} \tag{6}$$

letting

$$\Psi_{k_i}\left(\underline{r}_{n_i}\right) = \begin{cases} \phi_{k_i}\left(\underline{r}_{n_i}\right) & \text{if } i = s \\ \phi_{k_i^{opt}}\left(\underline{r}_{n_i}\right) & \text{if } (i < s) \text{ and } \left(\underline{r}_{n_i} \in R_i\right) \end{cases} \tag{7}$$

with $i = 1, ..., s$ as in (5).

- ***Field Distribution Updating*** - Once $\widetilde{\tau}_{k_s}(\underline{r})$ has been estimated, the electric field $E_{k_s}^v(\underline{r})$ is numerically computed according to a point-matching version of the Method of Moments (MoM) [31] as

$$\widetilde{E}_{k_i}^v\left(\underline{r}_{n_i}\right) = \textstyle\sum_{p_i=1}^{N_{IMSA}} \zeta^v\left(\underline{r}_{p_i}\right)\left[1 - \widetilde{\tau}_{k_i}\left(\underline{r}_{p_i}\right) G_{2D}\left(\underline{r}_{n_i}, \underline{r}_{p_i}\right)\right]^{-1}, \quad \underline{r}_{n_i}, \underline{r}_{p_i} \in D_I \quad n_i = 1, ..., N_{IMSA}\ . \tag{8}$$

- ***Cost Function Evaluation*** - Starting from the total electric field distribution (8), the reconstructed scattered field $\widetilde{\xi}_{k_s}^v(\underline{r}_m)$ at the m-th measurement point, $m = 1, ..., M(v)$, is updated by solving the following equation

$$\widetilde{\xi}_{k_s}^v(\underline{r}_m) = \sum_{i=1}^{s} \sum_{n_i=1}^{N_{IMSA}} \widetilde{\tau}_{k_i}\left(\underline{r}_{n_i}\right) \widetilde{E}_{k_i}^v\left(\underline{r}_{n_i}\right) G_{2D}\left(\underline{r}_m, \underline{r}_{n_i}\right) \tag{9}$$

and the fit between measured and reconstructed data is evaluated by the multi-resolution cost function Θ defined as

$$\Theta\left\{\phi_{k_s}\right\} = \frac{\sum_{v=1}^{V} \sum_{m=1}^{M(v)} \left|\widetilde{\xi}_{k_s}^v(\underline{r}_m) - \xi_{k_s}^v(\underline{r}_m)\right|^2}{\sum_{v=1}^{V} \sum_{m=1}^{M(v)} \left|\xi_{k_s}^v(\underline{r}_m)\right|^2}. \tag{10}$$

- ***Minimization Stopping*** - The iterative process stops [i.e., $k_s^{opt} = k_s$ and $\widetilde{\tau}_s^{opt} = \widetilde{\tau}_{k_s}$] when: (a) a set of conditions on the stability of the reconstruction holds true or (b) when the maximum number of iterations is reached $[k_s = K_{max}]$ or (c) when the

value of the cost function is smaller than a fixed threshold γ_{th}. As far as the stability of the reconstruction is concerned [condition (a)], the first corresponding stopping criterion is satisfied when, for a fixed number of iterations, K_τ, the maximum number of pixels which vary their value is smaller than a user defined threshold γ_τ according to the relationship

$$\max_{j=1,\ldots,K_\tau} \left\{ \sum_{n_s=1}^{N_{IMSA}} \frac{|\widetilde{\tau}_{k_s}(\underline{r}_{n_s}) - \widetilde{\tau}_{k_s-j}(\underline{r}_{n_s})|}{\tau_C} \right\} < \gamma_\tau \cdot N_{IMSA}. \tag{11}$$

The second criterion, about the stability of the reconstruction, is satisfied when the cost function becomes stationary within a window of K_Θ iterations as follows:

$$\frac{1}{K_\Theta} \sum_{j=1}^{K_\Theta} \frac{\Theta\{\phi_{k_s}\} - \Theta\{\phi_{k_s-j}\}}{\Theta\{\phi_{k_s}\}} < \gamma_\Theta. \tag{12}$$

K_Θ being a fixed number of iterations and γ_Θ being user-defined thresholds;. When the iterative process stops, the solution $\widetilde{\tau}_s^{opt}$ at the s-th step is selected as the one represented by the "best" level set function ϕ_s^{opt} defined as

$$\phi_s^{opt} = \arg\left[\min_{h=1,\ldots,k_s^{opt}} (\Theta\{\phi_h\})\right]. \tag{13}$$

- ***Iteration Update*** - The iteration index is updated $[k_s \rightarrow k_s + 1]$;
- ***Level Set Update*** - The level set is updated according to the following Hamilton-Jacobi relationship

$$\phi_{k_s}(\underline{r}_{n_s}) = \phi_{k_s-1}(\underline{r}_{n_s}) - \Delta t_s \mathcal{V}_{k_s-1}(\underline{r}_{n_s}) \mathcal{H}\{\phi_{k_s-1}(\underline{r}_{n_s})\} \tag{14}$$

where $\mathcal{H}\{\cdot\}$ is the Hamiltonian operator [32][33] given as

$$\mathcal{H}^2\{\phi_{k_s}(\underline{r}_{n_s})\} = \begin{cases} \max^2\left\{\mathcal{D}_{k_s}^{x-}; 0\right\} + \min^2\left\{\mathcal{D}_{k_s}^{x+}; 0\right\} + \\ \quad + \max^2\left\{\mathcal{D}_{k_s}^{y-}; 0\right\} + \min^2\left\{\mathcal{D}_{k_s}^{y+}; 0\right\} \\ \qquad \text{if } \mathcal{V}_{k(s)}\left(\underline{r}_{n(s)}\right) \geq 0 \\ \\ \min^2\left\{\mathcal{D}_{k_s}^{x-}; 0\right\} + \max^2\left\{\mathcal{D}_{k_s}^{x+}; 0\right\} + \\ \quad + \min^2\left\{\mathcal{D}_{k_s}^{y-}; 0\right\} + \max^2\left\{\mathcal{D}_{k_s}^{y+}; 0\right\} \\ \qquad \text{otherwise} \end{cases} \tag{15}$$

and $\mathcal{D}_{k_s}^{x\pm} = \frac{\pm\phi_{k_s}(x_{n_s}\pm1, y_{n_s}) \mp \phi_{k_s}(x_{n_s}, y_{n_s})}{l_s}$, $\mathcal{D}_{k_s}^{y\pm} = \frac{\pm\phi_{k_s}(x_{n_s}, y_{n_s}\pm1) \mp \phi_{k_s}(x_{n_s}, y_{n_s})}{l_s}$. Δt_s is the time-step chosen as $\Delta t_s = \Delta t_1 \frac{l_s}{l_1}$ with Δt_1 to be set heuristically according to the literature [23], l_s being the cell-side at the s-th resolution level. $\mathcal{V}_{k_s}$ is the velocity

function computed following the guidelines suggested in [23] by solving the adjoint problem of (8) in order to determine the adjoint field $\mathcal{F}^v_{k_s}$. Accordingly,

$$\mathcal{V}_{k_s}\left(\underline{r}_{n_s}\right) = -\Re\left\{\frac{\sum_{v=1}^{V}\tau_C E^v_{k_s}\left(\underline{r}_{n_s}\right)\mathcal{F}^v_{k_s}\left(\underline{r}_{n_s}\right)}{\sum_{v=1}^{V}\sum_{m=1}^{M(v)}\left|\xi^v_{k_s}\left(\underline{r}_m\right)\right|^2}\right\}, \qquad n_s = 1, ..., N_{IMSA} \tag{16}$$

where $\Re$ stands for the real part.

When the s-th minimization process terminates, the contrast function is updated $[\widetilde{\tau}^{opt}_s(\underline{r}) = \widetilde{\tau}_{k_{s-1}}(\underline{r}),\ \underline{r} \in D_I\ (5)]$ as well as the *RoI* $[R_s \rightarrow R_{s-1}]$. To do so, the following operations are carried out:

- ***Computation of the Barycenter of the RoI*** - the center of R_s of coordinates $(\widetilde{x}^c_s, \widetilde{y}^c_s)$ is determined by computing the center of mass of the reconstructed shapes as follows [14] [Fig. 1(b)]

$$\widetilde{x}^c_s = \frac{\int_{D_I} x\widetilde{\tau}^{opt}_s(\underline{r})\,\mathcal{B}(\underline{r})\,dx\,dy}{\int_{D_I}\widetilde{\tau}^{opt}_s(\underline{r})\,\mathcal{B}(\underline{r})\,dx\,dy} \tag{17}$$

$$\widetilde{y}^c_s = \frac{\int_{D_I} y\widetilde{\tau}^{opt}_s(\underline{r})\,\mathcal{B}(\underline{r})\,dx\,dy}{\int_{D_I}\widetilde{\tau}^{opt}_s(\underline{r})\,\mathcal{B}(\underline{r})\,dx\,dy}; \tag{18}$$

- ***Estimation of the Size of the RoI*** - the side L_s of R_s is computed by evaluating the maximum of the distance $\delta_c(\underline{r}) = \sqrt{(x-\widetilde{x}^c_s)^2 + (y-\widetilde{y}^c_s)^2}$ in order to enclose the scatterer, namely

$$\widetilde{L}_s = \max_{\underline{r}}\left\{2 \times \frac{\widetilde{\tau}^{opt}_s(\underline{r})}{\tau_C}\delta_c(\underline{r})\right\}. \tag{19}$$

Once the *RoI* has been identified, the level of resolution is enhanced $[k_s \rightarrow k_{s-1}]$ only in this region by discretizing R_s into N_{IMSA} sub-domains [Fig. 1(c)] and by repeating the minimization process until the synthetic zoom becomes stationary ($s = s_{opt}$), i.e.,

$$\left\{\frac{|Q_{s-1} - Q_s|}{|Q_{s-1}|} \times 100\right\} < \gamma_Q, \quad Q = \widetilde{x}^c, \widetilde{y}^c, \widetilde{L} \tag{20}$$

γ_Q being a threshold set as in [14], or until a maximum number of steps ($s_{opt} = S_{max}$) is reached.

At the end of the multi-step process ($s = s_{opt}$), the problem solution is obtained as $\widetilde{\tau}^{opt}\left(\underline{r}_{n_i}\right) = \widetilde{\tau}^{opt}_s\left(\underline{r}_{n_i}\right)$, $n_i = 1, ..., N_{IMSA}$, $i = 1, ..., s_{opt}$.

3. Numerical Validation

In order to assess the effectiveness of the *IMSA-LS* approach, a selected set of representative results concerned with both synthetic and experimental data is presented herein. The performances achieved are evaluated by means of the following error figures:

- *Localization Error* δ

$$\delta|_p = \frac{\sqrt{\left(\widetilde{x}_s^c|_p - x^c|_p\right)^2 - \left(\widetilde{y}_s^c|_p - y^c|_p\right)^2}}{\lambda} \times 100 \tag{21}$$

  where $\underline{r}_c|_p = \left(x^c|_p,\, y^c|_p\right)$ is the center of the p-th true scatterer, $p = 1, ..., P$, P being the number of objects. The average localization error $< \delta >$ is defined as

$$< \delta >= \frac{1}{P} \sum_{p=1}^{P} \delta|_p \,. \tag{22}$$

- *Area Estimation Error* Δ

$$\Delta = \left[\sum_{i=1}^{I} \frac{1}{N_{IMSA}} \sum_{n_i=1}^{N_{IMSA}} \mathcal{N}_{n_i} \right] \times 100 \tag{23}$$

  where $\mathcal{N}_{n_i}$ is equal to 1 if $\widetilde{\tau}^{opt}\left(\underline{r}_{n_i}\right) = \tau\left(\underline{r}_{n_i}\right)$ and 0 otherwise.

As far as the numerical experiments are concerned, the reconstructions have been performed by blurring the scattering data with an additive Gaussian noise characterized by a signal-to-noise-ratio (SNR)

$$SNR = 10\log \frac{\sum_{v=1}^{V} \sum_{m=1}^{M(v)} \left|\xi^v\left(\underline{r}_m\right)\right|^2}{\sum_{v=1}^{V} \sum_{m=1}^{M(v)} \left|\mu^{v,m}\right|^2} \tag{24}$$

$\mu^{v,m}$ being a complex Gaussian random variable with zero mean value.

3.1. Synthetic Data - Circular Cylinder

3.1.1. Preliminary Validation In the first experiment, a lossless circular off-centered scatterer of known permittivity $\epsilon_C = 1.8$ and radius $\rho = \lambda/4$ is located in a square investigation domain of side $L_D = \lambda$ [23]. $V = 10$ TM plane waves are impinging from the directions $\theta_v = 2\pi\,(v-1)/V$, $v = 1, ..., V$, and the scattering measurements are collected at $M = 10$ receivers uniformly distributed on a circle of radius $\rho_O = \lambda$.

As far as the initialization of the *IMSA-LS* algorithm is concerned, the initial trial object Υ_1 is a disk with radius $\lambda/4$ and centered in D_I. The initial value of the time step is set to $\Delta t_1 = 10^{-2}$ as in [23]. The *RoI* is discretized in $N_{IMSA} = 15 \times 15$ sub-domains at each step of the iterative multi-resolution process. Concerning the

stopping criteria, the following configuration of parameters has been selected according to a preliminary calibration dealing with simple known scatterers and noiseless data: $S_{max} = 4$ (maximum number of steps), $\gamma^{\widetilde{x}^c} = \gamma^{\widetilde{y}^c} = 0.01$ and $\gamma^{\widetilde{L}} = 0.05$ (multi-step process thresholds), $K_{max} = 500$ (maximum number of optimization iterations), $\gamma_\Theta = 0.2$ and $\gamma_\tau = 0.02$ (optimization thresholds), $K_\Theta = K_\tau = 0.15\,K_{max}$ (stability counters), and $\gamma_{th} = 10^{-5}$ (threshold on the cost function).

Figure 3 shows samples of reconstructions with the *IMSA-LS*. At the first step [Fig. 3(a) - $s = 1$], the scatterer is correctly located, but its shape is only roughly estimated. Thanks to the multi-resolution representation, the qualitative imaging of the scatterer is improved in the next step [Fig. 3(b) - $s = s_{opt} = 2$] as confirmed by the error indexes in Tab. 1. For comparison purposes, the profile retrieved by the single-resolution method [23] (indicated in the following as *Bare-LS*), when D_I has been discretized in $N_{Bare} = 31 \times 31$ equal sub-domains, is shown [Fig. 3(c)]. In general, the discretization of the *Bare-LS* has been chosen in order to achieve in the whole investigation domain a reconstruction with the same level of spatial resolution obtained by the *IMSA-LS* in the *RoI* at $s = s_{opt}$.

Although the final reconstructions [Figs. 3(b)(c)] achieved by the two approaches are similar and quite close to the true scatterer sampled at the spatial resolution of *Bare-LS* [Fig. 3(d)] and *IMSA-LS* [Fig. 3(b)], the *IMSA-LS* more faithfully retrieves the symmetry of the actual object, even though the reconstruction error appears to be larger than the one of the *Bare-LS* (Fig. 4). During the iterative procedure, the cost function $\Theta_{opt} = \Theta\left\{\phi_s^{opt}\right\}$ is initially characterized by a monotonically decreasing behavior. Then, $\Theta_{opt}\rfloor_{IMSA}$ becomes stationary until the stopping criterion defined by relationships (11) and (12) is satisfied (Fig. 4 - $s = 1$). Then, after the update of the field distribution inducing the error spike when $s = s_{opt} = 2$ and $k_s = 1$, $\Theta_{opt}\rfloor_{IMSA}$ settles to a value of 6.28×10^{-4} which is of the order of the *Bare-LS* error ($\Theta_{opt}\rfloor_{Bare} = 1.42 \times 10^{-4}$). Such a slight difference between $\Theta_{opt}\rfloor_{IMSA}$ and $\Theta_{opt}\rfloor_{Bare}$ depends on the different discretization [i.e., the basis functions $\mathcal{B}\left(\underline{r}_{n(i=2)}\right)$, $n(i) = 1, ..., N_{IMSA}$ are not the same as those of *Bare-LS*], but it does not affect the reconstruction in terms of both localization and area estimation, since $\delta\rfloor_{IMSA-LS} < \delta\rfloor_{Bare-LS}$ and $\Delta\rfloor_{IMSA-LS} < \Delta\rfloor_{Bare-LS}$ (Tab. 1).

Fig. 4 also shows that the multi-step multi-resolution strategy is characterized by a lower computational burden because of the smaller number of iterations for reaching the convergence (Fig. 4 - $k_{tot}\rfloor_{IMSA} = 125$ vs. $k_{tot}\rfloor_{Bare} = 177$, being k_{tot} the total number of iterations defined as $k_{tot} = \sum_{s=1}^{s_{opt}} k_s^{opt}$ for the *IMSA-LS*), and especially to the

reduced number of floating-point operations. As a matter of fact, since the complexity of the LS-based algorithms is of the order of $\mathcal{O}(2 \times \eta^3)$, $\eta = N_{IMSA}$, N_{Bare} (i.e., the solution of two direct problems is necessary for computing an estimate of the scattered field and for updating the velocity vector), the computational cost of the *IMSA-LS* at each iteration is two orders in magnitude smaller than that of the *Bare-LS*.

3.1.2. Noisy Data As for the stability of the proposed approach, Figure 5 shows the reconstructions with the *IMSA-LS* [Figs. $5(a)(c)(e)$] compared to those of the *Bare-LS* [Figs. $5(b)(d)(f)$] with different levels of additive noise on the scattered data [$SNR = 20\,dB$ (top); $SNR = 10\,dB$ $(middle)$; $SNR = 5\,dB$ $(bottom)$]. As expected, when the SNR decreases, the performances worsen. However, as outlined by the behavior of the error figures in Tab. 2, blurred data and/or noisy conditions affect more evidently the *Bare* implementation than the multi-resolution approach. For completeness, the behavior of $\Theta_{opt}\rfloor_{IMSA}$ versus the iteration index is reported in Fig. 6 for different levels of SNR. As it can be noticed, the value of the error at the end of the iterative procedure decreases as the SNR increases.

In the second experiment, the same circular scatterer, but centered at a different position within a larger investigation square of side $L_D = 2\lambda$ ($\rho_O = 2\lambda$), has been reconstructed. According to [9], $M = 20$; $v = 1, ..., V$ receivers and $V = 20$ views are considered and D_I is discretized in $N_{IMSA} = 13 \times 13$ pixels.

Figure $7(a)$ shows the reconstruction obtained at the convergence ($s_{opt} = 3$) by *IMSA-LS* when $SNR = 5\,dB$. The result reached by the *Bare-LS* ($N_{BARE} = 47 \times 47$) is reported in Fig. $7(b)$ as well. As it can be noticed, the multi-resolution inversion is characterized by a better estimation of the object center and shape as confirmed by the values of δ and Δ ($\delta\rfloor_{IMSA-LS} = 0.59$ vs. $\delta\rfloor_{Bare-LS} = 2.72$ and $\Delta\rfloor_{IMSA-LS} = 0.48$ vs. $\Delta\rfloor_{Bare-LS} = 0.64$). As for the computational load, the same conclusions from previous experiments hold true.

3.2. Synthetic Data - Rectangular Scatterer

The second test case deals with a more complex scattering configuration. A rectangular off-centered scatterer ($L = 0.27\lambda$ and $W = 0.13\lambda$) characterized by a dielectric permittivity $\epsilon_C = 1.8$ is located within an investigation domain of $L_D = 3\lambda$ as indicated by the red dashed line in Fig. 8. In such a case, the imaging setup is made up of $V = 30$ sources and $M = 30$ measurement points for each view v [9]. D_I is partitioned into

$N_{IMSA} = 19 \times 19$ sub-domains (while $N_{Bare} = 33 \times 33$) and Δt_1 is set to 0.06.

3.2.1. Validation of the Stopping Criteria Before discussing the reconstruction capabilities, let us show a result concerned with the behavior of the proposed approach when varying the user-defined thresholds (γ_Θ, γ_τ, $\gamma_{\widetilde{x}^c}$, $\gamma_{\widetilde{y}^c}$, $\gamma_{\widetilde{L}}$) of the stopping criteria. Figure 8 displays the reconstructions achieved by using the sets of parameters given in Tab. 3 [Γ_1 - Fig. 8(a); Γ_2 - Fig. 8(b); Γ_3 - Fig. 8(c); Γ_4 - Fig. 8(d)] while the behaviors of the cost function are depicted in Fig. 9. As it can be noticed, the total number of iterations k_{tot} increases as the values of the thresholds γ_Θ and γ_τ decrease. However, in spite of a larger k_{tot}, using lower threshold values does not provide better results, as shown by the comparison between settings Γ_2 and Γ_4 [Figs. 8(b)-(d), and Fig. 9]. The sets of parameters characterized by $\gamma_\Theta = 0.2$ and $\gamma_\tau = 0.02$ provide a good trade-off between the arising computational burden and the quality of the reconstructions. As far as the stopping criterion of the multi-resolution procedure is concerned, Figure 9 also shows two different behaviors of the cost function when using Γ_2 and Γ_3 (letting $\gamma_\Theta = 0.2$ and $\gamma_\tau = 0.02$). In particular, the proposed approach stops at $s_{opt} = 3$, instead of $s_{opt} = 4$, when increasing by a degree of magnitude the values of $\gamma_{\widetilde{x}^c}$, $\gamma_{\widetilde{y}^c}$, and $\gamma_{\widetilde{L}}$. Although with a heavier computational burden, the choice $\gamma_{\widetilde{x}^c} = \gamma_{\widetilde{y}^c} = 0.01$ and $\gamma_{\widetilde{L}} = 0.05$ results more effective [see Fig. 8(b) vs. Fig. 8(c)].

3.2.2. Noisy Data Figures 10-12 and Table 4 show the results from the comparative study carried out in correspondence with different values of signal-to-noise ratio [$SNR = 20\,dB$ - Fig. 10(a) vs. Fig. 10(b); $SNR = 10\,dB$ - Fig. 10(c) vs. Fig. 10(d); $SNR = 5\,dB$ - Fig. 10(e) vs. Fig. 10(f)]. They further confirm the reliability and efficiency of the multi-resolution strategy in terms of qualitative reconstruction errors (Fig. 11), especially when the noise level grows. In particular, the *Bare* implementation does not yield either the position or the shape of the rectangular scatterer when $SNR = 5\,dB$, whereas the *IMSA-LS* properly retrieves both the barycenter and the contour of the target. As for the computational cost, it should be noticed that although the *IMSA-LS* requires a greater number of iterations for reaching the convergence (Fig. 12, Tab. 4), the total amount of complex floating-point operations, $f_{pos} = \mathcal{O}(2 \times \eta^3) \times k_{tot}$, usually results smaller (Tab. 4).

3.3. Numerical Data - Hollow Cylinder

The third test case is concerned with the inversion of the data scattered by a higher permittivity ($\epsilon_C = 2.5$) off-centered cylindrical ring, letting $L_D = 3\lambda$. The external radius of the ring is $\rho_{ext} = \frac{2}{3}\lambda$, and the internal one is $\rho_{int} = \frac{\lambda}{3}$. By assuming the same arrangement of emitters and receivers as in Section 3.2, the investigation domain is discretized with $N_{IMSA} = 19 \times 19$ and $N_{Bare} = 35 \times 35$ square cells for the *IMSA-LS* and the *Bare-LS*, respectively. Moreover, Δt_1 is initialized to 0.003.

As it can be observed from Fig. 13, where the profiles when $SNR = 20\,dB$ [Figs. 13$(a)(b)$] and $SNR = 10\,dB$ [Figs. 13$(c)(d)$] reconstructed by means of the *IMSA-LS* [Figs. 13$(a)(c)$] and the *Bare-LS* [Figs. 13$(b)(d)$] are shown, the integrated strategy usually overcomes the standard one both in locating the object and in estimating the shape. In particular, when $SNR = 20\,dB$, the distribution in Fig. 13(a) is a faithful estimate of the scatterer under test ($\delta\rfloor_{IMSA-LS} = 1.25$ and $\Delta\rfloor_{IMSA-LS} = 3.13$). On the contrary, the reconstruction with the *Bare-LS* is very poor ($\delta\rfloor_{Bare-LS} = 65.2$ and $\Delta\rfloor_{Bare-LS} = 34.39$). Certainly, a smaller SNR value impairs the inversion as shown in Fig. 13(c) [compared to Fig. 13(a)]. However, in this case, the *IMSA-LS* is able to properly locate the object ($\delta\rfloor_{IMSA-LS} = 1.7$ vs. $\delta\rfloor_{Bare-LS} = 65.9$) giving rough but useful indications about its shape ($\Delta\rfloor_{IMSA-LS} = 7.6$ vs. $\Delta\rfloor_{Bare-LS} = 34.55$).

3.4. Synthetic Data - Multiple Scatterers

The last synthetic test case is aimed at illustrating the behavior of the *IMSA-LS* when dealing with $P = 3$ scatterers ($\epsilon_C = 2.0$) distanced from one another. The test geometry is characterized by an elliptic off-centered cylinder, a circular off-centered scatterer, and a square off-centered object located in a square investigation domain characterized by $L_D = 3\lambda$. By adopting the same arrangement of emitters and receivers as in Section 3.3, the investigation domain is discretized with $N_{IMSA} = 23 \times 23$ and $N_{Bare} = 31 \times 31$ square cells for the *IMSA-LS* and the *Bare-LS*, respectively. Moreover, Δt_1 is set to 0.03.

Figures 14 and 15 show the results from the comparative study carried out in correspondence with different values of signal-to-noise ratio. As shown by the reconstructions (Fig. 14) and as expected, the multi-resolution approach provides more accurate results and appears to be more reliable than the *Bare-LS* especially with low SNR. This conclusion is further confirmed by the behavior of the reconstruction errors

(Fig. 15), for which the *IMSA-LS* achieves a lower localization error as well as a lower area error than those of *Bare-LS,* especially for $SNR = 5\,dB$. On the other hand, both algorithms provide good estimates of the scatterer under test when inverting data affected by low noise [$SNR = 20\,dB$ - Fig. 14(a) vs. Fig. 14(b); Fig. 15(a) and (b)].

3.5. Laboratory-Controlled Data

In order to further assess the effectiveness of the *IMSA-LS* also in dealing with experimental data, the multiple-frequency angular-diversity bi-static benchmark provided by *Institut Fresnel* in Marseille (France) has been considered. With reference to the experimental setup described in [34], the dataset "*dielTM_dec8f.exp*" has been processed. The field samples [$M = 49$, $V = 36$] are related to an off-centered homogeneous circular cylinder $\rho = 15\,\mathrm{mm}$ in diameter, characterized by a nominal value of the object function equal to $\tau(\underline{r}) = 2.0 \pm 0.3$, and located at $x_c = 0.0$, $y_c = -30\,\mathrm{mm}$ within an investigation domain assumed in the following of square geometry and extension $20 \times 20\,\mathrm{cm}^2$.

By setting $\epsilon_C = 3.0$, the reconstructions achieved are shown in Fig. 16 (*left column*) compared to those from the standard *LS* (*right column*) at $F = 4$ different operation frequencies. Whatever the frequency, the unknown scatterer is accurately localized and both algorithms yield, at convergence, structures that occupy a large subset of the true object. Such a similarity of performances, usually verified in synthetic experiments when the value of SNR is greater than $20\,dB$, seems to confirm the hypothesis of a low-noise environment as already evidenced in [35].

Finally, also in dealing with experimental datasets, the *IMSA-LS* proves its efficiency since the overall amount of complex floating point operations still remains two orders in magnitude lower than the one of the *Bare-LS* (Tab. 5 - Fig. 17).

4. Conclusions

In this paper, a multi-resolution approach for qualitative imaging purposes based on shape optimization has been presented. The proposed approach integrates the multi-scale strategy and the level set representation of the problem unknowns in order to profitably exploit the amount of information collectable from the scattering experiments as well as the available *a-priori* information on the scatterer under test.

The main key features of such a technique can be summarized as follows:

- innovative multi-level representation of the problem unknowns in the shape-deformation-based reconstruction technique;
- effective exploitation of the scattering data through the iterative multi-step strategy;
- limitation of the risk of being trapped in false solutions thanks to the reduced ratio between data and unknowns;
- useful exploitation of the *a-priori* information (i.e., object homogeneity) about the scenario under test;
- enhanced spatial resolution limited to the region of interest.

From the validation concerned with different scenarios and both synthetic and experimental data, the following conclusions can be drawn:

- the *IMSA-LS* usually proved more effective than the single-resolution implementation, especially when dealing with corrupted data scattered from simple as well as complex geometries characterized by one or several objects;
- the integrated strategy appeared less computationally-expensive than the standard approach in reaching a reconstruction with the same level of spatial resolution within the support of the object.

References

[1] P. J. Shull, *Nondestructive Evaluation: Theory, Techniques and Applications*. CRC Press, 2002.

[2] J. Baruchel, J.-Y. Buffière, E. Maire, P. Merle, and G. Peix, *X-Ray Tomography in Material Science*. Hermes Science, 2000.

[3] L. W. Schmerr, *Fundamentals of Ultrasonic Nondestructive Evaluation: A Modeling Approach*. Springer, 1998.

[4] B. A. Auld and J. C. Moulder, "Review of advances in quantitative eddy current nondestructive evaluation", *J. Nondestructive Evaluation*, vol. 18, no. 1, pp. 3-36, Mar. 1999.

[5] R. Zoughi, *Microwave Nondestructive Testing and Evaluation*. Dordrecht, The Netherlands: Kluwer Academic Publishers, 2000.

[6] O. M. Bucci and T. Isernia, "Electromagnetic inverse scattering: retrievable information and measurement strategies," *Radio Sci.*, vol. 32, pp. 2123-2138, Nov.-Dec. 1997.

[7] M. Bertero and P. Boccacci, *Introduction to Inverse Problems in Imaging*. IOP Publishing Ltd, Bristol, 1998.

[8] O. M. Bucci and G. Franceschetti, "On the spatial bandwidth of scattered fields," *IEEE Trans. Antennas Propagat.*, vol. 35, no. 12, pp. 1445-1455, Dec. 1987.

[9] T. Isernia, V. Pascazio, and R. Pierri, "On the local minima in a tomographic imaging technique," *IEEE Trans. Antennas Propagat.*, vol. 39, no. 7, pp. 1696-1607, Jul. 2001.

[10] H. Haddar, S. Kusiak, and J. Sylvester, "The convex back-scattering support," *SIAM J. Appl. Math.*, vol. 66, pp. 591-615, Dec. 2005.

[11] E. L. Miller, and A. S. Willsky, "A multiscale, statistically based inversion scheme for linearized inverse scattering problems," *IEEE Trans. Antennas Propagat.*, vol. 34, no. 2, pp. 346-357, Mar. 1996.

[12] A. Baussard, E. L. Miller, and D. Lesselier, "Adaptive muliscale reconstruction of buried objects," *Inverse Problems*, vol. 20, pp. S1-S15, Dec. 2004.

[13] J. Li, H. Liu, and J. Zou, "Multilevel linear sampling method for inverse scattering problems," *SIAM J. Appl. Math.*, vol. 30, pp. 1228-1250, Mar. 2008.

[14] S. Caorsi, M. Donelli, and A. Massa, "Detection, location, and imaging of multiple scatterers by means of the iterative multiscaling method," *IEEE Trans. Microwave Theory Tech.*, vol. 52, no. 4, pp. 1217-1228, Apr. 2004.

[15] S. Caorsi, A. Massa, M. Pastorino, and M. Donelli, "Improved microwave imaging procedure for nondestructive evaluations of two-dimensional structures," *IEEE Trans. Antennas Propag.*, vol. 52, pp. 1386-1397, Jun. 2004.

[16] M. Benedetti, M. Donelli, and A. Massa, "Multicrack detection in two-dimensional structures by means of GA-based strategies," *IEEE Trans. Antennas Propagat.*, vol. 55, no. 1, pp. 205-215, Jan. 2007.

[17] V. Cingoski, N. Kowata, K. Kaneda, and H. Yamashita, "Inverse shape optimization using dynamically adjustable genetic algorithms," *IEEE Trans. Energy Conversion*, vol. 14, no. 3, pp. 661-666, Sept. 1999.

[18] L. Lizzi, F. Viani, R. Azaro, and A. Massa, "Optimization of a spline-shaped UWB antenna by PSO," *IEEE Antennas Wireless Propagat. Lett.*, vol. 6, pp. 182-185, 2007.

[19] J. Cea, S. Garreau, P. Guillame, and M. Masmoudi, "The shape and topological optimizations connection," *Comput. Methods Appl. Mech. Eng.*, vol. 188, no. 4, pp. 713-726, 2000.

[20] G. R. Feijoo, A. A. Oberai, and P. M. Pinsky, "An application of shape optimization in the solution of inverse acoustic scattering problems," *Inverse Problems*, vol. 20, pp. 199-228, Feb. 2004.

[21] M. Masmoudi, J. Pommier, and B. Samet, "The topological asymptotic expansion for the Maxwell equations and some applications," *Inverse Problems*, vol. 21, pp. 547-564, Apr. 2005.

[22] F. Santosa, "A level-set approach for inverse problems involving obstacles," *ESAIM: COCV*, vol. 1, pp. 17-33, Jan. 1996.

[23] A. Litman, D. Lesselier, and F. Santosa, "Reconstruction of a two-dimensional binary obstacle by controlled evolution of a level-set," *Inverse Problems*, vol. 14, pp. 685-706, Jun. 1998.

[24] O. Dorn, E. L. Miller, C. M. Rappaport, "A shape reconstruction method for electromagnetic tomography using adjoint fields and level sets," *Inverse Problems*, vol. 16, pp. 1119-1156, May 2000.

[25] C. Ramananjaona, M. Lambert, D. Lesselier, and J. P. Zolésio, "Shape reconstruction of buried obstacles by controlled evolution of a level-set: from a min-max formulation to a numerical experimentation," *Inverse Problems*, vol. 17, pp. 1087-1111, Dec. 2001.

[26] R. Ferrayé, J.-Y. Dauvignac, and C. Pichot, "An inverse scattering method based on contour deformations by means of a level set method using frequency hopping technique," *IEEE Trans. Antennas Propagat.*, vol. 51, no. 5, pp. 1100-1113, May 2003.

[27] E. T. Chung, T. F. Chan, X. C. Tai, "Electrical impedance tomography using level set representation and total variational regularization," *J. Comput. Phys.*, vol. 205, no. 2, pp. 707-723, May. 2005.

[28] K. van den Doel and U. M. Asher, "Dynamic level set regularization for large distributed parameter estimation problems," *Inverse Problems*, vol. 23, pp. 1271-1288, Jun. 2007.

[29] J. Strain, "Three methods for moving interfaces," *J. Comput. Phys.*, vol. 151, pp. 616-648, May 1999.

[30] O. Dorn and D. Lesselier, "Level set methods for inverse scattering," *Inverse Problems*, vol. 22, pp. R67-R131, Aug. 2006.

[31] J. H. Richmond, "Scattering by a dielectric cylinder of arbitrary cross-section shape," *IEEE Trans. Antennas Propagat.*, vol. 13, pp. 334-341, May 1965.

[32] S. Osher and J. A. Sethian, "Fronts propagating with curvature-dependent speed: algorithms based on Hamilton-Jacobi formulations," *J. Comput. Phys.*, 79, pp. 12-49, Nov. 1988.

[33] J. A. Sethian, *Level Set and Fast Marching Methods*. Cambridge University Press, Cambridge, UK, 2nd ed., 1999.

[34] K. Belkebir and M. Saillard, "Testing inversion algorithms against experimental data," *Inverse Problems*, vol. 17, pp. 1565-1702, Dec. 2001.

[35] M. Testorf and M. Fiddy, "Imaging from real scattered field data using a linear spectral estimation technique," *Inverse Problems*, vol. 17, pp. 1645-1658, Dec. 2001.

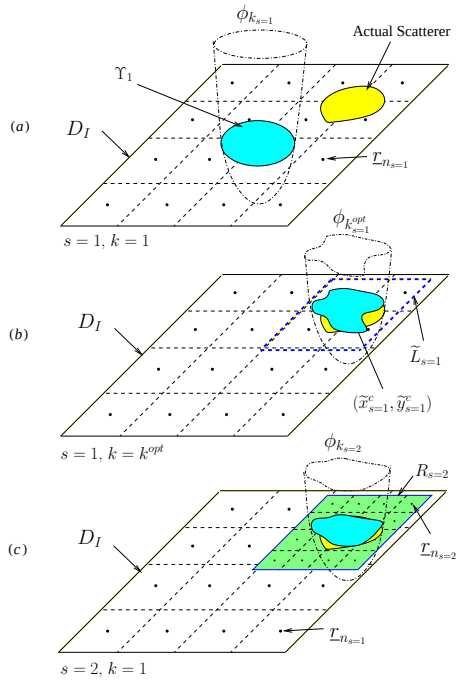

Figure 1. Graphical representation of the *IMSA-LS* zooming procedure. (a) First step ($k = 1$): the investigation domain is discretized in N sub-domains and a coarse solution is looked for. (b) First step ($k = k^{opt}$): the region of interest that contains the first estimate of the object is defined. (c) Second step ($k = 1$): an enhanced resolution level is used only inside the region of interest.

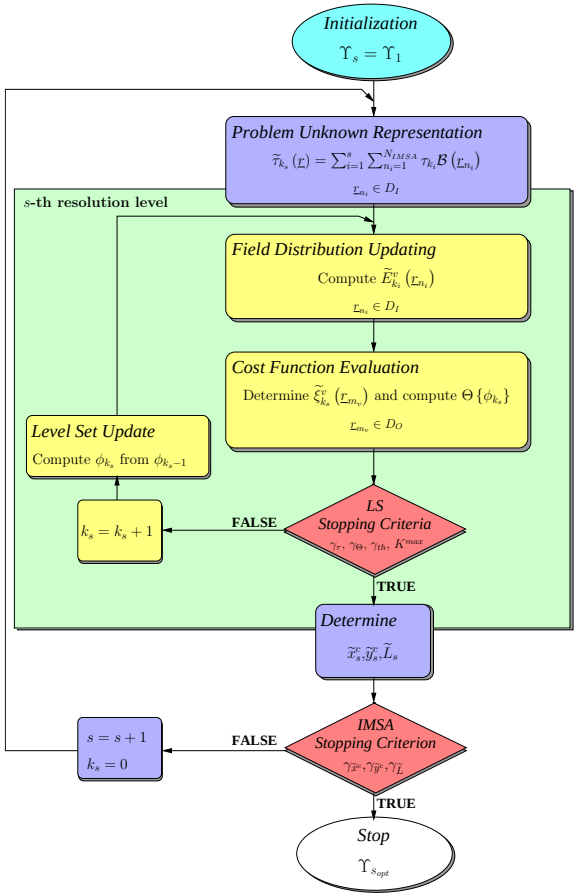

Figure 2. Block diagram description of the *IMSA-LS* zooming procedure.

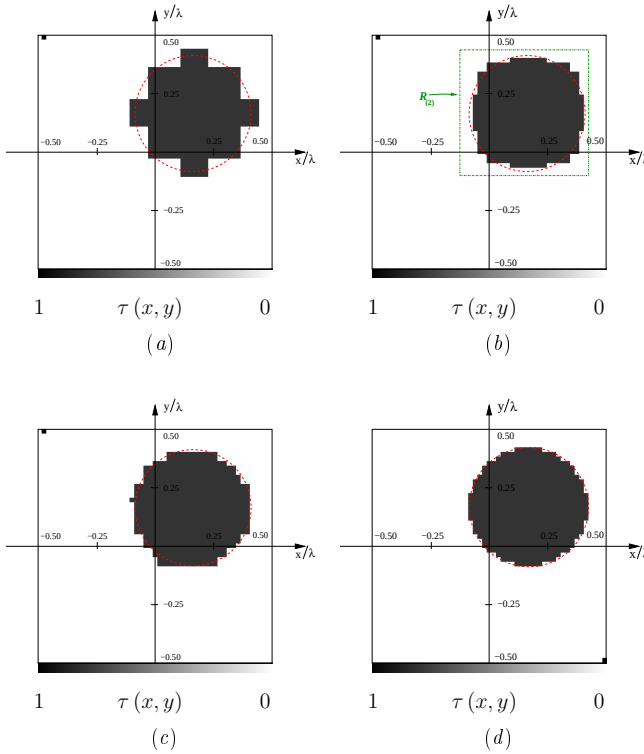

Figure 3. Numerical Data. Circular cylinder ($\epsilon_C = 1.8$, $L_D = \lambda$, *Noiseless Case*). Reconstructions with *IMSA-LS* at (a) $s = 1$ and (b) $s = s_{opt} = 2$, (c) *Bare-LS*. Optimal inversion (d).

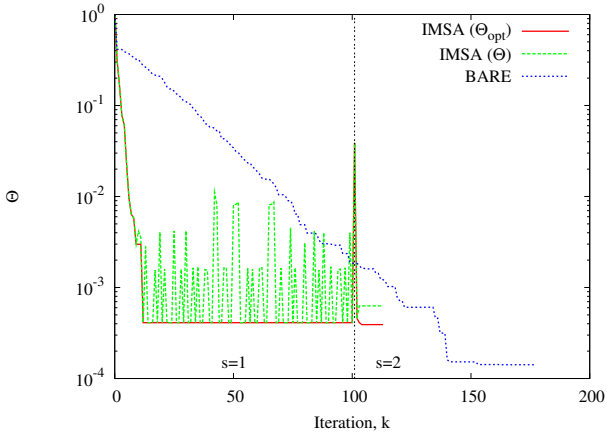

Figure 4. Numerical Data. Circular cylinder ($\epsilon_C = 1.8$, $L_D = \lambda$, *Noiseless Case*). Behavior of the cost function.

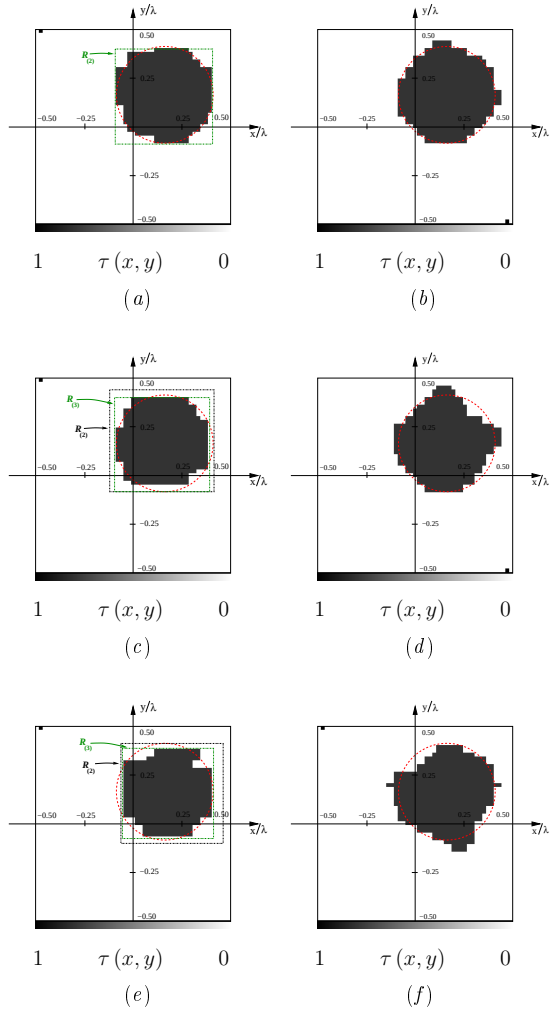

Figure 5. Circular cylinder ($\epsilon_C = 1.8$, $L_D = \lambda$, *Noisy Case*). Reconstructions with *IMSA-LS* (left column) and *Bare-LS* (right column) for different values of SNR [$SNR = 20\,dB$ (top), $SNR = 10\,dB$ (middle), $SNR = 5\,dB$ (bottom)].

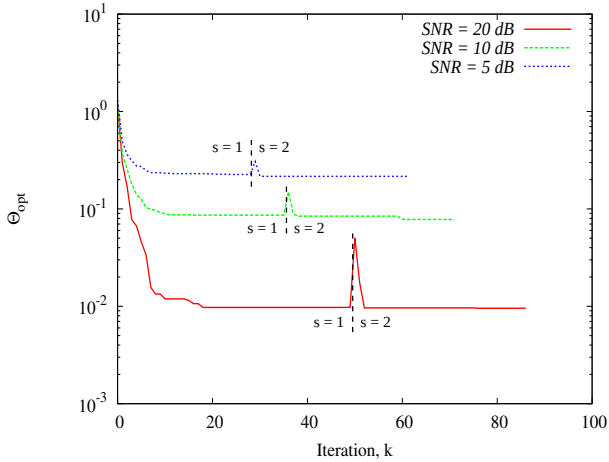

Figure 6. Numerical Data. Circular cylinder ($\epsilon_C = 1.8$, $L_D = \lambda$). Behavior of the cost function versus the noise level.

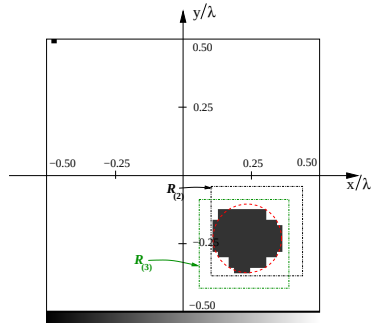

1 $\tau\,(x,y)$ 0

(a)

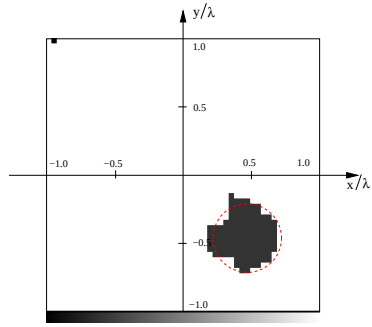

1 $\tau\,(x,y)$ 0

(b)

Figure 7. Numerical Data. Circular cylinder ($\epsilon_C = 1.8$, $L_D = 2\lambda$, $SNR = 5\,dB$). Reconstructions with (a) *IMSA-LS* and (b) *Bare-LS*.

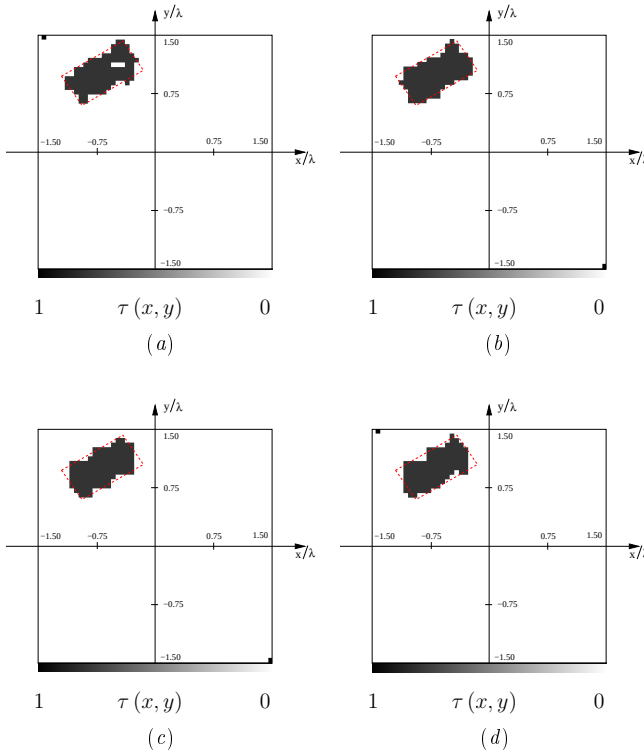

Figure 8. Numerical Data. Rectangular cylinder ($\epsilon_C = 1.8$, $L_D = 3\lambda$, *Noiseless Case*). Reconstructions with *IMSA-LS* for the different settings of Tab. 3 [(a) Γ_1, (b) Γ_2, (c) Γ_3, (d) Γ_4].

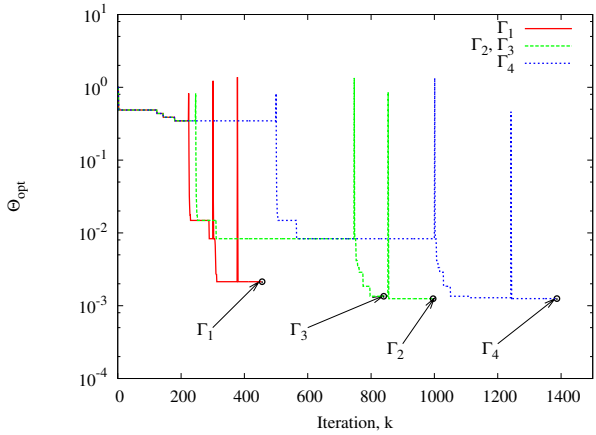

Figure 9. Numerical Data. Rectangular cylinder ($\epsilon_C = 1.8$, $L_D = 3\lambda$, *Noiseless Case*). Behavior of the cost function of *IMSA-LS* for the different settings of Tab. 3.

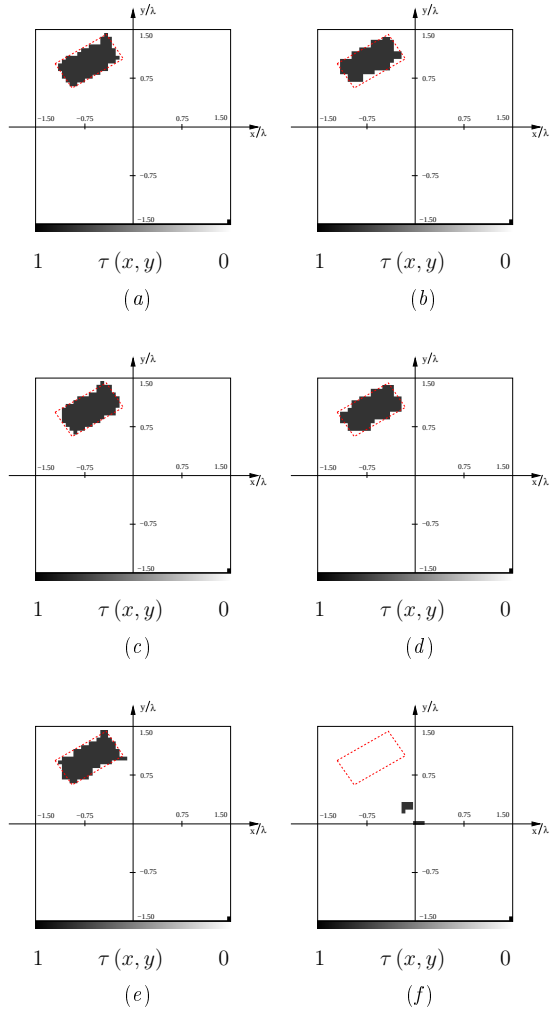

Figure 10. Numerical Data. Rectangular cylinder ($\epsilon_C = 1.8$, $L_D = 3\lambda$, *Noisy Case*). Reconstructions with *IMSA-LS* (left column) and *Bare-LS* (right column) for different values of SNR [$SNR = 20\,dB$ (top), $SNR = 10\,dB$ (middle), $SNR = 5\,dB$ (bottom)].

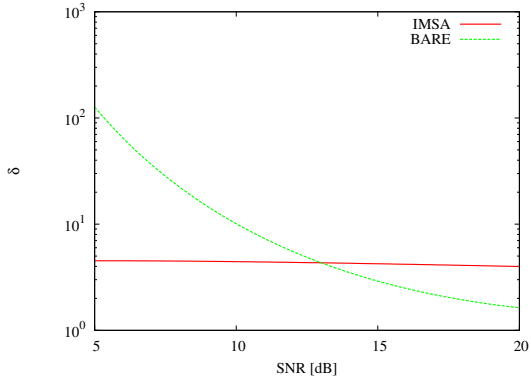

(*a*)

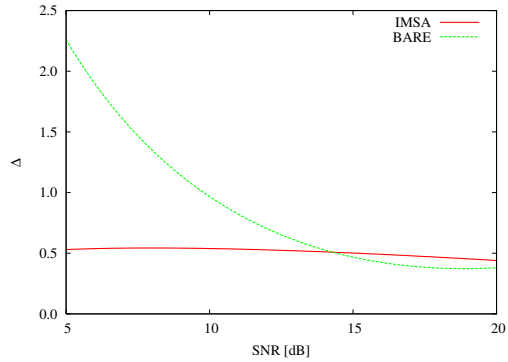

(*b*)

Figure 11. Numerical Data. Rectangular cylinder ($\epsilon_C = 1.8$, $L_D = 3\lambda$, *Noisy Case*). Values of the error figures versus SNR.

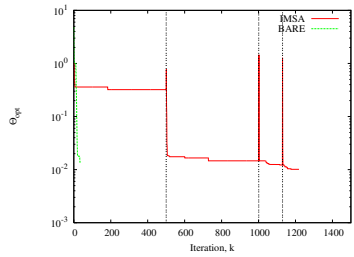

(a)

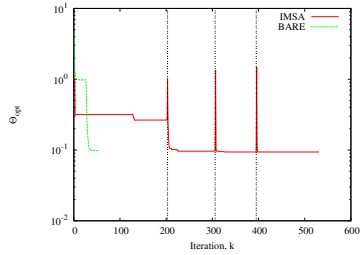

(b)

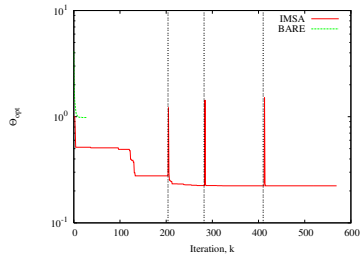

(c)

Figure 12. Numerical Data. Rectangular cylinder ($\epsilon_C = 1.8$, $L_D = 3\lambda$, *Noisy Case*). Behavior of the cost function versus the iteration index when (a) $SNR = 20\,dB$, (b) $SNR = 10\,dB$, and (c) $SNR = 5\,dB$.

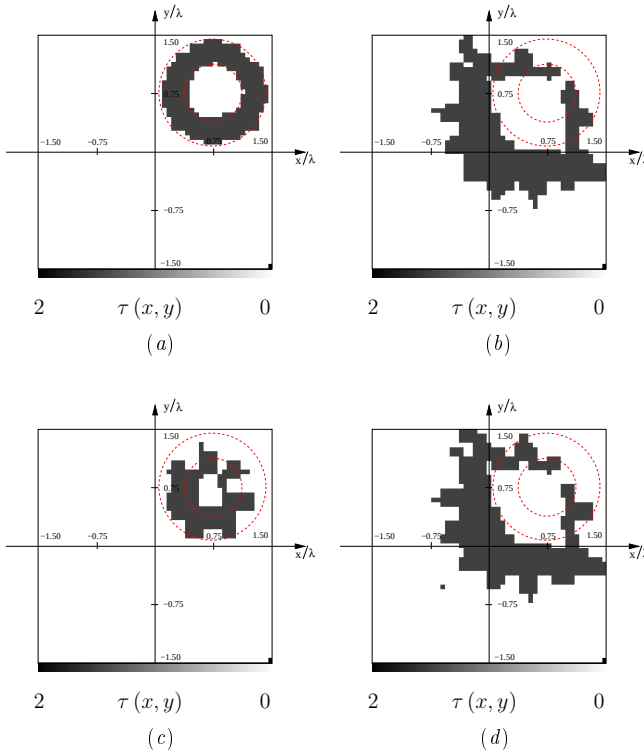

Figure 13. Numerical Data. Hollow cylinder ($\epsilon_C = 2.5$, $L_D = 3\lambda$, *Noisy Case*). Reconstructions with *IMSA-LS* (left column) and *Baræ-LS* (right column) for different values of SNR [$SNR = 20\,dB$ (top), $SNR = 10\,dB$ (bottom)].

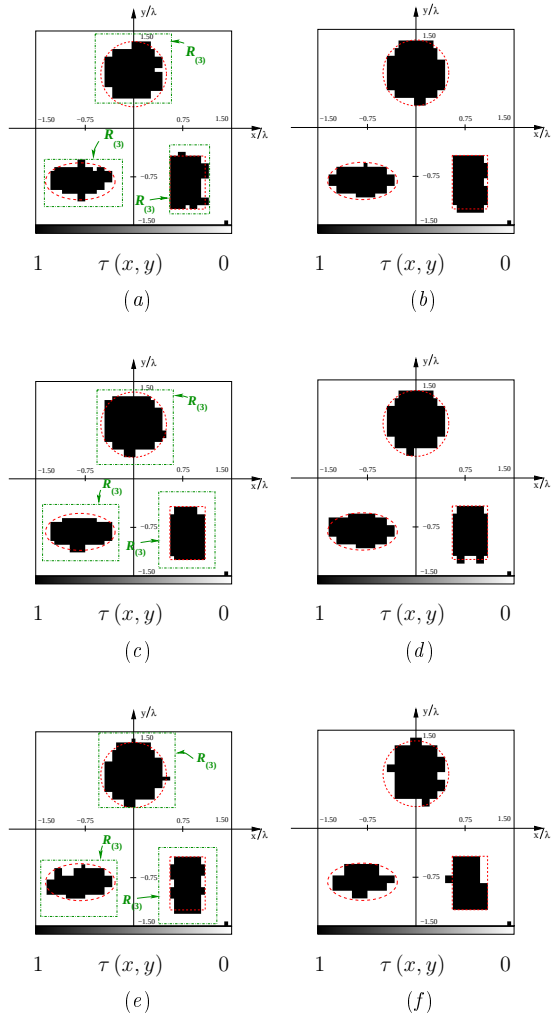

Figure 14. Numerical Data. Multiple scatterers ($\epsilon_C = 2.0$, $L_D = 3\lambda$, *Noisy Case*). Reconstructions with *IMSA-LS* (left column) and *Barræ-LS* (right column) for different values of SNR [$SNR = 20\,dB$ (top), $SNR = 10\,dB$ (middle), $SNR = 5\,dB$ (bottom)].

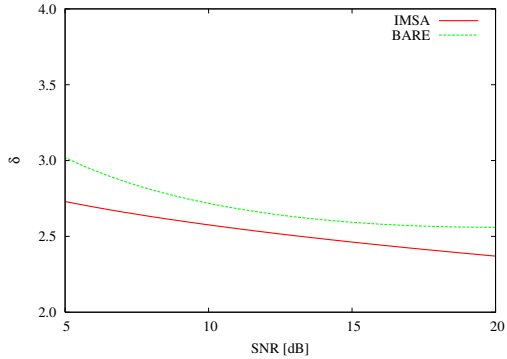

(*a*)

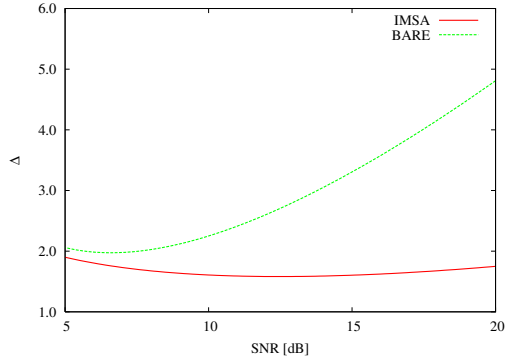

(*b*)

Figure 15. Multiple scatterers ($\epsilon_C = 2.0$, $L_D = 3\lambda$, *Noisy Case*). Values of the error figures versus SNR.

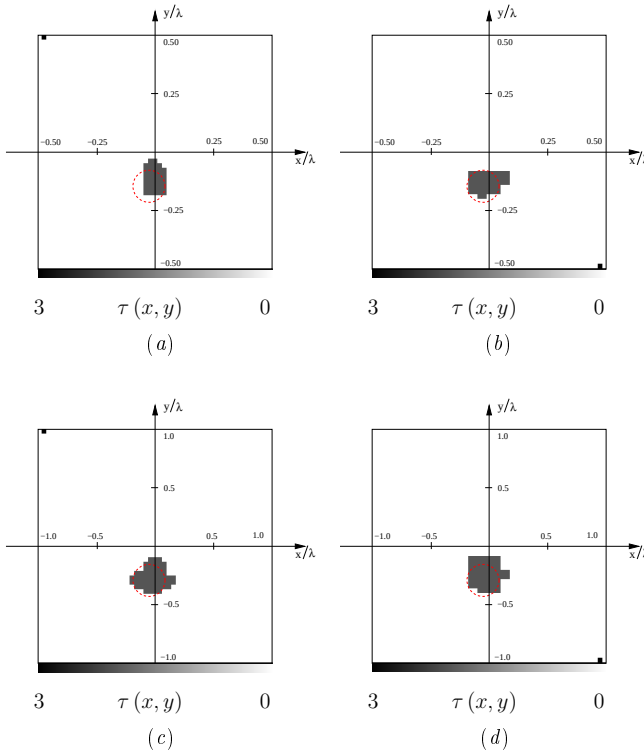

Figure 16(*I*). Experimental Data (Dataset "Marseille" [34]). Circular cylinder ("*dielTM_dec8f.exp*"). Reconstructions with *IMSA-LS* (left column) and *Bare-LS* (right column) at different frequencies f [$f = 1\,GHz$ $(a)(b)$; $f = 2\,GHz$ $(c)(d)$].

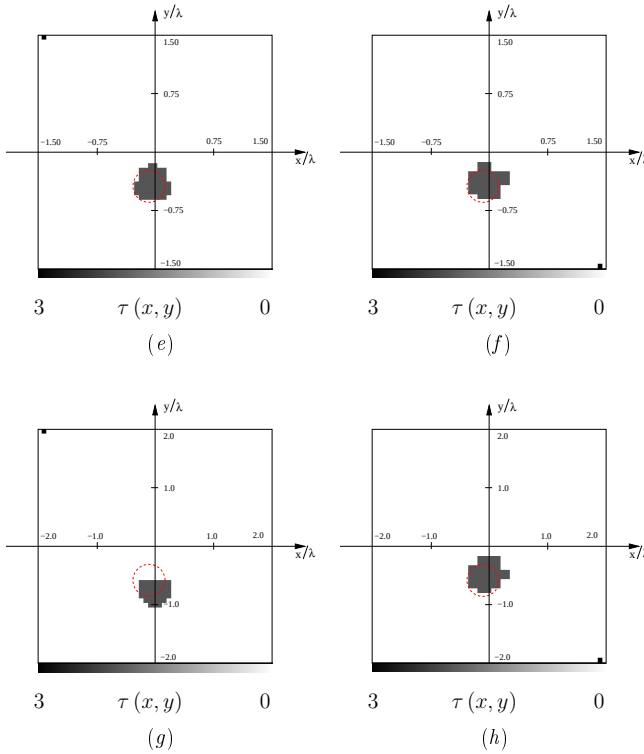

Figure 16(*II*). Experimental Data (Dataset "Marseille" [34]). Circular cylinder ("*dielTM_ dec8f.exp*"). Reconstructions with *IMSA-LS* (left column) and *Bare-LS* (right column) at different frequencies f [$f = 3\,GHz$ $(e)(f)$; $f = 4\,GHz$ $(g)(h)$].

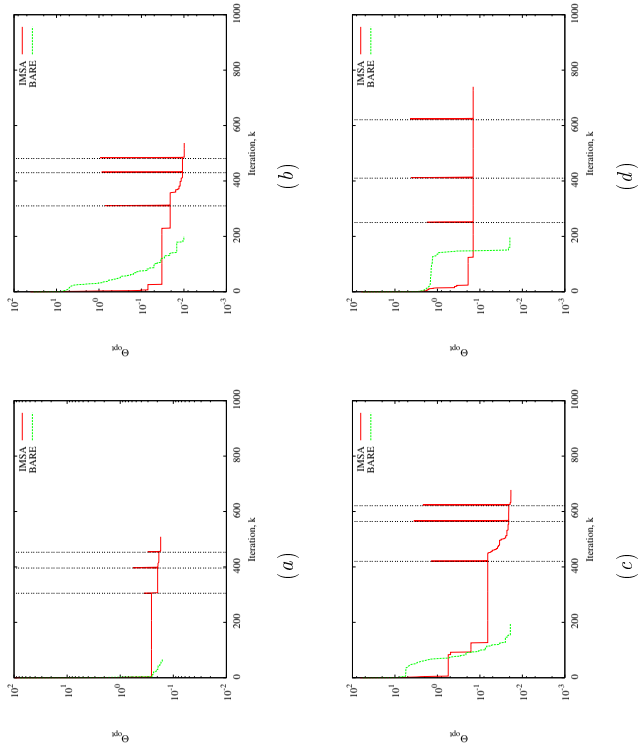

Figure 17. Experimental Data (Dataset "Marseille" [34]). Circular cylinder ("*dielTM_dec8f.exp*"). Behavior of the cost function versus the number of iterations when (a) $f = 1\,GHz$, (b) $f = 2\,GHz$, (c) $f = 3\,GHZ$, and (d) $f = 4\,GHz$.

	$IMSA-LS$		$Bare-LS$
	$s=1$	$s=2$	
δ	6.58×10^{-6}	2.19×10^{-6}	5.21×10^{-1}
Δ	2.36	0.48	0.64

Table 1. Numerical Data. Circular cylinder ($\epsilon_C = 1.8$, *Noiseless Case*). Error figures.

	$SNR = 20\,dB$		$SNR = 10\,dB$		$SNR = 5\,dB$	
	$IMSA - LS$	$Bare - LS$	$IMSA - LS$	$Bare - LS$	$IMSA - LS$	$Bare - LS$
δ	5.91×10^{-1}	2.72	2.28	2.45	6.78×10^{-1}	1.63
Δ	0.98	1.28	1.07	1.80	1.50	2.07

Table 2. Numerical Data. Circular cylinder ($\epsilon_C = 1.8$, *Noisy Case*). Values of the error indexes for different values of SNR.

Set of Parameters	γ_Θ	γ_τ	$\gamma_{\widetilde{x}^c}$, $\gamma_{\widetilde{y}^c}$	$\gamma_{\widetilde{L}}$
Γ_1	0.5	0.05	0.01	0.05
Γ_2	0.2	0.02	0.01	0.05
Γ_3	0.2	0.02	0.1	0.5
Γ_4	0.02	0.002	0.01	0.05

Table 3. Numerical Data. Rectangular cylinder ($\epsilon_C = 1.8$, $L_D = 3\lambda$, *Noiseless Case*). Different settings for the parameters of the stopping criteria.

	$SNR = 20\,dB$		$SNR = 10\,dB$		$SNR = 5dB$	
	$IMSA-LS$	$Bare-LS$	$IMSA-LS$	$Bare-LS$	$IMSA-LS$	$Bare-LS$
k_{tot}	1089	41	393	53	410	28
N	361	1089	361	1089	361	1089
f_{pos}	1.02×10^{11}	1.02×10^{11}	3.70×10^{10}	1.37×10^{11}	3.86×10^{10}	7.23×10^{10}

Table 4. Numerical Data. Rectangular cylinder ($\epsilon_C = 1.8$, $L_D = 3\lambda$, *Noisy Case*). Computational indexes for different values of SNR.

	$f = 1\,GHz$		$f = 2\,GHz$	
	$IMSA - LS$	$Bare - LS$	$IMSA - LS$	$Bare - LS$
k_{tot}	506	69	532	200
f_{pos}	4.88×10^9	1.22×10^{11}	5.14×10^9	3.55×10^{11}

	$f = 3\,GHz$		$f = 4\,GHz$	
	$IMSA - LS$	$Bare - LS$	$IMSA - LS$	$Bare - LS$
k_{tot}	678	198	621	200
f_{pos}	6.55×10^9	3.51×10^{11}	5.99×10^9	3.55×10^{11}

Table 5. Experimental Data (Dataset "Marseille" [34]). Circular cylinder ("*dielTM_dec8f.exp*"). Computational indexes.

Contents

List of Tables

List of Figures

Structure of the Thesis

The thesis is structured in chapters according to the organization detailed in the following.

The first chapter deals with an introduction to the thesis, focusing on the main motivations and on the subject of this work.

Then, Chapter 2 presents the mathematical formulation of the inverse scattering problem, pointing out the main drawbacks such as non-linearity, ill-condition, and ill-posedness.

Chapter 3 is concerned with the state-of-the-art. The exploitation of regularized solutions and approximations to cope with the ill-posedness of the inverse problem is discussed. Moreover, both deterministic and heuristic minimization techniques are presented. Finally, a brief coverage of the literature on multi-resolution techniques and shape-optimization is given.

The iterative multi-scaling approach with level-set-based

optimization is discussed in Chapter 4. The mathematical formulation is focused on the multi-step architecture and the proposed numerical validation, carried out when considering both numerically-synthesized and laboratory-controlled data, assesses the reconstruction capabilities of the proposed methodology by considering targets characterized by simple and complex shape.

Chapter 5 deals with the iterative multi-scaling multi-region approach with level-set-based minimization, customized for geometries characterized by multiple objects. After presenting the mathematical formulation by focusing on the main differences with respect to the single-region version, the effectiveness of the approach is evaluated by means of the discussion of a selected set of results, when dealing with both numerical and laboratory-controlled data.

Conclusions, further developments, and open problems are presented in Chapter 6. Finally, two appendices gives more detail on the adjoint problem (whose solution allows to compute the gradient of the cost function) and on two imaging algorithms (the edge detection operator and a technique for counting the number of obstacles in an image).

Chapter 1

Introduction

In the introduction, the motivation of the thesis is pointed out starting from a brief overview about the framework of techniques for non-destructive evaluation and testing.

The non-invasive reconstruction of position and shape of unknown targets is a topic of great interest in many applications, such as non-destructive evaluation and testing (usually referred to with the acronyms "NDE" and "NDT") for industrial monitoring and subsurface sensing [1]. In such an interesting framework, many methodologies have been proposed, mainly based on x-rays [2], ultrasonics [3], and eddy currents [4]. However, microwave approaches have been recently recognized as effective imaging methodologies because of the following key points [1] [5]-[8]:

(a) electromagnetic fields at microwave frequencies can penetrate non-ideal conductor materials;

(b) the field scattered by the target is representative not only of its boundary, but also of its inner structure;

(c) microwaves show a high sensivity to the water content of the structure under test;

(d) microwave sensors can be employed without mechanical contacts with the specimen.

In addition, compared to x-ray and magnetic resonance, microwave-based approaches minimize (or avoid) collateral effects in the specimen under test. Therefore, they can be safely employed in biomedical imaging, limiting the stress for the patient since the physical contact with the imaging system can be avoided (e.g., the breast screening [9]), or in other critical applications, such as through-wall imaging (TWI) [10].

A further advance in microwave non-invasive inspection is represented by inverse scattering approaches aimed at reconstructing the image of the region under test in a *quantitative* fashion [11]. Unfortunately, the underlying mathematical model is characterized by several drawbacks that currently limit their massive employment, especially in the NDE/NDT's framework. More in detail, the inverse scattering problems are intrinsically ill-posed [12] as well as non-linear [13].

Since the ill-posedness is strongly related to the amount of collectable information and usually the number of independent data is lower than the dimension of the solution space, multi-view/multi-illumination systems are generally adopted. However, it is well known that the collectable information is an upper-bounded quantity [14][15]. Consequently, it is necessary to effectively exploit the overall information contained in the scattered field samples for achieving a satisfactory reconstruction.

In order to exploit the whole amount of information collected from scattering measurements, multi-resolution strategies have been recently proposed. The idea is that of using an enhanced spatial resolution only in those regions of interest (RoIs) where the unknown scatterers are found to be located [16] and/or where discontinuities occur [17][18]. As for the proposed implementations, deterministic or statistically-based data processing strategies have been proposed to determine the optimal resolution level, and spline-based approaches have been employed to improve the resolution level. Furthermore, multi-step approaches have been implemented to iteratively increase the spatial resolution by means of a so-called "zooming"

procedure [19] by keeping the ratio between unknowns and data suitably low and constant, thus reducing the risk of occurrence of local minima [15] in the arising optimization problem.

On the other hand, the lack of information affecting the inverse problem has been addressed, especially in NDE/NDT, through the exploitation of the *a-priori* knowledge on the scenario under test by means of an effective representation of the unknowns. In many applications, the unknown defect is characterized by known electromagnetic properties (i.e., dielectric permittivity and conductivity) and it lies within a known host region. Moreover, depending on the desired degree of accuracy, more complex scenarios can be approximated by a set of homogeneous regions characterized by different "shape" and electromagnetic parameters [20]. Under these assumptions, an imaging problem reduces to a shape reconstruction problem, namely to a problem where the support of the homogeneous regions needs to be retrieved. Towards this end, parametric techniques aimed at representing the unknown object in terms of descriptive parameters of reference shapes [21]-[22] and more sophisticated approaches such as evolutionary-controlled spline curves [23]-[25], shape gradients [26]-[28] or level-sets [31]-[32] have been proposed. As far as level-set-based methods are concerned, the homogeneous object is defined as the zero level of a continuous function and, unlike pixel-based or parametric-based strategies, such a description enables one to represent complex shapes or regions in a simple way.

Within such a framework, the thesis focuses on the development and the analysis of the integration of the iterative multi-scaling strategy (*IMSA*) [19] and the level-set (*LS*) representa-

tion [33]. The implementation is aimed at profitably exploiting both the available *a-priori* knowledge on the scenario under test (e.g., the homogeneity of the scatterer) and the information content from the scattering measurements. For the sake of simplicity and with no claim of exhaustivity, the inverse problem formulation is restricted to the two-dimensional transverse-magnetic (TM) case when dealing with one and with multiple RoIs. As for the assessment of the proposed strategy, the numerical validation deals with dielectric lossless scatterers, by considering both synthetic and experimental (i.e., laboratory-controlled) data.

Chapter 2

The Inverse Scattering Problem

The electromagnetic inverse scattering problem is presented in this chapter, focusing on its mathematical formulation as well as on the main drawbacks, such as non-linearity, ill-conditioning, and ill-posedness.

2.1 Mathematical Formulation

2.1.1 Field Scattered by Inhomogeneous Objects

Let us consider a region, called investigation domain D_I, characterized by a relative permittivity $\epsilon(\underline{r})$ and conductivity $\sigma(\underline{r})$. As shown in Fig. 2.1, such a region is probed by a set of V transverse-magnetic (TM) plane waves sources, with electric field $\underline{\zeta}^v(\underline{r}) = \zeta^v(\underline{r})\hat{\underline{z}}$ ($v = 1, \ldots, V$), $\underline{r} = (x, y)$, and the scattered field, $\underline{\xi}^v(\underline{r}) = \xi^v(\underline{r})\hat{\underline{z}}$, is collected at $M(v)$, $v = 1, ..., V$, measurement points $\underline{r}_{m(v)}$ distributed in the observation domain D_O.

In order to electromagnetically describe the investigation domain D_I, let us define the contrast function

$$\tau(\underline{r}) = [\epsilon(\underline{r}) - 1] - j\frac{\sigma(\underline{r})}{2\pi f \varepsilon_0} \qquad \underline{r} \in D_I\,, \tag{2.1}$$

where f is the frequency of operation (the time dependence $e^{j2\pi ft}$ being implied). Under the hypothesis of a linear, isotropic and non-magnetic propagation medium, the scattered field distribution $\xi^v(\underline{r})$ is the solution of the following Helmholtz equation (see [13][35][36] for a more detailed explanation)

$$\nabla^2 \xi^v(\underline{r}) - \left(\frac{2\pi}{\lambda}\right)^2 \xi^v(\underline{r}) = -j2\pi f \mu_0 J^v(\underline{r})\,. \tag{2.2}$$

where λ is the background wavelength. Moreover, $J^v(\underline{r})$ is the

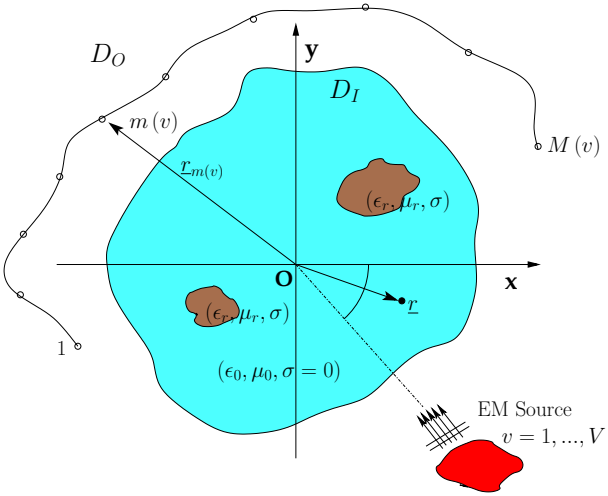

Figure 2.1: Geometry of an inverse scattering problem.

equivalent current density radiating in free-space, defined in D_I as follows

$$J^v(\underline{r}) = j2\pi f \varepsilon_0 \tau\,(\underline{r})\, E^v\,(\underline{r}) \tag{2.3}$$

E^v being the total electric field. By imposing that $\xi^v(\underline{r})$ satisfies the Sommerfeld radiation condition, namely

$$\lim_{|\underline{r}|\to+\infty} \sqrt{|\underline{r}|}\left(\frac{\partial \xi^v(\underline{r})}{\partial\,|\underline{r}|} - j\kappa(\underline{r})\xi^v(\underline{r})\right) = 0\,, \tag{2.4}$$

the solution of (2.2) is given by the following pair of Lippmann-

Schwinger integral equations

$$\xi^v\left(\underline{r}_{m(v)}\right) = \left(\tfrac{2\pi}{\lambda}\right)^2 \int_{D_I} \tau\left(\underline{r}'\right) E^v\left(\underline{r}'\right) G_{2D}\left(\underline{r}_{m(v)}/\underline{r}'\right) d\underline{r}' \qquad \underline{r}_{m(v)} \in D_O\,, \tag{2.5}$$

$$\zeta^v\left(\underline{r}\right) = E^v\left(\underline{r}\right) - \left(\tfrac{2\pi}{\lambda}\right)^2 \int_{D_I} \tau\left(\underline{r}'\right) E^v\left(\underline{r}'\right) G_{2D}\left(\underline{r}/\underline{r}'\right) d\underline{r}' \qquad \underline{r} \in D_I\,. \tag{2.6}$$

Moreover, $G_{2D}\left(\underline{r}/\underline{r}'\right)$ is the free-space two-dimensional Green's function defined as follows

$$G_{2D}\left(\underline{r}/\underline{r}'\right) = -\frac{j}{4} H_0^{(2)}\left(\frac{2\pi}{\lambda}\left\|\underline{r} - \underline{r}'\right\|\right)\,, \tag{2.7}$$

$H_0^{(2)}$ being the second-kind zeroth-order Hankel function.

The aim of an inverse scattering technique is the reconstruction of both the electromagnetic properties $\tau(\underline{r})$ and the total field distribution $E^v\left(\underline{r}\right)$, with $\underline{r}$ belonging to D_I [i.e., the equivalent current density $J^v(\underline{r})$], starting from the knowledge of the measurements $\xi^v\left(\underline{r}_{m(v)}\right)$, $r_{m(v)} \in D_O$, and of the incident field $\zeta^v\left(\underline{r}\right)$ radiated by the known source. Unfortunately, a closed form solution of integral equations (2.5) and (2.6) does not generally exist. Consequently, the inverse scattering problem has to be reformulated and effective inversion methodologies have to be employed in order to retrieve the solution. Chapter 3 will focus on the state-of-the-art of the inverse scattering approaches.

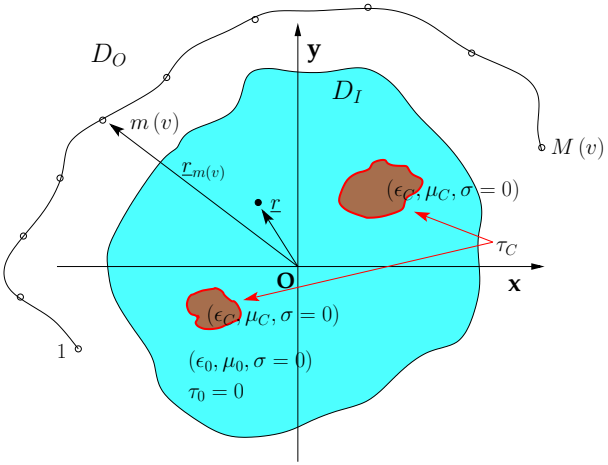

Figure 2.2: Geometry of an inverse scattering problem when *a-priori* information about the scatterer is available.

2.1.2 Exploitation of the *a-priori* Information about the Scatterers

Let us now assume that a cylindrical homogeneous non-magnetic object with known relative permittivity ϵ_C and conductivity σ_C occupies a non-homogeneous region Υ belonging to an investigation domain D_I. How could such an amount of *a-priori* information be profitably exploited? A possible solution consists in re-defining the contrast function $\tau(\underline{r})$ as follows

$$\tau(\underline{r}) = \begin{cases} \tau_C & \underline{r} \in \Upsilon \\ 0 & \text{otherwise} \end{cases} \tag{2.8}$$

letting

$$\tau_C = (\epsilon_C - 1) - j\frac{\sigma_C}{2\pi f \varepsilon_0}\,. \tag{2.9}$$

Since the dielectric properties of the obstacles are *a-priori* known and homogeneous, the shape of Υ, or its contour, becomes a sufficient parameter for the characterization of the domain under test. Consequently, suitable inversion techniques can be applied in order to retrieve the boundaries of Υ by solving equations (2.5) and (2.6). Such techniques, usually known as shape-optimization methods [37], are dealt with in Sect. 3.4.

Although the hypothesis of homogeneous objects and a-priori known permittivity and conductivity appears to be strong and restrictive, many inverse problems can be reduced to the search of homogeneous obstacles inside homogeneous or *a-priori* known backgrounds [32][33].

2.2 Numerical Solution of the Inverse Scattering Problem

In order to allow a numerical solution of the inverse scattering problem, equations (2.5) and (2.6) can be discretized according to a point-matching version of the Method of Moments (MoM) [39]. More in detail, the investigation domain D_I is partitioned in N square sub-domains D_n with barycentres $\underline{r}_n$, $n = 1, ..., N$. In each sub-domain, a pulse basis function is defined as

$$\mathcal{B}\left(\underline{r}_n\right) = \begin{cases} 1 & \text{if } \underline{r}_n \in D_n \\ 0 & \text{if } \underline{r}_n \notin D_n \end{cases}\,, \tag{2.10}$$

while the discrete contrast function is given by the following relationship

$$\tau\left(\underline{r}\right) = \sum_{n=1}^{N} \tau_n \mathcal{B}\left(\underline{r}_n\right) \qquad \underline{r},\, \underline{r}_n \in D_I\,. \tag{2.11}$$

Consequently, by assuming that the incident field ζ^v and the total field E^v are constant inside each sub-domain D_n, the discrete form of the Lippmann-Schwinger integral equations is given by the following relationships

$$\xi^v_{m(v)}\left(\underline{r}_{m(v)}\right) = \sum_{n=1}^{N} \tau_n E^v_n\left(\underline{r}_n\right) G_{2D}\left(\underline{r}_{m(v)}/\underline{r}_n\right) \qquad \underline{r}_{m(v)} \in D_O\,, \tag{2.12}$$

$$\zeta^v_n\left(\underline{r}_n\right) = E^v_n\left(\underline{r}_n\right) - \sum_{p=1}^{N} \tau_p E^v_p\left(\underline{r}_p\right) G_{2D}\left(\underline{r}_n/\underline{r}_p\right) \qquad \underline{r}_n \in D_I\,, \tag{2.13}$$

where $G_{2D}\left(\underline{r}_m/\underline{r}_n\right)$ is the two-dimensional discrete Green operator given by

$$G_{2D}\left(\underline{r}_m/\underline{r}_n\right) = \begin{cases} -\frac{j}{2}\left[\pi\kappa_o A H_1^{(2)}\left(\kappa_o A\right) - 2j\right] & \text{if } m = n \\ -\frac{j\pi\kappa_o A}{2} J_1\left(\kappa_o A\right) H_0^{(2)}\left(\kappa_o \left\|\underline{r}_m - \underline{r}_n\right\|\right) & \text{if } m \neq n \end{cases} \tag{2.14}$$

where A is the area of the square sub-domain, $\kappa_o = \frac{2\pi}{\lambda}$ is the free-space wavenumber, $H_1^{(2)}$ is the second kind first order Hankel function, and J_1 is the first kind Bessel function.

2.3 Drawbacks of the Inverse Scattering Problem

Unlike the forward scattering problem, which is aimed at determining the fields ξ^v and E^v (i.e., the "effects") starting from ζ^v and the τ (i.e., the "cause"), the inverse scattering problem should reconstruct the cause starting from the observation of the measurable effects. It is also well known (see [13] and [38] for an exhaustive and detailed overview) that the inverse problems are intrinsically characterized by several drawbacks, which are detailed in the following:

- ***Ill-posedness*** - The forward problem is characterized by a loss of information, since its solution represents a transformation from a physical quantity (i.e., the complete description of the scatterer τ and the knowledge of the electromagnetic source ζ^v) with a certain information content to the scattered field, which is characterized by a lower information content. In addition, the scattered field provided by a band-limited system is smoother than the one provided by the actual object. As a consequence, the corresponding inverse scattering problem requires a gain of information in order to retrieve a solution as close as possible to the "cause". Such a loss of information is known as "ill-posedness" of the inverse problem. To cope with the ill-posedness, the "golden rule" consists in adding some *additional* information to compensate the loss of information of the imaging process. Such a information is defined as *additional* since it cannot be derived neither

from the scattered field nor from the properties of the mapping between the data and the space of unknowns, which describes the imaging process. It comes from other informative sources or from previous information gained on the object [40] and it is usually referred to as *a-priori* information.

- ***Non-linearity*** - With reference to equations (2.12) and (2.13), the inverse problem is non-linear because the variable τ to be solved can not be written as a linear sum of independent components. As a matter of fact, the total field E^v depends on the dielectric properties of the domain under test. On the other hand, the inverse scattering problem is linear with respect to the equivalent current density $J^v(\underline{r}) = \tau(\underline{r})E^v(\underline{r})$, according to a contrast source formulation [41][42].

- ***Ill-conditioning*** - As a consequence of the ill-posedness and due to the band-limited nature of the system as well, the numerical counterpart of the inverse scattering problem appears to be ill-conditioned, since the solution does not depend continuously on the data. As a matter of fact, the numerical solution may suffer from numerical instability and a small error in the initial data can result in much larger errors in the answers.

These drawbacks have to be taken into account when solving an inverse scattering problem. In Ch. 3, a brief overview on the state-of-the-art of the inversion methodologies will be pre-

sented, focusing on the multi-resolution approaches and the shape-optimization methods.

Chapter 3

An Overview on Inverse Scattering Techniques

This chapter deals with an overview on the inverse scattering techniques. The exploitation of regularized solutions and approximations to cope with the ill-posedness of the inverse problem will be discussed. Then, both deterministic and heuristic minimization techniques will be presented. Finally, the chapter focuses on the state-of-the-art on multi-resolution techniques and shape-optimization.

3.1 Regularized Solutions and Approximations

As pointed out in Sect. 2.3, the inverse problem is characterized by ill-posedness, which is a consequence of the loss of information between "cause" and "effect" in the forward problem. A possible solution consists in mathematically expressing some expected physical properties of the scatterer and to explicitly use such a knowledge to build families of approximate solutions. For instance, *A. N. Tikhonov* and *V. Y. Arsenin* [38] introduced a family of approximate solutions depending on a *regularization parameter*. For noise-free data, the approximate solutions converge to the true solution when the regularization parameter tends to zero. Otherwise, an optimal approximation of the exact solution exists for a non-zero value of the regularization parameter. However, the choice of the value of the *regularization parameter* becomes the main issue, since it could depend on the geometry under test. Furthermore, while mathematical methods and efficient numerical algorithms are already available for linear inverse scattering problems, the scientific literature does not provide any simple rule for the optimal choice of the regularization coefficient when nonlinear problems are dealt with [43]. Looking for criteria, in [44] and [45] the authors considered this parameter an additional unknown which has to be controlled by the optimization process.

On the other hand, the improvement of the robustness with respect to false solutions and the convergence rate as well as the non-uniqueness and ill-conditioning inherent to inverse scatter-

ing problems has been dealt with as well [46]-[50]. As far as non-linearity is concerned, some attempts have been devoted to the problem linearization by using suitable approximations. However, the use of Born, Rayleigh and Rytov approximations [13] is suitable only for dealing with weakly scattering objects [51]. The iterative Born method [52] and its modified form [53] could extend their availability, but they still remain techniques that can be applied only to dielectric scatterers.

3.2 An Overview on Minimization Techniques

In order to cope with the non-linearity, the inverse scattering problem can be recast as an optimization procedure, where a suitable cost function depending on the mismatch between the measured fields and the numerically evaluated one is minimized. Such a cost function is computed on the basis of the trial solution $\underline{\widetilde{\tau}} = \{\widetilde{\tau}_n;\ n = 1, ..., N\}$ and it is usually expressed in matrix form as follows [13]

$$\Phi\left\{\underline{\widetilde{\tau}}\right\} = \alpha \frac{\left\|\underline{\varsigma} - \underline{\underline{G}}_{EXT}\underline{\widetilde{\tau}}\,\underline{\widetilde{E}}\right\|^2}{\left\|\underline{\varsigma}\right\|^2} + \beta \frac{\left\|\underline{\zeta} - \underline{\widetilde{E}} + \underline{\underline{G}}_{INT}\underline{\widetilde{\tau}}\,\underline{\widetilde{E}}\right\|^2}{\left\|\underline{\zeta}\right\|^2} \tag{3.1}$$

where $\underline{\underline{G}}_{EXT}$ and $\underline{\underline{G}}_{INT}$ are the $M \times N$ external Green's matrix and the $N \times N$ internal Green's matrix, respectively, and α, β

are two user-defined regularization parameters. Furthermore, $\underline{\zeta}$ is the $N \times 1$ incident field array, $\underline{\xi}$ is the $M \times 1$ measured field, and $\underline{\widetilde{E}}$ is the $N \times 1$ estimated total electric field.

The optimal solution $\underline{\tau}_{opt}$ is found as the $N \times 1$ array that minimizes the relationship (3.1), namely

$$\underline{\tau}_{opt} = \arg\left\{\min_{k=1,\ldots,K}\left[\Phi\left\{\underline{\widetilde{\tau}}_k\right\}\right]\right\} \tag{3.2}$$

where $\underline{\widetilde{\tau}}_k$ is the trial solution achieved at the step k by the iterative updating procedure. As a consequence, the quality of the final solution depends mostly on the search strategy, since the problem may have false solutions due to its non-linearity. The next two subsections discuss both deterministic and heuristic approaches.

3.2.1 Deterministic Approaches

As far as deterministic approaches are concerned, the most widely used are the gradient-based techniques introduced by *Kleinman et al.* in [54]. Such methodologies are based on a simultaneous update of the unknown field $\underline{\widetilde{E}}_k$ and scatterers contrast $\underline{\widetilde{\tau}}_k$ in order to avoid the full solution of the forward problem at each iteration. Towards this end, a sequence of trial solutions $\underline{\widetilde{\chi}}_k = \left[\underline{\widetilde{\tau}}_k, \underline{\widetilde{E}}_k\right]$, $k = 1, ..., K$, is defined with strictly decreasing cost function values. At each iteration k, the trial solution is updated as follows

$$\underline{\widetilde{\chi}}_{k+1} = \underline{\widetilde{\chi}}_k + \nu_k \cdot \underline{\mathcal{U}}_k \tag{3.3}$$

where $\mathcal{U}_k$ is the value of the updating function at the iteration k, $k = 1, ..., K$, and

$$\nu_k = \arg\left\{\min_p\left[\Phi\left\{\widetilde{\underline{\chi}}_k + \nu_p \cdot \mathcal{U}_k\right\}\right]\right\} . \tag{3.4}$$

The iterative procedure is iterated until the value of (3.1) is smaller than a fixed threshold or a stationary condition is reached.

The updating of the unknowns $\underline{\mathcal{U}}_k$ consists in the evaluation of the steepest descent $\underline{\Gamma}_k = -\nabla_{\tau_k}\left(\Phi\left\{\widetilde{\underline{\chi}}_k\right\}\right)$. Several updating strategies have been developed, but one of the most effective architecture in terms of convergence rate is the *Polak-Ribiere* procedure [55]. Such an algorithm defines the following update term

$$\underline{\mathcal{U}}_k = \underline{\Gamma}_k - \frac{\underline{\Gamma}_k^T\left(\underline{\Gamma}_k - \underline{\Gamma}_{k-1}\right)}{\underline{\Gamma}_{k-1}^T\underline{\Gamma}_{k-1}}\mathcal{U}_{k-1} \tag{3.5}$$

where the superscript T indicates the transpose operator.

As for some examples of other updating strategies, the *bi-conjugate gradient method* (see [56] and [57] for more details), or its development called the *bi-conjugate gradient stabilized* method (see [58] for more details), have been implemented to solve nonsymmetric systems. Moreover, the *generalized minimum residual* (*GM-RES*) method (see [59] for more details) and the *quasi minimal residual method* (see [60] for more details) have a different approach based on the creation of proper basis functions to represent the solution space. However, such strategies are often more demanding, even though a faster convergence rate is reported. Moreover, at the best of the author's

knowledge, these updating approaches are generally used to solve linear problems.

3.2.2 Heuristic Minimization Methodologies

Unfortunately, the convergence of the deterministic minimization strategies is strictly dependent on the initialization point. As a matter of fact, since the problem at hand is non-linear, the solution can be easily trapped in local minima representing false reconstructions if the initialization is not appropriate.

Since false solutions are physically unacceptable solutions, the minimization methods should meet the following requirements to avoid local minima:

(a) the possibility of easily including the whole amount of available *a-priori* information on the unknown solution;

(b) on-line control of the solution quality in order to assure that trial solutions, estimated during the sampling of the search space, are physically admissible solutions;

(c) suitable operators able to fully exploit the information on the solution gained during the minimization and/or arising from the *a-priori* information;

(d) operators able to easily replace non-feasible solutions by newly feasible ones, without introducing user-defined penalty functions.

Such properties are usually owned by the heuristic optimization techniques based on evolutionary algorithms. These strategies are characterized by the definition of a set of W trial solution $\underline{\widetilde{\chi}}_k = \left\{ \underline{\widetilde{\chi}}_k^w ;\, w = 1, ..., W \right\}$, commonly called population, that is iteratively updated according to the following general relationship

$$\underline{\widetilde{\chi}}_{k+1} = \underline{\widetilde{\chi}}_k + \underline{\underline{\mathcal{U}}}_k \left\{ \underline{\widetilde{\chi}}_\ell ;\, \ell = 1, ..., k \right\} \tag{3.6}$$

where the updating operator $\underline{\underline{\mathcal{U}}}_k \{\cdot\}$ depends on the current solution and on the previous $k-1$ trial solution. Consequently, the optimal solution is found as the one minimizing the cost function (3.1), namely

$$\underline{\chi}_{opt} = \arg \left\{ \min_{k=1,...,K} \left[\min_{w=1,...,W} \left(\Phi \left\{ \underline{\widetilde{\chi}}_k^w \right\} \right) \right] \right\} . \tag{3.7}$$

where $\underline{\widetilde{\tau}}_k$ is the trial solution achieved at the step k by the iterative updating procedure.

As far as the updating strategies are concerned, many approaches have been developed. Simulated Annealing [61] is one of the first and most common single agent algorithm (i.e., $W = 1$). The basis idea is to define $\underline{\underline{\mathcal{U}}}_k$ according to a *"temperature parameter"* that incrementally decreases at each iteration converging to a stable condition. However, the smaller the update becomes, the lesser the hill-climbing[1] capability is.

In order to increase the hill-climbing capabilities, multiple agent techniques (i.e., $W > 1$) have been also adopted. Some

[1]The hill-climbing capability refers to the possibility of dealing with multi-minima cost function, without the solution being trapped in a local minima.

well known examples are the Genetic-Algorithms (GA) [62]-[64] [21] and the Particle Swarm Optimizer (PSO) [65]. In GA, a population of trial solution is defined and it is evolved by mimicing Darwin's evolution theory by means of a set of updated operators, known as *selection*, *crossover*, and *mutation* [66]. The procedure is based on a *competitive* process aimed at extracting the best individual among the population. On the contrary, the PSO is based on a *cooperative* logic inspired by the behavior of flocks of birds looking for food [67][68]. Each particle (i.e., trial solution) collects information and makes it available to the whole swarm in order to cooperate in searching the global minimum. As a matter of fact, the update term $\underline{\underline{\mathcal{U}}}_k$ is characterized by a *"personal"* term and a *"social"* term.

Evolutionary techniques are much more demanding than the deterministic procedures in terms of computational resources, but they provide a suitable exploitation of the *a-priori* information together with an efficient representation of the solution space.

3.3 State-of-the-Art on Multi-Resolution Approaches

In order to deal with the ill-posedness of the inverse scattering problems, many approaches to collect a greater amount of information have been considered. More in detail, multi-illumination [69] and/or multi-view [70] and/or multi-source [71] and/or multi-frequency systems [72] are generally used,

but the information collectable from the scattering experiments still remains limited [13] to an upper bound that depends on the geometrical characteristics of the imaging system and on the working frequency [12]. In order to reduce the dimension of the space of unknowns, some *a-priori* information (when available) on the scenario under test [73][40] can be added by imposing a set of constraints [15] on the retrievable dielectric profile.

In order to restore the "well-position" of the inverse problem, a different approach consists in fully exploiting all available information on the scenario under test. In more detail, the representation of the unknown scatterer belongs to a finite dimensional space, whose dimension is smaller than the essential dimension of data (i.e., the number of retrievable unknowns should be lower than the amount of information in data). Because of the analytical nature of the scattering operator, such an optimal dimension is a known quantity since it depends on the extension of the investigation domain with respect to the wavelength [74] and on the characteristics of the acquisition system [12]. Starting from these considerations and since the scattered field is a spatial band-limited function, the optimal numbers of views V and of measurement points M depend on the size of the investigation domain. As a matter of fact, the degrees of freedom of the field scattered by an obstacle located in free space is [15]

$$\mathcal{R}_f = 2\kappa_0\alpha \tag{3.8}$$

where α is the radius of the minimum circle enclosing the scatterer. Moreover, the number $\mathcal{I}$ of independent measurements

that can be collected, starting from the number of total measurement (i.e., $M \times V$), is $\mathcal{I} = \mathcal{R}_f^2/2$. Consequently, when $M \times V$ measurements are available, the optimal number N_{opt} of unknowns (i.e., independent equations) to be allocated is given as

$$N_{opt} = \min\{\mathcal{I},\ M \times V/2\}\ . \tag{3.9}$$

Unfortunately, the optimal number N_{opt} of retrievable unknowns (equal to the essential dimension of the scattered data) does not usually meet the criterion given in [39] for a suitable representation (in terms of spatial resolution) for both the dielectric profile of the scatterer and the induced electric field.

In order to suitably represent the unknowns and keep the ratio between unknown and data, namely $N_{opt}/(M \times V)$, small and constant during the inversion procedure, a more effective representation of the problem unknown should be adopted. A possible solution consists in the use of multi-resolution meshes, by decreasing the size of the sub-domains where the targets are located and using a coarse resolution level otherwise [75]. According to such a basic idea, various strategies based on a multi-resolution expansion of the unknowns have been proposed. These methods define discretization schemes and corresponding tailored basis functions to better represent the geometry under test (i.e., higher resolution level near the discontinuities and coarse grid in the external homogeneous background). Taking advantage of such a kind of expansion, it is possible to distribute in a non-uniform fashion the unknowns inside the scattering domain (for more details see [76][77]).

3.3.1 Wavelet-based multi-resolution approaches

In order to better allocate the number of unknowns of the inverse problem, a statistical model is employed in [17] to gather information on the suitable resolution levels to be adopted in a linear inverse problem. In practice, the *relative error covariance matrix* (*RECM*) provides a rational basis for dealing with resolution/accuracy trade-offs and to identify the optimal spatial resolution. As a matter of fact, such an approach is able to identify those regions in space where the information provided by data is higher, thus increasing the spatial resolution by means of wavelet decomposition of the signals. The arising inverse scattering problem is then recast into the minimization of a two-term cost function enforcing fidelity to scattering data and matching with the statistical prior model for the contrast, respectively. As a consequence, the inverse problem is regularized through the multiscale approach that allows the collection of *a-priori* information.

A similar approach has been considered in [16]. Starting from *a-priori* considerations on the mathematical nature of the problem and from the intrinsic features exhibited by the class of retrievable functions, such a multi-resolution strategy associates part of the optimal number of unknowns N_{opt} to a coarse representation of the whole domain. Then, it concentrates the remaining ones in those parts of the region under test where a better resolution can be achieved. Mathematically, the arising problem is solved through the minimization (only once) of a cost function related to the scattering equa-

tions. Furthermore, the unknowns are represented with the *a-priori* multi-resolution expansion by considering a suitable wavelet transformation.

3.3.2 Adaptive Multiscale Techniques

A different approach based on a step-wise refinement procedure is developed [78] for a nonlinear scattering model. A sequence of different tests based on *a-priori* hypotheses (i.e., a collection of anomaly configurations) are employed first to localize anomalous behaviors in large areas and then to refine these initial estimates in order to better characterize the actual structures. The proposed stable coarse-to-fine localization method defines a decomposition procedure (able to zoom on strong scatterers before refining other structures) and a pruning step to remove unreliable candidate anomalies. In further works (for details see [18] and referred works), a different approach based on an adaptive iterative strategy is proposed to improve spatial resolution by means of spline pyramids. Finally, the multiscale distribution of the contrast is determined by adding detail close to the surface and defining a coarse scale deeper into the the material, pruning away unnecessary degrees of freedom.

3.3.3 The Iterative Multi-Scaling Approach

In the framework of adaptive multi-resolution approaches, *Caorsi et al.* developed an iterative technique, called iterative multi-scaling approach (*IMSA*), where the distribution of the un-

knowns is *a-posteriori* determined by exploiting the information gathered during the multi-step procedure [79]. Taking advantage of a constant multi-scaling piece-wise pulse representation able to deal with all possible multi-resolution combinations (unlike wavelet expansion), such an approach is aimed at determining firstly the regions-of-interest (*RoIs*) where the scatterers are located, thus increasing the spatial resolution only where needed. The amount of information collected through the field measurements is suitably exploited by allowing an enhanced spatial resolution only in the *RoIs* and keeping the ratio $N_{opt}/(M \times V)$ low according to the criterion previously discussed. As a consequence, the risk for the solution of being trapped in a local minima is sensibly reduced [15], even though it cannot be fully removed.

At each step of the iterative procedure, the reconstruction is performed through the minimization of a suitable multi-resolution cost function. The process is iterated until the unknowns' distribution reaches a stationary condition. The operations characterizing each step s, $s = 1, ..., S$, of the *IMSA* can be summarized as follows (for more details, see [79]):

- ***Multi-Resolution Expansion*** - The representation of the unknowns is updated according to the new resolution level s, $s = 1, ..., S$, by means of the following multi-resolution expansion

$$\widetilde{\tau}\left(\underline{r}\right) = \sum_{i=1}^{s} \sum_{n_i=1}^{N} \widetilde{\tau}_{n_i} \mathcal{B}\left(\underline{r}_{n_i}\right) \ , \quad \underline{r} \in D_I \tag{3.10}$$

where $\mathcal{B}\left(\underline{r}_{n_i}\right)$ is a rectangular basis function whose support is the n_i-th sub-domain of the region of interest R_i at the i-th resolution level, $i = 1, ..., S$.

- ***Multi-Resolution Profile Retrieval*** - Minimize the multi-resolution cost function at the resolution level s, given as

$$\Phi\left\{\widetilde{\underline{\chi}}_s\right\} = \alpha \frac{\left\|\underline{\xi} - \sum_{i=1}^{s} \underline{\underline{G}}^i_{EXT} \widetilde{\underline{\tau}}_i \widetilde{\underline{E}}_i\right\|^2}{\left\|\underline{\xi}\right\|^2} + \beta \frac{\left\|\sum_{i=1}^{s} \left[\underline{\zeta}_i - \widetilde{\underline{E}}_i + \underline{\underline{G}}^i_{INT} \widetilde{\underline{\tau}}_i \widetilde{\underline{E}}_i\right]\right\|^2}{\left\|\sum_{i=1}^{s} \underline{\zeta}_i\right\|^2} \tag{3.11}$$

by considering the multi-resolution representation for the unknowns, namely $\widetilde{\underline{\chi}}_s = \left\{\left[\widetilde{\tau}\left(\underline{r}_{n_s}\right), E^v\left(\underline{r}_{n_s}\right)\right]; \quad n_s = 1, ..., N;\ i = 1, ..., s\right\}$. At each resolution level, the Green's functions $\underline{\underline{G}}^i_{EXT}$ and $\underline{\underline{G}}^i_{INT}$, $i = 1, ..., s$, need to be recomputed (for more detail see [79]).

- ***Update of the Resolution Level*** - The resolution level is updated ($s \leftarrow s + 1$).

- ***RoIs Estimation*** - The location ($\widetilde{x}^c_s$, $\widetilde{y}^c_s$) and the extension ($\widetilde{L}^c_s$) of the RoI is defined according to the *clustering procedure* described in [19], by using the previous step reconstruction image and performing a noise filtering to eliminate some artifacts in the reconstructed image [79].

- ***Termination Procedure*** - Go to "*Multi-Resolution Expansion*" until a stationary condition on the qualitative

reconstruction parameters

$$\left\{ \frac{|\Omega_{s-1} - \Omega_s|}{|\Omega_{s-1}|} \times 100 \right\} < \gamma_\Omega, \quad \Omega = \widetilde{x}^c, \widetilde{y}^c, \widetilde{L} \qquad (3.12)$$

is reached ($s = s_{opt}$), where γ_Ω are fixed thresholds experimentally determined.

The multi-scaling procedure has shown to be effective also when dealing with multiple scatterers [19][80][81]. The proposed *clustering procedure* is able to manage different non-connected *RoI*s with a satisfactory accuracy.

3.4 Shape-Optimization Algorithms

In order to properly address the ill-posedness of the inverse scattering problem, the full exploitation of whole amount of information content appears as a key issue. That can be provided though multi-resolution methodologies which allows to keep the ratio between unknowns and data low during the inversion process. In addition, several approaches, such as *IMSA* (Sect. 3.3.3), increase the information content step-by-step, providing an iteratively-increasing amount of *a-priori* information about the proper spatial resolution to be employed. However, multi-resolution techniques are not generally aimed at taking into account the *a-priori* information about the geometry at hand. As a matter of fact, many practical imaging problems can be reduced to the search of homogeneous objects inside known host media (Sect. 2.1.2), by assuming that the

electromagnetic properties of the targets are *a-priori* known [5]-[8]. In such a case, the inverse scattering problem is limited to a *qualitative imaging* problem, where only the search of location and shape of the targets is carried out, unlike standard *quantitative imaging* problems [11], where the estimation of the electrical conductivity and permittivity values is required.

To profitably exploit the *a-priori* information about the scatterers, shape-optimization algorithms can be considered as effective strategies to solve *qualitative imaging* problems. In the following, a brief state-of-the-art about these methodologies is provided, focusing basically on two classes: the parametric approaches [21]-[25], where the target is represented by a set of parameters, and the level-set-based strategies [31]-[32] [82], where the shape of the scatterer is identified by the zero-level of a continuous function.

3.4.1 Parametric Approaches

Starting from the knowledge of the unperturbed geometry and of the electromagnetic properties of the media, the targets to be retrieved can be profitably defined as inclusions in a known structure and approximated with a limited set of essential parameters [21]. Such a parametrization and the use of a suitable Green's function [73] allow a reduction of the number of unknowns and consequently a non-negligible computational saving during the reconstruction process carried out in terms of the optimization of a suitable cost function.

In general, these shape-optimization strategies describe the targets as basic shapes, such as rectangular domains, to be

properly parametrized. More in detail, by considering some *a-priori* assumptions, the scatterer is defined by the coordinates of its center (x_c, y_c), its length L, its side W, and the orientation θ. Therefore, the value of the contrast function in the n-th sub-domain, $n = 1, ..., N$, can be re-defined according to the following relationship

$$\tau_n = \begin{cases} \tau_C & \text{if} \mathcal{P} \in \left[-\frac{L}{2}, \frac{L}{2}\right] \text{ and } \mathcal{Q} \in \left[-\frac{W}{2}, \frac{W}{2}\right] \\ 0 & \text{otherwise} \end{cases} \tag{3.13}$$

where

$$\mathcal{P} = (x_n - x_c)\cos\theta + (y_n - y_c)\sin\theta \tag{3.14}$$

and

$$\mathcal{Q} = (x_n - x_c)\sin\theta + (y_n - y_c)\cos\theta\,. \tag{3.15}$$

Accordingly, the set of parameters to be retrieved during the reconstruction process is

$$\underline{\chi} = \{(x_c, y_c)\,,\, L,\, W,\, \theta;\, E^v\left(\underline{r}_n\right),\, n = 1, ..., N\} \tag{3.16}$$

where the total electric field $E^v\left(\underline{r}_n\right)$ can be updated by means of effective forward solvers [83] or estimated during the optimization process.

In order to determine the optimal solution $\underline{\chi}_{opt}$ of the reconstruction problem, the problem at hand is recast as an optimization one via the definition of a suitable cost function

$$\begin{aligned} \Phi\left\{\underline{\chi}\right\} = \alpha \frac{\left\|\underline{\xi} - \underline{\underline{G}}_{EXT}\aleph\left(\underline{\chi}\right)\right\|^2}{\left\|\underline{\xi}\right\|^2} \\ + \beta \frac{\left\|\underline{\zeta} - \underline{\widetilde{E}} + \underline{\underline{G}}_{INT}\aleph\left(\underline{\chi}\right)\right\|^2}{\left\|\underline{\zeta}\right\|^2} \end{aligned} \tag{3.17}$$

where $\aleph\left(\underline{\chi}\right) = \widetilde{\underline{\tau}}\left(\underline{\chi}\right)\widetilde{\underline{E}}\left(\underline{\chi}\right)$ is the equivalent current density computed starting from $\underline{\chi}$. Due to the discrete nature of the array of unknowns, the resulting minimization procedure is usually solved by means of evolutionary optimization approaches, such as *GA*. As for the use of more complex parametrization schemes, such as spline functions, it usually requires customized strategies [23][24].

3.4.2 Level-Set-based Shape Optimization

Since 1988 when the paper of *Osher* and *Sethian* [29] appeared in the literature, level set methods are considered effective techniques for dealing with propagating fronts and interfaces [32]. Such methodologies have been successfully exploited in many frameworks, such as modelling and simulation [84] and inverse problems [85]-[87], or more specifically in imaging [88]-[90], medical applications [91]-[94], and geology [95].

More in detail, once the effectiveness of these optimization strategies has been proved for the retrieval of position and shape of unknowns targets [31], they have been also used in electromagnetics, for inverse scattering problems [33][34] [97]-[98]. In such a framework, the first works were mainly focused on "binary" geometries, where the permittivity and conductivity of targets and background were assumed to be *a-priori* known, thus turning the inverse scattering problem into a *qualitative imaging* problem, where only the shape of the scatterer has to be reconstructed. However, recent advances deal with more complex problems, such as the retrieval of the values of the "binary" contrast function, the recovery of the support of

several targets, or more complex geometries [20][99].

As for the main aspect of level-set-based optimization, the contrast function is defined with respect to the shape Υ of the scatterer as follows

$$\tau\left(\underline{r}\right) = \begin{cases} \tau_C & \phi\left(\underline{r}\right) \leq 0 \quad \text{and} \quad \underline{r} \in \Upsilon \\ 0 & \phi\left(\underline{r}\right) > 0 \quad \text{and} \quad \underline{r} \notin \Upsilon \end{cases} \tag{3.18}$$

where ϕ is a continuous function, called level set, and the contour of Υ is identified by $\phi = 0$. In order to retrieve the optimal shape Υ_{opt} of the reconstruction problem, the level set algorithm starts from an initial guess $\Upsilon_{k=1}$ and iteratively performs the following sequence of operations ($k = 1, ..., K$ being the iteration index):

- ***Update of the Field Distribution*** - The values of the scattered field $\underline{\xi}_k\left(\underline{r}_m\right)$, $m = 1, ..., M$ with $\underline{r}_m \in D_O$, and of the total field $\underline{E}_k\left(\underline{r}\right)$, $\underline{r} \in D_I$, are computed starting from $\phi_k\left(\underline{r}\right)$ and $\tau_k\left(\underline{r}\right)$ by solving a forward scattering problem.

- ***Gradient Computation*** - The shape derivative $\nabla_\Upsilon \Theta\left\{\phi_k\right\}$ of the cost function

$$\Theta\left\{\phi_k\right\} = \left\| \underline{\xi} - \underline{\underline{G}}_{EXT} \underline{\tau}_k\left(\phi_k\right) \underline{E}_k\left(\phi_k\right) \right\|^2 \tag{3.19}$$

  is computed in order to get a velocity function $\underline{\mathcal{V}}_k\left(\underline{r}\right)$ for the update of the level set function. $\underline{\mathcal{V}}_k\left(\underline{r}\right)$ can be obtained by calculating the Eulerian derivative of (3.19) [32] or similarly by solving an adjoint problem [33]. More details about the adjoint problem for the two-dimensional TM case are given in Appendix A.

- ***Iteration Update*** - The iteration index is updated ($k \leftarrow k+1$).

- ***Level Set Update*** - The level set function ϕ_k is updated according to the following relationship

$$\phi_k\left(\underline{r}\right) = \phi_{k-1}\left(\underline{r}\right) + \nu_{k-1}\mathcal{U}_{k-1}\left(\underline{r}\right) \tag{3.20}$$

  where $\mathcal{U}_{k-1}$ is the update term and ν_{k-1} is the step size which can be determined by a line-search strategy. When $\mathcal{U}_{k-1}\left(\underline{r}\right)$ is chosen as

$$\mathcal{U}_{k-1} = \left|\nabla\phi_{k-1}\right| \underline{\mathcal{V}}_{k-1} \cdot \underline{\hat{\mathbf{n}}}\,, \tag{3.21}$$

  with $\underline{\hat{\mathbf{n}}} = \nabla\phi_{k-1} / \left|\nabla\phi_{k-1}\right|$, relationship (3.20) is a Hamilton-Jacobi-type equation.

Since the updates $\mathcal{U}_k$ could provide rough boundaries of the trial shape Υ_k, $k = 1, ..., K$, regularization strategies for shape inversion are often considered [32][87]. Such techniques consist in employing smoothing operators (e.g., by assuming that the solution belongs to a particular function space consisting of smooth functions) or penalization terms based on the desired geometric properties of the trial solutions. These constraints can be determined through the analysis of the data at hand and of the achievable resolution.

Chapter 4

The Multi-Resolution Level Set Approach

In this chapter, the iterative multi-scaling approach with level-set-based optimization is presented. The mathematical formulation is focused on the multi-step architecture and the proposed numerical validation, carried out both with numerical synthesized data and laboratory-controlled data, discusses the reconstruction capabilities of the proposed multi-resolution methodology by considering simple and complex targets.

4.1 Mathematical Formulation

With reference to Ch. 2 where the inverse scattering problem has been mathematically formulated, this section is aimed at presenting the integration of the iterative multi-scaling strategy (*IMSA*) and the level-set (*LS*) representation. Let us consider a cylindrical homogeneous non-magnetic object with relative permittivity ϵ_C and conductivity σ_C that occupies a region Υ belonging to an investigation domain D_I. Such a scatterer is probed by a set of V transverse-magnetic (TM) plane waves, with electric field $\underline{\zeta}^v(\underline{r}) = \zeta^v(\underline{r})\hat{\underline{z}}$ ($v = 1, \ldots, V$), $\underline{r} = (x, y)$, and the scattered field, $\underline{\xi}^v(\underline{r}) = \xi^v(\underline{r})\hat{\underline{z}}$, is collected at $M(v)$, $v = 1, ..., V$, measurement points $\underline{r}_{m(v)}$ distributed in the observation domain D_O.

In order to retrieve the unknown position and shape of the target Υ by step-by-step enhancing the spatial resolution only in that region, called region-of-interest (RoI), $R \in D_I$, where the scatterer is located [19], the following iterative procedure of S_{max} steps is carried out.

With reference to Fig. 4.1(a) and to the block diagram displayed in Fig. 4.2, at the first step ($s = 1$, s being the step number) a trial shape $\Upsilon_s = \Upsilon_1$, belonging to D_I, is chosen and the region of interest R_s [$R_{s=1} = D_I$] is partitioned into N_{IMSA} equal square sub-domains, N_{IMSA} being the number of degrees of freedom of the problem at hand [14]. In addition, the level set function ϕ_s is initialized as follows [33][97]:

$$\phi_s\left(\underline{r}_{n_s}\right) = \begin{cases} -\min_{b=1,\ldots,B_s}\left\{d_{n_s b}\right\} & \text{if } \tau\left(\underline{r}_{n_s}\right) = \tau_C \\ \min_{b=1,\ldots,B_s}\left\{d_{n_s b}\right\} & \text{if } \tau\left(\underline{r}_{n_s}\right) = 0 \end{cases} \tag{4.1}$$

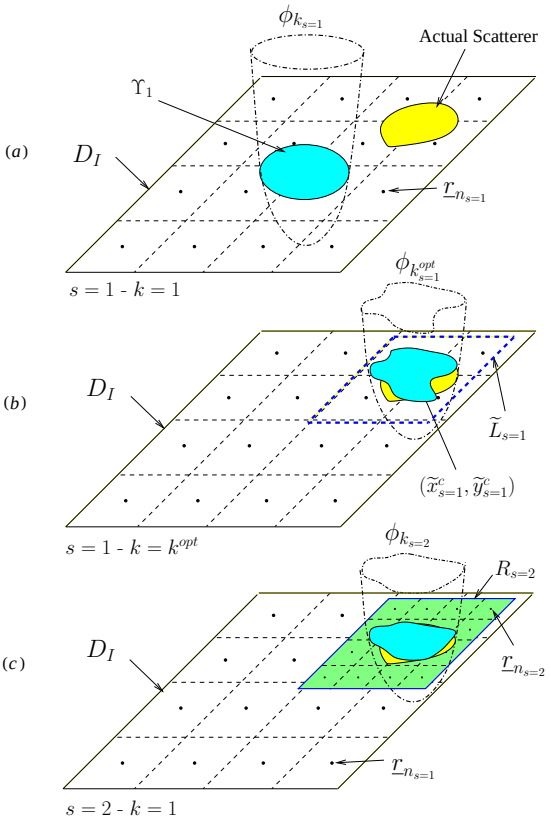

Figure 4.1: Graphical representation of the *IMSA-LS* zooming procedure. (a) First step ($k = 1$): the investigation domain is discretized in N sub-domains and a coarse solution is looked for. (b) First step ($k = k^{opt}$): the region of interest that contains the first estimate of the object is defined. (c) Second step ($k = 1$): an enhanced resolution level is used only inside the region of interest.

where $d_{n_s,b} = \sqrt{(x_{n_s} - x_b)^2 + (y_{n_s} - y_b)^2}$, $\underline{r}_{n_s} = (x_{n_s}, y_{n_s})$ and $\underline{r}_b = (x_b, y_b)$ are the center of the n_s-th pixel and the b-th border-cell ($b = 1, \ldots, B_s$) of Υ_1, respectively.

Then, at each step s of the process ($s = 1, ..., S_{max}$), the following optimization procedure is repeated (Fig. 4.2):

- ***Problem Unknown Representation*** - The contrast function is represented in terms of the level set function as follows

$$\widetilde{\tau}_{k_s}(\underline{r}) = \sum_{i=1}^{s} \sum_{n_i=1}^{N_{IMSA}} \tau_{k_i} \mathcal{B}\left(\underline{r}_{n_i}\right) \quad \underline{r} \in D_I \tag{4.2}$$

  where the index k_s indicates the k-th iteration at the s-th step [$k_s = 1, ..., k_s^{opt}$], $\mathcal{B}\left(\underline{r}_{n_i}\right)$ is a rectangular basis function whose support is the n-th sub-domain at the i-th resolution level [$n_i = 1, ..., N_{IMSA}$, $i = 1, ..., s$], and the coefficient τ_{k_i} is given by

$$\tau_{k_i} = \begin{cases} \tau_C & \text{if } \Psi_{k_i}\left(\underline{r}_{n_i}\right) \leq 0 \\ 0 & \text{otherwise} \end{cases} \tag{4.3}$$

  letting

$$\Psi_{k_i}\left(\underline{r}_{n_i}\right) = \begin{cases} \phi_{k_i}\left(\underline{r}_{n_i}\right) & \text{if } i = s \\ \phi_{k_i^{opt}}\left(\underline{r}_{n_i}\right) & \text{if } (i < s) \text{ and } \left(\underline{r}_{n_i} \in R_i\right) \end{cases} \tag{4.4}$$

  with $i = 1, ..., s$ as in (4.2).

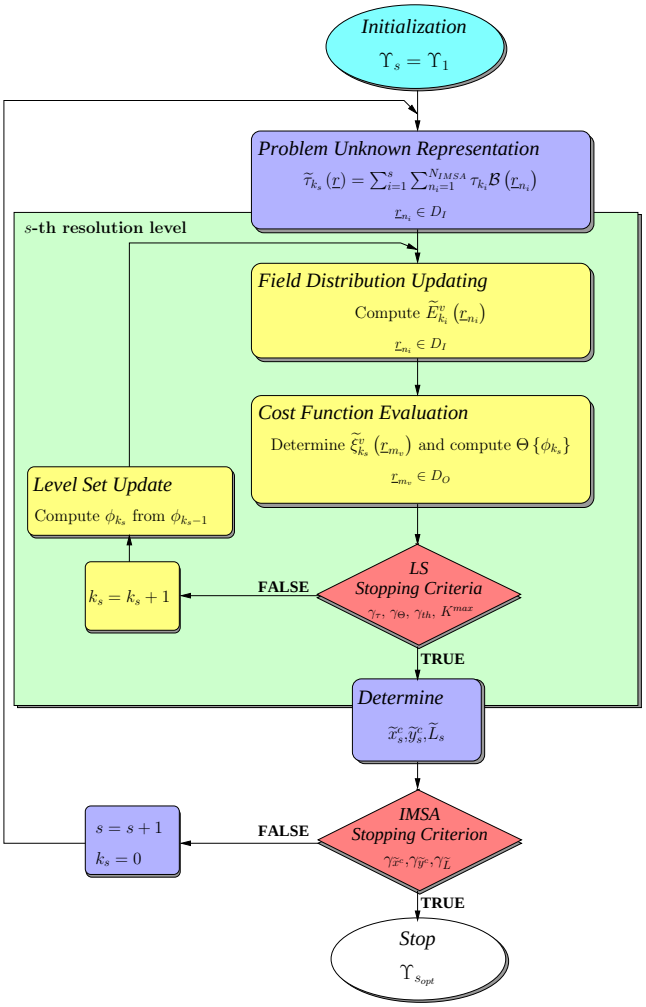

Figure 4.2: Block diagram description of the *IMSA-LS* zooming procedure.

- ***Field Distribution Updating*** - Once $\widetilde{\tau}_{k_s}(\underline{r})$ has been estimated, the electric field $E^v_{k_s}(\underline{r})$ is numerically computed according to a point-matching version of the Method of Moments (MoM) [39] as

$$\widetilde{E}^v_{k_i}\left(\underline{r}_{n_i}\right) = \sum_{p_i=1}^{N_{IMSA}} \zeta^v\left(\underline{r}_{p_i}\right)\left[1-\widetilde{\tau}_{k_i}\left(\underline{r}_{p_i}\right) G_{2D}\left(\underline{r}_{n_i}/\underline{r}_{p_i}\right)\right]^{-1}, \quad \begin{array}{r} \underline{r}_{n_i}, \underline{r}_{p_i} \in D_I \\ n_i = 1, ..., N_{IMSA} \end{array}. \tag{4.5}$$

- ***Cost Function Evaluation*** - Starting from the total electric field distribution (4.5), the reconstructed scattered field $\widetilde{\xi}^v_{k_s}\left(\underline{r}_{m(v)}\right)$ at the $m(v)$-th measurement point, $m(v) = 1, ..., M(v)$, is updated by solving the following equation

$$\widetilde{\xi}^v_{k_s}\left(\underline{r}_{m(v)}\right) = \sum_{i=1}^{s}\sum_{n_i=1}^{N_{IMSA}} \widetilde{\tau}_{k_i}\left(\underline{r}_{n_i}\right)\widetilde{E}^v_{k_i}\left(\underline{r}_{n_i}\right) G_{2D}\left(\underline{r}_{m(v)}/\underline{r}_{n_i}\right) \tag{4.6}$$

and the fit between measured and reconstructed data is evaluated by the multi-resolution cost function Θ defined as

$$\Theta\left\{\phi_{k_s}\right\} = \frac{\sum_{v=1}^{V}\sum_{m(v)=1}^{M(v)}\left|\widetilde{\xi}^v_{k_s}\left(\underline{r}_{m(v)}\right) - \xi^v_{k_s}\left(\underline{r}_{m(v)}\right)\right|^2}{\sum_{v=1}^{V}\sum_{m(v)=1}^{M(v)}\left|\xi^v_{k_s}\left(\underline{r}_{m(v)}\right)\right|^2}. \tag{4.7}$$

- ***Minimization Stopping*** - The iterative process stops [i.e., $k_s^{opt} = k_s$ and $\widetilde{\tau}_s^{opt} = \widetilde{\tau}_{k_s}$] when: (a) a set of conditions on the stability of the reconstruction holds true or (b) when the maximum number of iterations is reached $[k_s = K_{max}]$, or (c) when the value of the cost function is smaller than a fixed threshold γ_{th}. As far as the stability of the reconstruction is concerned [condition (a)], the first corresponding stopping criterion is satisfied when, for a fixed number of iterations, K_τ, the maximum number of pixels, the value of which has changed, becomes smaller than a user-defined threshold γ_τ according to the relationship

$$\max_{j=1,\ldots,K_\tau} \left\{ \sum_{n_s=1}^{N_{IMSA}} \frac{\left| \widetilde{\tau}_{k_s}\left(\underline{r}_{n_s}\right) - \widetilde{\tau}_{k_s-j}\left(\underline{r}_{n_s}\right) \right|}{\tau_C} \right\} < \gamma_\tau \cdot N_{IMSA}. \tag{4.8}$$

The second criterion, about the stability of the reconstruction, is satisfied when the cost function becomes stationary within a window of K_Θ iterations as follows:

$$\frac{1}{K_\Theta} \sum_{j=1}^{K_\Theta} \frac{\Theta\left\{\phi_{k_s}\right\} - \Theta\left\{\phi_{k_s-j}\right\}}{\Theta\left\{\phi_{k_s}\right\}} < \gamma_\Theta. \tag{4.9}$$

K_Θ being a fixed number of iterations and γ_Θ being user-defined thresholds;. When the iterative process stops, the solution $\widetilde{\tau}_s^{opt}$ at the s-th step is selected as the one represented by the "best" level set function ϕ_s^{opt} defined as

$$\phi_s^{opt} = \arg\left[\min_{h=1,\ldots,k_s^{opt}} \left(\Theta\left\{\phi_h\right\}\right)\right]. \tag{4.10}$$

- ***Iteration Update*** - The iteration index is updated $[k_s \rightarrow k_s + 1]$;

- ***Level Set Update*** - The level set is updated according to the following Hamilton-Jacobi relationship

$$\phi_{k_s}\left(\underline{r}_{n_s}\right) = \phi_{k_s-1}\left(\underline{r}_{n_s}\right) - \Delta t_s \mathcal{V}_{k_s-1}\left(\underline{r}_{n_s}\right) \mathcal{H}\left\{\phi_{k_s-1}\left(\underline{r}_{n_s}\right)\right\} \tag{4.11}$$

where $\mathcal{H}\{\cdot\}$ is the Hamiltonian operator [29][30] given as

$$\mathcal{H}^2\left\{\phi_{k_s}\left(\underline{r}_{n_s}\right)\right\} = \begin{cases} \max^2\left\{\mathcal{D}_{k_s}^{x-};0\right\} + \min^2\left\{\mathcal{D}_{k_s}^{x+};0\right\} + \\ \quad +\max^2\left\{\mathcal{D}_{k_s}^{y-};0\right\} + \min^2\left\{\mathcal{D}_{k_s}^{y+};0\right\} \\ \quad \text{if } \mathcal{V}_{k_s}\left(\underline{r}_{n_s}\right) \geq 0 \\ \\ \min^2\left\{\mathcal{D}_{k_s}^{x-};0\right\} + \max^2\left\{\mathcal{D}_{k_s}^{x+};0\right\} + \\ \quad +\min^2\left\{\mathcal{D}_{k_s}^{y-};0\right\} + \max^2\left\{\mathcal{D}_{k_s}^{y+};0\right\} \\ \quad \text{otherwise} \end{cases} \tag{4.12}$$

with

- $\mathcal{D}_{k_s}^{x\pm} = \frac{\pm\phi_{k_s}(x_{n_s}\pm 1, y_{n_s}) \mp \phi_{k_s}(x_{n_s}, y_{n_s})}{l_s}$,
- $\mathcal{D}_{k_s}^{y\pm} = \frac{\pm\phi_{k_s}(x_{n_s}, y_{n_s}\pm 1) \mp \phi_{k_s}(x_{n_s}, y_{n_s})}{l_s}$.

Δt_s is the time-step chosen as $\Delta t_s = \Delta t_1 \frac{l_s}{l_1}$ with Δt_1 to be set heuristically according to the literature [33], l_s being the cell-side at the s-th resolution level. $\mathcal{V}_{k_s}$ is the velocity function computed following the guidelines suggested in [33] by solving the adjoint problem of (4.5) in order to

determine the adjoint field $\mathcal{F}_{k_s}^v$ (for more details, please refer to the Appendix A). Accordingly,

$$\mathcal{V}_{k_s}\left(\underline{r}_{n_s}\right) = -\Re\left\{\frac{\sum_{v=1}^{V}\tau_C E_{k_s}^v\left(\underline{r}_{n_s}\right)\mathcal{F}_{k_s}^v\left(\underline{r}_{n_s}\right)}{\sum_{v=1}^{V}\sum_{m(v)=1}^{M(v)}\left|\xi_{k_s}^v\left(\underline{r}_{m(v)}\right)\right|^2}\right\}, \qquad n_s = 1, ..., N_{IMSA} \tag{4.13}$$

where $\Re$ stands for the real part.

When the s-th minimization process terminates, the contrast function is updated $[\widetilde{\tau}_s^{opt}(\underline{r}) = \widetilde{\tau}_{k_{s-1}}(\underline{r}),\ \underline{r} \in D_I\ (4.2)]$ as well as the RoI $[R_s \rightarrow R_{s-1}]$. To do so, the center of R_s of coordinates $(\widetilde{x}_s^c, \widetilde{y}_s^c)$ is determined as follows [19] [Fig. 4.1(b)]:

$$\widetilde{x}_s^c = \frac{\sum_{i=1}^{s}\sum_{n_i=1}^{N_{IMSA}} x_{n_i}\widetilde{\tau}_s^{opt}\left(\underline{r}_{n_i}\right)\mathcal{B}\left(\underline{r}_{n_i}\right)}{\sum_{i=1}^{s}\sum_{n_i=1}^{N_{IMSA}}\widetilde{\tau}_s^{opt}\left(\underline{r}_{n_i}\right)\mathcal{B}\left(\underline{r}_{n_i}\right)} \tag{4.14}$$

$$\widetilde{y}_s^c = \frac{\sum_{i=1}^{s}\sum_{n_i=1}^{N_{IMSA}} y_{n_i}\widetilde{\tau}_s^{opt}\left(\underline{r}_{n_i}\right)\mathcal{B}\left(\underline{r}_{n_i}\right)}{\sum_{i=1}^{s}\sum_{n_i=1}^{N_{IMSA}}\widetilde{\tau}_s^{opt}\left(\underline{r}_{n_i}\right)\mathcal{B}\left(\underline{r}_{n_i}\right)}. \tag{4.15}$$

The estimated side L_s of R_s is computed as

$$\widetilde{L}_s = 2\frac{\sum_{i=1}^{s}\sum_{n_i=1}^{N_{IMSA}}\left[d_{n_i,c_s}\widetilde{\tau}_s^{opt}\left(\underline{r}_{n_i}\right)\mathcal{B}\left(\underline{r}_{n_i}\right)\right]}{\sum_{i=1}^{s}\sum_{n_i=1}^{N_{IMSA}}\left[\widetilde{\tau}_s^{opt}\left(\underline{r}_{n_i}\right)\mathcal{B}\left(\underline{r}_{n_s}\right)\right]} \tag{4.16}$$

where $d_{n_i,c_s} = \sqrt{\left(x_{n_i} - \widetilde{x}_s^c\right)^2 + \left(y_{n_i} - \widetilde{y}_s^c\right)^2}$.

Once the RoI has been identified, the level of resolution is enhanced $[k_s \rightarrow k_{s-1}]$ only in this region by discretizing R_s into

N_{IMSA} sub-domains [Fig. 4.1(c)] and by repeating the minimization process until the synthetic zoom becomes stationary ($s = s_{opt}$), i.e.,

$$\left\{ \frac{|\Omega_{s-1} - \Omega_s|}{|\Omega_{s-1}|} \times 100 \right\} < \gamma_\Omega, \quad \Omega = \widetilde{x}^c, \widetilde{y}^c, \widetilde{L} \tag{4.17}$$

γ_Q being a threshold set as in [19], or until a maximum number of steps ($s_{opt} = S_{max}$) is reached. As far as the regions outside R_s are concerned, the spatial resolution is left unchanged as defined in the previous steps ($\underline{r}_{n_i}$, $n_i = 1, ..., N_{IMSA}$, $i = 1, ..., s-1$) and the values of the problem unknowns are computed according to equation (4.4).

At the end of the multi-step process ($s = s_{opt}$), the problem solution is obtained as $\widetilde{\tau}^{opt}\left(\underline{r}_{n_i}\right) = \widetilde{\tau}_s^{opt}\left(\underline{r}_{n_i}\right)$, $n_i = 1, ..., N_{IMSA}$, $i = 1, ..., s_{opt}$.

4.2 Numerical Validation: Synthetic Data

In order to assess the effectiveness of the *IMSA-LS* approach, a selected set of representative results concerned with synthetic data is presented herein. The performances achieved are evaluated by means of the following error figures:

- *Localization Error* δ

$$\delta|_p = \frac{\sqrt{\left(\widetilde{x}_s^c|_p - x^c|_p\right)^2 - \left(\widetilde{y}_s^c|_p - y^c|_p\right)^2}}{\lambda} \times 100 \quad (4.18)$$

where $\underline{r}_c|_p = \left(x^c|_p\,,\; y^c|_p\right)$ is the center of the p-th true scatterer, $p = 1, ..., P$, P being the number of objects. The average localization error $< \delta >$ is defined as

$$< \delta >= \frac{1}{P} \sum_{p=1}^{P} \delta|_p \,. \quad (4.19)$$

- *Area Estimation Error* Δ

$$\Delta = \left[\sum_{i=1}^{I} \frac{1}{N_{IMSA}} \sum_{n_i=1}^{N_{IMSA}} \mathcal{N}_{n_i} \right] \times 100 \quad (4.20)$$

where $\mathcal{N}_{n_i}$ is equal to 1 if $\widetilde{\tau}^{opt}\left(\underline{r}_{n_i}\right) = \tau\left(\underline{r}_{n_i}\right)$ and 0 otherwise.

As far as the numerical experiments are concerned, the reconstructions have been performed by blurring the scattering data with an additive Gaussian noise characterized by a signal-to-noise-ratio (SNR)

$$SNR = 10\log\frac{\sum_{v=1}^{V}\sum_{m(v)=1}^{M(v)}\left|\xi^{v}\left(\underline{r}_{m(v)}\right)\right|^{2}}{\sum_{v=1}^{V}\sum_{m(v)=1}^{M(v)}\left|\mu^{v,m(v)}\right|^{2}} \tag{4.21}$$

$\mu^{v,m(v)}$ being a complex Gaussian random variable with zero mean value.

4.2.1 Initializing with the True Solution

In the first experiment, a lossless circular scatterer of known permittivity $\epsilon_C = 1.8$ and radius $\rho = \lambda/4$ is centered at $x^c = y^c = \lambda/6$ [33] in a square investigation domain of side $L_D = \lambda$. $V = 10\,TM$ plane waves are impinging from the directions $\theta_v = 2\pi\,(v-1)/\,V,\ v = 1, ..., V$, and the scattering measurements are collected at $M(v) = 10$ receivers uniformly distributed on a circle of radius $\rho_O = \lambda$.

As far as the initialization of the *IMSA-LS* algorithm is concerned, the initial trial object Υ_1 is the true solution sampled at the resolution level $s = 1$. The initial value of the time step is set to $\Delta t_1 = 10^{-2}$ as in [33]. The *RoI* is discretized in $N_{IMSA} = 15 \times 15$ sub-domains at each step of the iterative multi-resolution process. Concerning the stopping criteria, the following configuration of parameters has been selected according to a preliminary calibration dealing with simple known scatterers and noiseless data: $S_{max} = 4$ (maximum number of

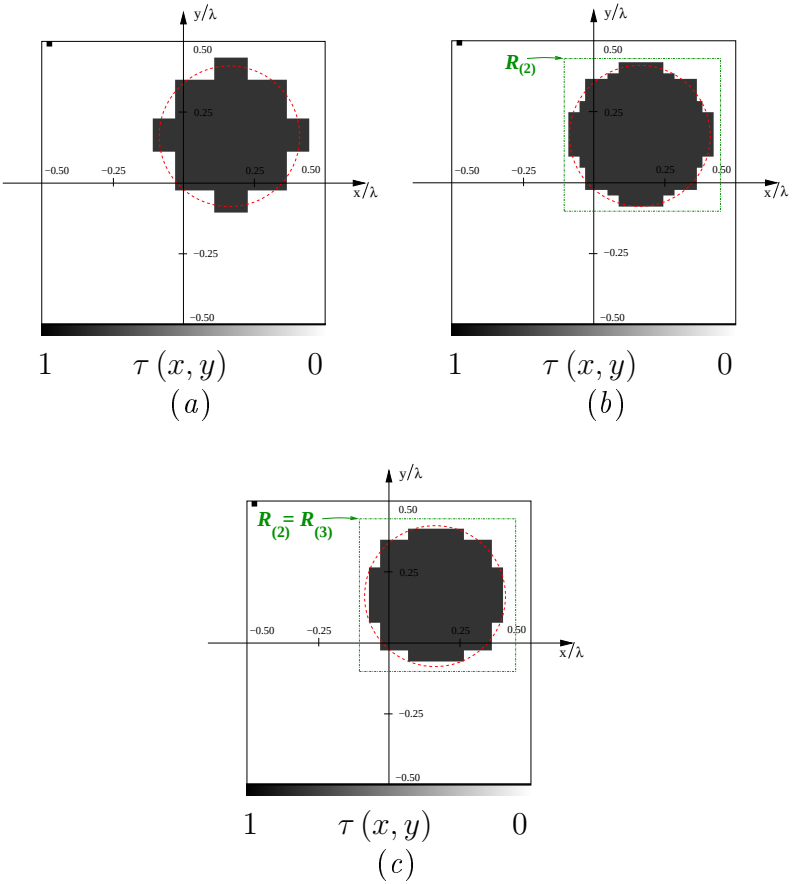

Figure 4.3: Numerical Data. Circular cylinder ($\epsilon_C = 1.8$, $L_D = \lambda$, *Noiseless Case*). Reconstructions when initializing *IMSA-LS* with the true solution $[(a)\ s = 1,\ (b)\ s = 2,$ and $(c)\ s = s_{opt} = 3]$.

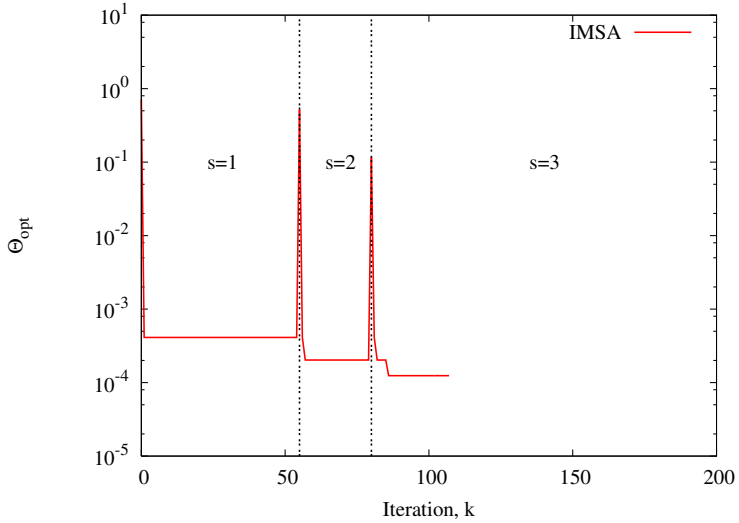

Figure 4.4: Numerical Data. Circular cylinder ($\epsilon_C = 1.8$, $L_D = \lambda$, *Noiseless Case*). Behavior of the cost function when initializing *IMSA-LS* with the true solution.

steps), $\gamma^{\widetilde{x}^c} = \gamma^{\widetilde{y}^c} = 0.01$ and $\gamma^{\widetilde{L}} = 0.05$ (multi-step process thresholds), $K_{max} = 500$ (maximum number of optimization iterations), $\gamma_\Theta = 0.2$ and $\gamma_\tau = 0.02$ (optimization thresholds), $K_\Theta = K_\tau = 0.15\,K_{max}$ (stability counters), and $\gamma_{th} = 10^{-5}$ (threshold on the cost function).

Figure 4.3 shows the reconstruction achieved at the end of the iterative steps of the multi-resolution procedure [(a) $s = 1$ - $k = k_{opt}$, (b) $s = 2$ - $k = k_{opt}$, and (c) $s = s_{opt} = 3$ - $k = k_{opt}$] while the behavior of the cost function is reported in Fig. 4.4. The regions of interest determined at steps $s = 2$ and $s = 3$ are reported on the reconstructed profile by the dashed/dotted contour [Figs. 4.3(b) and (c)].

As for the quality of the reconstructions, it is worth noting that Fig. 4.3(a) is the true object sampled at the level $s = 1$ (i.e., it is equal to the the initial guess). Then, as the resolution increases, the reconstruction improves as expected. As a matter of fact, the shape of the object reconstructed at the end of the process [Fig. 4.3(c)] appears to be better retrieved than in Figs. 4.3(a) and (b). Such an improvement is obvious also in the behavior of the cost function, since the error "jumps" to a lower value as the spatial resolution improves. For the sake of completeness, let us emphasize that the spikes of the cost function between two adjacent steps are due to the updating of the field distribution in correspondence with the new resolution level.

When dealing with noisy data, the method still converges to the exact solution, even though the quality of the reconstructions gets worse with respect to the noiseless case. Figure 4.5 shows the solutions achieved with different levels of additive

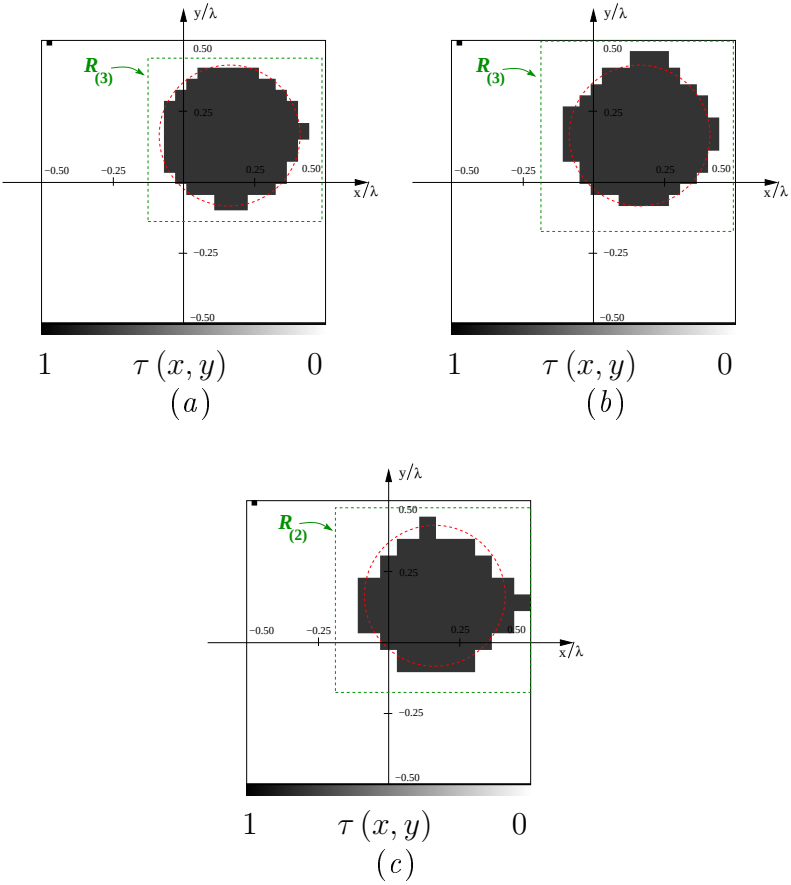

Figure 4.5: Numerical Data. Circular cylinder ($\epsilon_C = 1.8$, $L_D = \lambda$, *Noisy Case*). Reconstructions when initializing *IMSA-LS* with the true solution [(a) $SNR = 20\,dB$, (b) $SNR = 10\,dB$, and (c) $SNR = 5\,dB$] .

noise on scattered data [(a) $SNR = 20\,dB$; (b) $SNR = 10\,dB$; (c) $SNR = 5\,dB$]. The reconstructions are similar to the actual object sampled at the highest resolution level. More in detail, the symmetry of the actual object appears to be better retrieved as the noise on the data decreases. As for the behavior of the cost function (Fig. 4.6), the final error increases as the SNR increases, as expected. Moreover, the "jump" of the cost function due to the increase of the spatial resolution is less visible than in the noiseless case, and it disappears with the lowest SNR.

4.2.2 Initializing with Exact Data

For the sake of completeness, this subsection deals with the behavior of $IMSA{-}LS$ when the initial guess is the true object sampled at the same resolution level used to solve the forward problem that generates the data (i.e., the inverse crime occurs). In order to perform the inversion, the number of sub-domains has been "forced" to $N_{IMSA} = N_{direct} = 51 \times 51$, while the remaining parameters are the same of the previous section. As expected, the inversion algorithm stops immediately ($s_{opt} = 1$ - $k_{opt} = 0$), since the stopping criterion on the value of the cost function holds true. As a consequence, the reconstruction achieved is equal to the initial trial shape (Fig. 4.7).

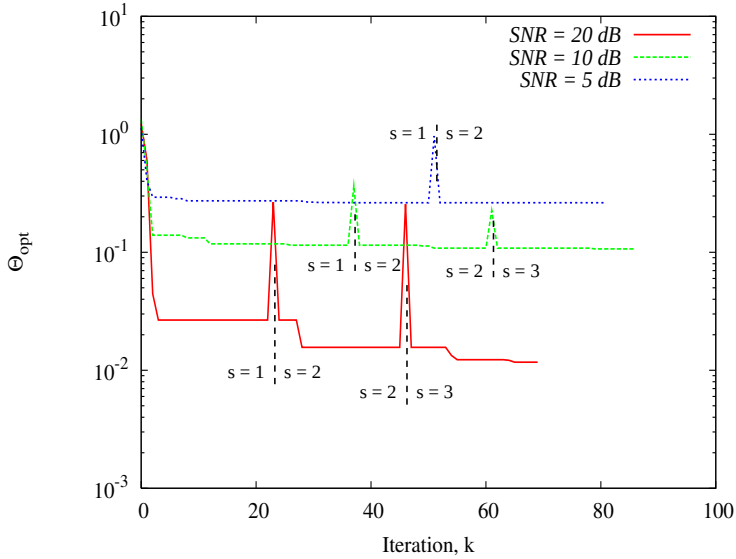

Figure 4.6: Numerical Data. Circular cylinder ($\epsilon_C = 1.8$, $L_D = \lambda$, *Noisy Case*). Behavior of the cost function when initializing *IMSA-LS* with the true solution.

4.2.3 Inversion of Data scattered by a Circular Cylinder

The first test case with an initial guess different from the true solution deals with the inversion of data scattered by the circular dielectric cylinder described in Sect. 4.2.1. In such a case, the initial trial object Υ_1 is a disk with radius $\lambda/4$ and centered in D_I while the other parameters are those selected previously.

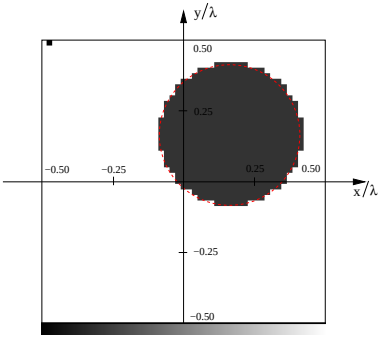

(a)

Figure 4.7: Circular cylinder ($\epsilon_C = 1.8$, $L_D = \lambda$, *Noisy Case*). Circular cylinder ($\epsilon_C = 1.8$, $L_D = \lambda$, *Noiseless Case*). Reconstructions when initializing *IMSA-LS* with the exact data.

Figure 4.8 shows samples of reconstructions with the *IMSA-LS*. At the first step [Fig. 4.8(a) - $s = 1$], the scatterer is correctly located, but its shape is only roughly estimated. Thanks to the multi-resolution representation, the qualitative imaging of the scatterer is improved in the next step [Fig. 4.8(b) - $s = s_{opt} = 2$] as confirmed by the error indexes in Tab. 4.1. For comparison purposes, the profile retrieved by the single-resolution method [33] (indicated in the following as *Bare-LS*), when D_I has been discretized in $N_{Bare} = 31 \times 31$ equal subdomains, is shown [Fig. 4.8(c)]. In general, the discretization of the *Bare-LS* has been chosen in order to achieve in

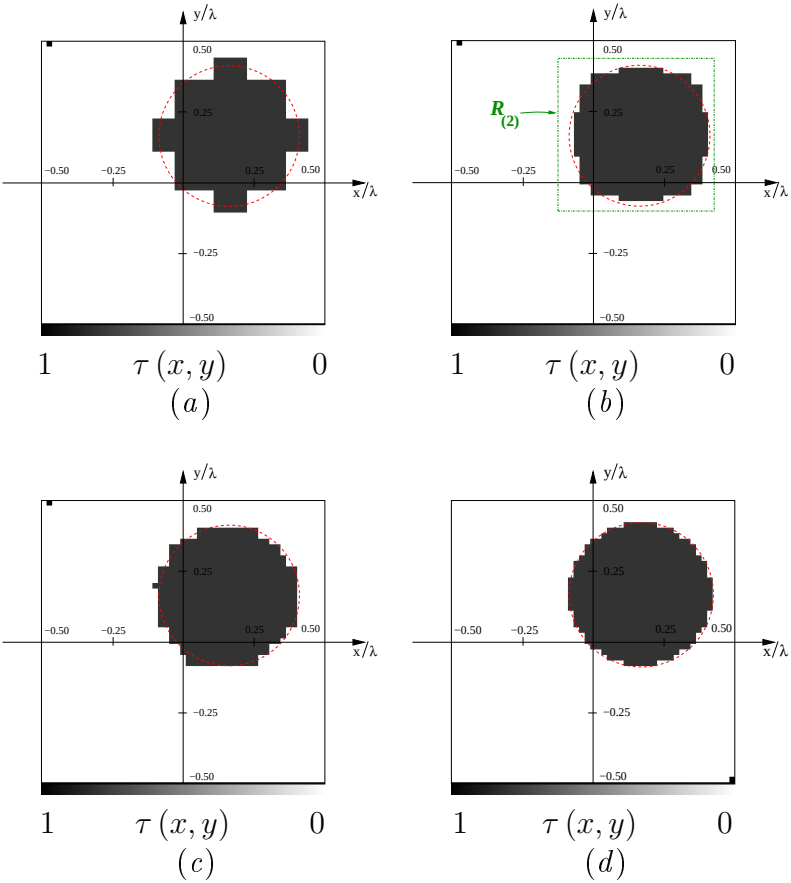

Figure 4.8: Numerical Data. Circular cylinder ($\epsilon_C = 1.8$, $L_D = \lambda$, *Noiseless Case*). Reconstructions with *IMSA-LS* at (a) $s = 1$, (b) $s = s_{opt} = 2$, (c) *Bare-LS*. Optimal inversion (d).

	$IMSA-LS$		$Bare-LS$
	$s=1$	$s=2$	
δ	6.58×10^{-6}	2.19×10^{-6}	5.21×10^{-1}
Δ	2.36	0.48	0.64

Table 4.1: Numerical Data. Circular cylinder ($\epsilon_C = 1.8$, *Noiseless Case*). Error figures.

the whole investigation domain a reconstruction with the same level of spatial resolution obtained by the *IMSA-LS* in the *RoI* at $s = s_{opt}$.

Although the final reconstructions [Figs. 4.8$(b)(c)$] achieved by the two approaches are similar and quite close to the true scatterer sampled at the spatial resolution of *Bare-LS* [Fig. 4.8(d)] and *IMSA-LS* [Fig. 4.8(b)], the *IMSA-LS* more faithfully retrieves the symmetry of the actual object, even though the reconstruction error appears to be larger than the one of the *Bare-LS* (Fig. 4.9). During the iterative procedure, the cost function $\Theta_{opt} = \Theta\{\phi_s^{opt}\}$ is initially characterized by a monotonically decreasing behavior. Then, $\Theta_{opt}\rfloor_{IMSA}$ becomes stationary until the stopping criterion defined by relationships (4.8) and (4.9) is satisfied (Fig. 4.9 - $s = 1$). Then, after the update of the field distribution inducing the error spike when $s = s_{opt} = 2$ and $k_s = 1$, $\Theta_{opt}\rfloor_{IMSA}$ settles to a value of 6.28×10^{-4} which is of the order of the *Bare-LS* error ($\Theta_{opt}\rfloor_{Bare} = 1.42\times10^{-4}$). The slight difference between $\Theta_{opt}\rfloor_{IMSA}$ and $\Theta_{opt}\rfloor_{Bare}$ depends on the different discretiza-

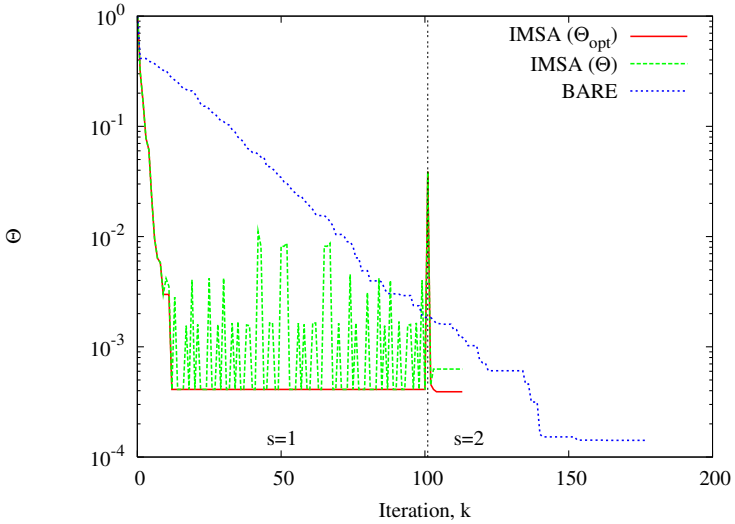

Figure 4.9: Numerical Data. Circular cylinder ($\epsilon_C = 1.8$, $L_D = \lambda$, *Noiseless Case*). Behavior of the cost function.

tion [i.e., the basis functions $\mathcal{B}\left(\underline{r}_{n(i=2)}\right)$, $n(i) = 1, ..., N_{IMSA}$ are not the same as those of *Bare-LS*], but it does not affect the reconstruction in terms of both localization and area estimation, since $\delta\rfloor_{IMSA-LS} < \delta\rfloor_{Bare-LS}$ and $\Delta\rfloor_{IMSA-LS} < \Delta\rfloor_{Bare-LS}$ (Tab. 4.1).

Fig. 4.9 also shows that the multi-step multi-resolution strategy is characterized by a lower computational burden because of the smaller number of iterations for reaching the convergence (Fig. 4.9 - $k_{tot}\rfloor_{IMSA} = 125$ vs. $k_{tot}\rfloor_{Bare} = 177$, letting k_{tot} the total number of iterations defined as $k_{tot} =$

$\sum_{s=1}^{s_{opt}} k_s^{opt}$ for the *IMSA-LS*), and especially of the reduced number of floating-point operations. As a matter of fact, since the complexity of the *LS*-based algorithms is of the order of $\mathcal{O}\left(2 \times \eta^3\right)$, $\eta = N_{IMSA}, N_{Bare}$ (i.e., the solution of two direct problems is necessary for computing an estimate of the scattered field and for updating the velocity vector), the computational cost of the *IMSA-LS* at each iteration is two orders in magnitude smaller than the one of the *Bare-LS*.

The behavior of the multi-resolution level set function Ψ_{k_s} during the inversion procedure is shown in Figs. 4.10 and 4.11. At iteration $k = 1$ of the step $s = 1$, the level set is initialized according to the oriented distance function (4.1) by considering the initial guess Υ_1. As it can be noticed from Fig. 4.10(a), the level set function is defined on the resolution level $s = 1$ and its value is lower than zero in the center of the investigation domain, namely inside the object defined by the trial solution. Then, the update of Ψ_{k_s} is carried out by means of the velocity function $\mathcal{V}_{k_s}$, whose behavior in the investigation domain at iteration $k = 1$ and at step $s = 1$ is reported in Fig. 4.12(a). After $k = 20$ iterations, the trial solution appears to be similar to the actual object, since the region where $\phi_{k_{s=1}} < 0$ is centered on the barycentre of the actual object [Fig. 4.10(b)], and the values of the velocity function are lower than at iteration $k = 1$ [Fig. 4.12(b)], especially in the region where the true scatterer is located. At the next step (i.e., $s = s_{opt} = 2$), Ψ_{k_s} at resolution level $s = 2$ is defined in the new *RoI*, while the level set at the previous resolution level, $\phi_{k_{s=1}^{opt}}$, is considered outside $R_{s=2}$. As for the update of the multi-resolution level set, the velocity function is computed only in $R_{s=2}$ [Fig. 4.13(a)] and,

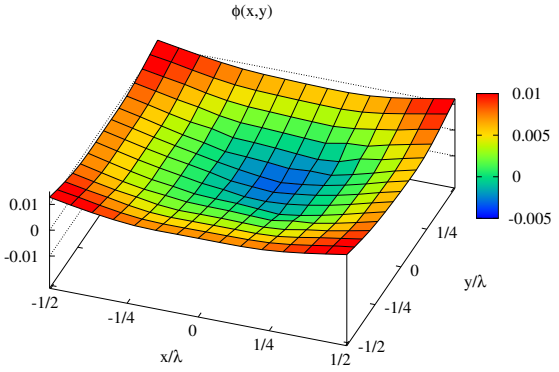

(a)

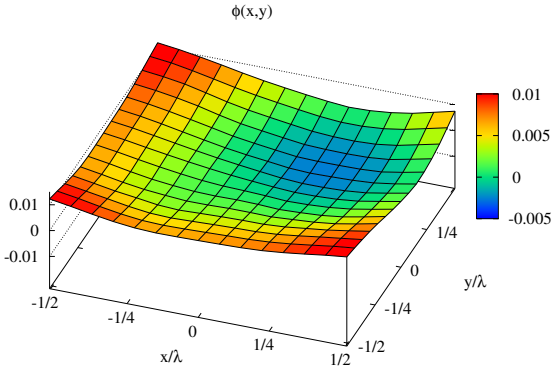

(b)

Figure 4.10: Numerical Data. Circular cylinder ($\epsilon_C = 1.8$, $L_D = \lambda$, *Noiseless Case*). Behavior of the level set ϕ_{k_s} at $s = 1$ [(a) $k = 1$, (b) $k = 20$].

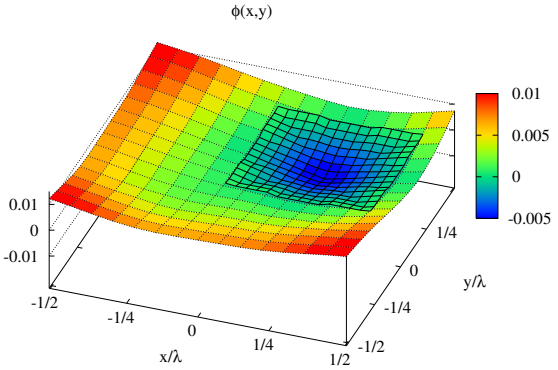

(a)

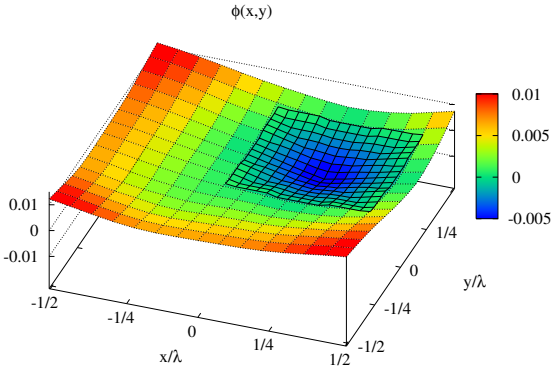

(b)

Figure 4.11: Numerical Data. Circular cylinder ($\epsilon_C = 1.8$, $L_D = \lambda$, *Noiseless Case*). Behavior of the level set ϕ_{k_s} at $s = s_{opt} = 2$ [(a) $k = 1$, (b) $k = k_{opt}$].

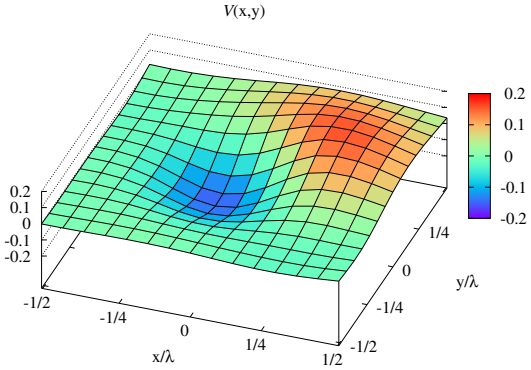

(a)

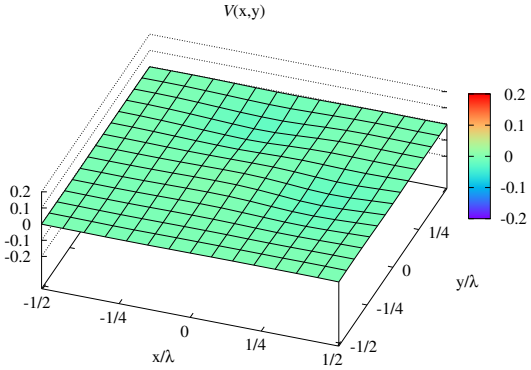

(b)

Figure 4.12: Numerical Data. Circular cylinder ($\epsilon_C = 1.8$, $L_D = \lambda$, *Noiseless Case*). Behavior of the velocity $\mathcal{V}_{k_s}$ at $s = 1$ [(a) $k = 1$, (b) $k = 20$].

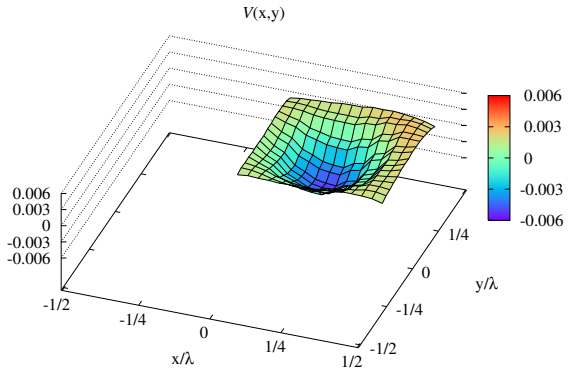

(a)

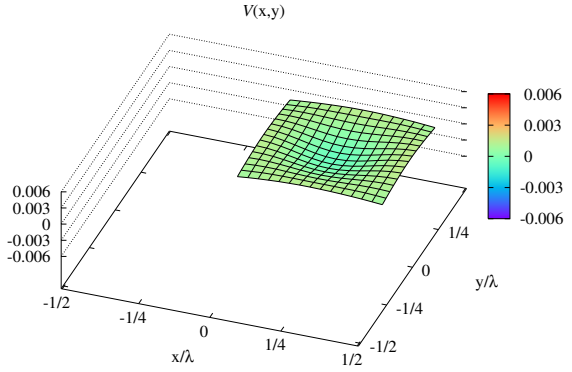

(b)

Figure 4.13: Numerical Data. Circular cylinder ($\epsilon_C = 1.8$, $L_D = \lambda$, *Noiseless Case*). Behavior of the velocity $\mathcal{V}_{k_s}$ at $s = s_{opt} = 2$ [(a) $k = 1$, (b) $k = k_{opt}$].

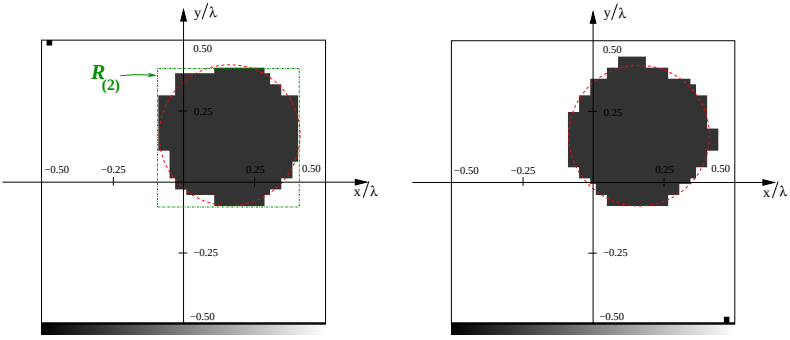

Figure 4.14: Numerical Data. Circular cylinder ($\epsilon_C = 1.8$, $L_D = \lambda$, *Noisy Case*). Reconstructions with *IMSA-LS* (a) and *Bare-LS* (b) for $SNR = 20\,dB$.

as expected, its contribution becomes more and more negligible as the iteration index $k_{s=2}$ increases [Fig. 4.13(b)].

As for the stability of the proposed approach, Figures 4.14-4.16 show the reconstructions with the *IMSA-LS* [Figs. 4.14-4.16(a)] compared to those of the *Bare-LS* [Figs. 4.14-4.16(b)] with different levels of additive noise on the scattered data [Fig. 4.14 - $SNR = 20\,dB$; Fig. 4.15 - $SNR = 10\,dB$; Fig. 4.16 - $SNR = 5\,dB$ $(bottom)$]. As expected, when the SNR decreases, the performances worsen. However, as outlined by the behavior of the error figures in Tab. 2, blurred data and/or noisy conditions affect more evidently the *Bare* implementation than the multi-resolution approach.

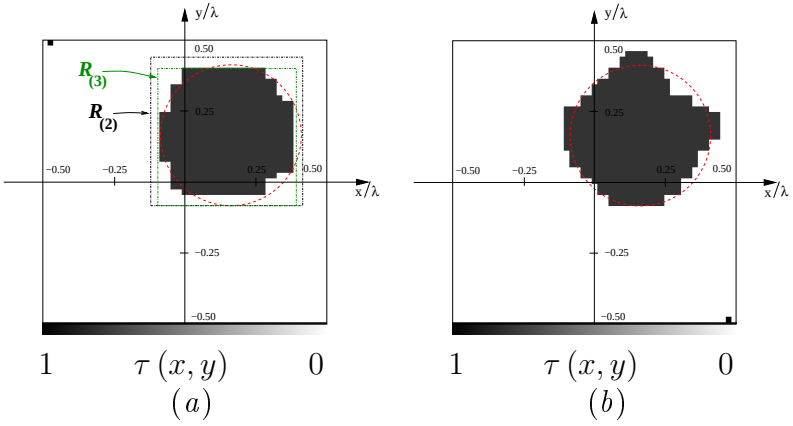

Figure 4.15: Circular cylinder ($\epsilon_C = 1.8$, $L_D = \lambda$, *Noisy Case*). Reconstructions with *IMSA-LS* (left column) and *Bare-LS* (right column) for $SNR = 10\,dB$.

In the second experiment, the same circular scatterer, but centered at $x^c = -y^c = 7\lambda/15$ within a larger investigation square of side $L_D = 2\lambda$ ($\rho_O = 2\lambda$), has been reconstructed. According to [15], $M(v) = 20$; $v = 1, ..., V$ receivers and $V = 20$ views are considered and D_I is discretized in $N_{IMSA} = 13 \times 13$ pixels. Figure 4.17(a) shows the reconstruction obtained at the convergence ($s_{opt} = 3$) by *IMSA-LS* when $SNR = 5\,dB$. The result reached by the *Bare-LS* ($N_{BARE} = 47 \times 47$) is reported in Fig. 4.17(b) as well. As it can be noticed, the multi-resolution inversion is characterized by a better estimation of the object center and shape as confirmed by the values of δ and Δ ($\delta\rfloor_{IMSA-LS} = 0.59$ vs. $\delta\rfloor_{Bare-LS} = 2.72$ and

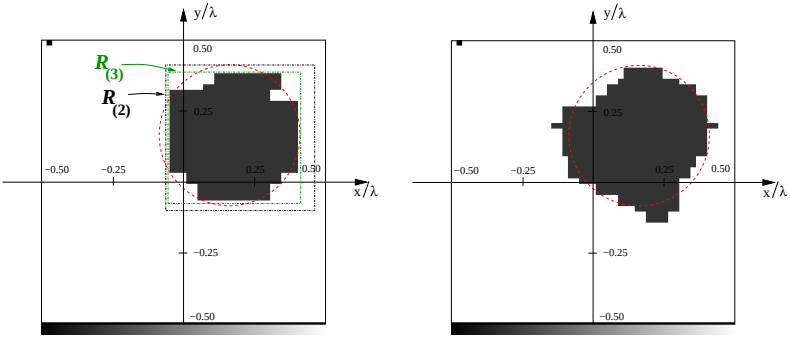

Figure 4.16: Numerical Data. Circular cylinder ($\epsilon_C = 1.8$, $L_D = \lambda$, *Noisy Case*). Reconstructions with *IMSA-LS* (left column) and *Bare-LS* (right column) for $SNR = 5\,dB$.

$\Delta\rfloor_{IMSA-LS} = 0.48$ vs. $\Delta\rfloor_{Bare-LS} = 0.64$). As for the computational load, the same conclusions from previous experiments hold true.

As far as the behavior of the level set in this second experiment is concerned, Figure 4.18 shows that the function $\phi_{k_{s=1}}$ at the iteration $k = 2$ presents some irregularities. The level set is characterized in the centre of the investigation domain by several spikes due to the update procedure at the previous iteration [Fig. 4.18(a)]. Unfortunately, these peaks compromise the computation of the update term at $k = 3$, although the behavior of the velocity function is regular [Fig. 4.18(b)]. As a matter of fact, the level set at $k = 3$ appears to be even

	$IMSA-LS$	$Bare-LS$
	$SNR = 20\,dB$	
δ	5.91×10^{-1}	2.72
Δ	0.98	1.28
	$SNR = 10\,dB$	
δ	2.28	2.45
Δ	1.07	1.80
	$SNR = 5\,dB$	
δ	6.78×10^{-1}	1.63
Δ	1.50	2.07

Table 4.2: Numerical Data. Circular cylinder ($\epsilon_C = 1.8$, *Noisy Case*). Values of the error indexes for different values of SNR.

more irregular than at iteration $k = 2$.

4.2.4 Rectangular Scatterer

The second test case deals with a more complex scattering configuration. A rectangular scatterer ($L = 0.27\lambda$ and $W = 0.13\lambda$) characterized by a dielectric permittivity $\epsilon_C = 1.8$ is centered at $x^c = -\frac{2}{3}\lambda$, $y^c = \lambda$ within an investigation domain of $L_D = 3\lambda$ as indicated by the red dashed line in Fig. 4.19. In such a case, the imaging setup is made up of $V = 30$ sources and $M = 30$ measurement points for each view v [15]. D_I is partitioned into $N_{IMSA} = 19 \times 19$ sub-domains (while $N_{Bare} = 33 \times 33$) and Δt_1 is set to 0.06.

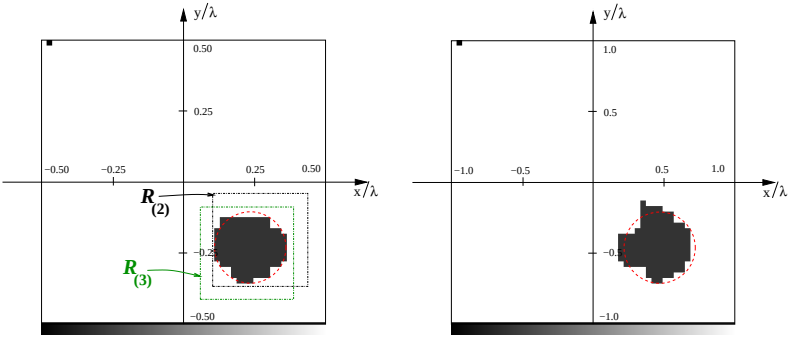

Figure 4.17: Numerical Data. Circular cylinder ($\epsilon_C = 1.8$, $L_D = 2\lambda$, *Noisy Case*). Reconstructions with *IMSA-LS* (a) and *Bare-LS* (b) when $SNR = 5\,dB$.

Before discussing the reconstruction capabilities, let us show a result concerned with the behavior of the proposed approach when varying the user-defined thresholds (γ_Θ, γ_τ, $\gamma_{\widetilde{x}^c}$, $\gamma_{\widetilde{y}^c}$, $\gamma_{\widetilde{L}}$) of the stopping criteria. Figure 4.19 displays the reconstructions achieved by using the sets of parameters given in Tab. 4.3 [Γ_1 - Fig. 4.19(a); Γ_2 - Fig. 4.19(b); Γ_3 - Fig. 4.19(c); Γ_4 - Fig. 4.19(d)] while the behaviors of the cost function are depicted in Fig. 4.20. As it can be noticed, the total number of iterations k_{tot} increases as the values of the thresholds γ_Θ and γ_τ decrease. However, in spite of a larger k_{tot}, using lower threshold values does not provide better results, as shown by the comparison between settings Γ_2 and Γ_4 [Figs. 4.19(b)-(d), and

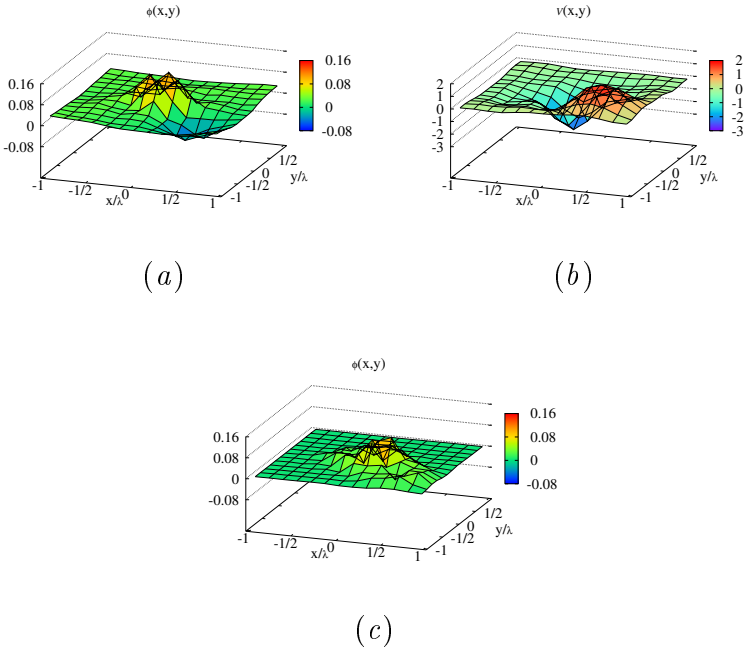

Figure 4.18: Numerical Data. Circular cylinder ($\epsilon_C = 1.8$, $L_D = 2\lambda$, $SNR = 5\,dB$). Behavior of the level set ϕ_{k_s} and the velocity $\mathcal{V}_{k_s}$. (a) ϕ_{k_s} at $k = 2$, (b) $\mathcal{V}_{k_s}$ at $k = 2$, and (c) ϕ_{k_s} at $k = 3$.

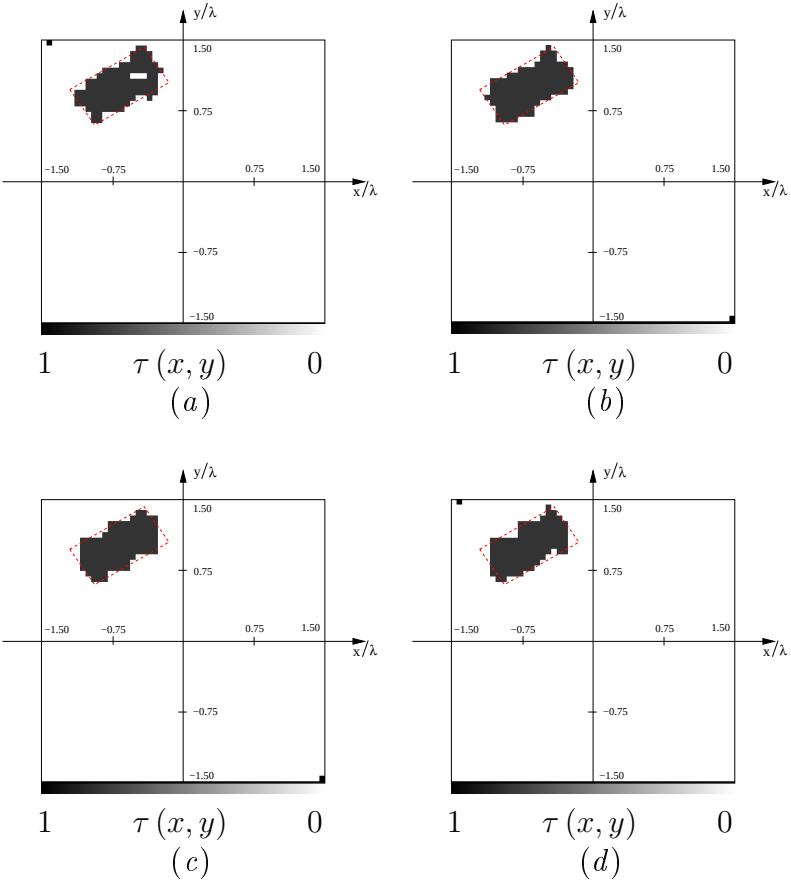

Figure 4.19: Numerical Data. Rectangular cylinder ($\epsilon_C = 1.8$, $L_D = 3\lambda$, *Noiseless Case*). Reconstructions with *IMSA-LS* for the different settings of Tab. 4.3 [(a) Γ_1, (b) Γ_2, (c) Γ_3, (d) Γ_4].

Set of Parameters	γ_Θ	γ_τ	$\gamma_{\widetilde{x}^c}$, $\gamma_{\widetilde{y}^c}$	$\gamma_{\widetilde{L}}$
Γ_1	0.5	0.05	0.01	0.05
Γ_2	0.2	0.02	0.01	0.05
Γ_3	0.2	0.02	0.1	0.5
Γ_4	0.02	0.002	0.01	0.05

Table 4.3: Numerical Data. Rectangular cylinder ($\epsilon_C = 1.8$, $L_D = 3\lambda$, *Noiseless Case*). Different settings for the parameters of the stopping criteria.

Fig. 4.20]. The sets of parameters characterized by $\gamma_\Theta = 0.2$ and $\gamma_\tau = 0.02$ provide a good trade-off between the arising computational burden and the quality of the reconstructions. As far as the stopping criterion of the multi-resolution procedure is concerned, figure 9 also shows two different behaviors of the cost function when using Γ_2 and Γ_3 (letting $\gamma_\Theta = 0.2$ and $\gamma_\tau = 0.02$). In particular, the proposed approach stops at $s_{opt} = 3$, instead of $s_{opt} = 4$, when increasing by a degree of magnitude the values of $\gamma_{\widetilde{x}^c}$, $\gamma_{\widetilde{y}^c}$, and $\gamma_{\widetilde{L}}$. Although with a heavier computational burden, the choice $\gamma_{\widetilde{x}^c} = \gamma_{\widetilde{y}^c} = 0.01$ and $\gamma_{\widetilde{L}} = 0.05$ appears to be more effective [see Fig. 4.19(b) vs. Fig. 4.19(c)].

Figures 4.21-4.24 and Table 4.4 show the results from the comparative study carried out in correspondence with different values of signal-to-noise ratio [$SNR = 20\,dB$ - Fig. 4.21(a) vs. Fig. 4.21(b); $SNR = 10\,dB$ - Fig. 4.22(a) vs. Fig. 4.22(b); $SNR = 5\,dB$ - Fig. 4.23(a) vs. Fig. 4.23(b)]. They fur-

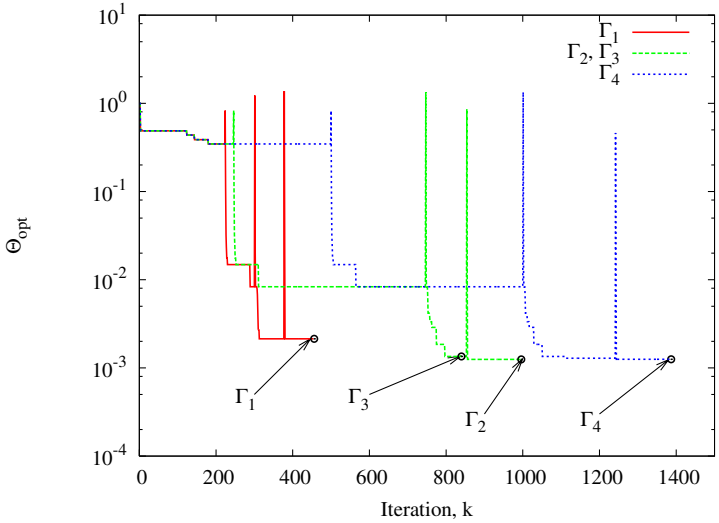

Figure 4.20: Numerical Data. Rectangular cylinder ($\epsilon_C = 1.8$, $L_D = 3\lambda$, *Noiseless Case*). Behavior of the cost function of *IMSA-LS* for the different settings of Tab. 4.3.

	$IMSA-LS$	$Bare-LS$
	$SNR = 20\,dB$	
k_{tot}	1089	41
N	361	1089
f_{pos}	1.02×10^{11}	1.02×10^{11}
	$SNR = 10\,dB$	
k_{tot}	393	53
N	361	1089
f_{pos}	3.70×10^{10}	1.37×10^{11}
	$SNR = 5\,dB$	
k_{tot}	410	28
N	361	1089
f_{pos}	3.86×10^{10}	7.23×10^{10}

Table 4.4: Numerical Data. Rectangular cylinder ($\epsilon_C = 1.8$, $L_D = 3\lambda$, *Noisy Case*). Computational indexes for different values of SNR.

ther confirm the reliability and efficiency of the multi-resolution strategy in terms of qualitative reconstruction errors (Fig. 4.24), especially when the noise level grows. In particular, the *Bare* implementation does not yield either the position or the shape of the rectangular scatterer when $SNR = 5\,dB$, whereas the *IMSA-LS* properly retrieves both the barycenter and the contour of the target. As for the computational cost, it should be noticed that although the *IMSA-LS* requires a greater number of iterations for reaching the convergence (Figs. 4.21-4.23(c), and Tab. 4.4), the total amount of complex floating-point operations, $f_{pos} = \mathcal{O}\left(2 \times \eta^3\right) \times k_{tot}$, usually results smaller (Tab. 4.4).

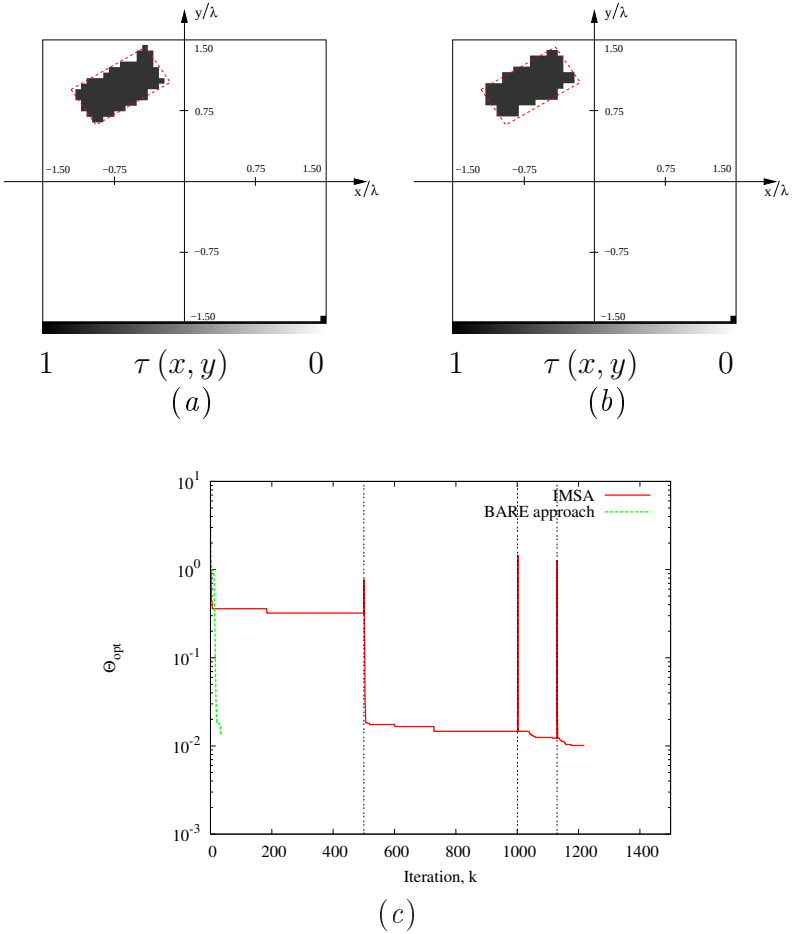

Figure 4.21: Numerical Data. Rectangular cylinder ($\epsilon_C = 1.8$, $L_D = 3\lambda$, *Noisy Case*). Reconstructions with *IMSA-LS* (a) and *Bare-LS* (b) for $SNR = 20\,dB$. (c) Behavior of the cost function versus the iteration index.

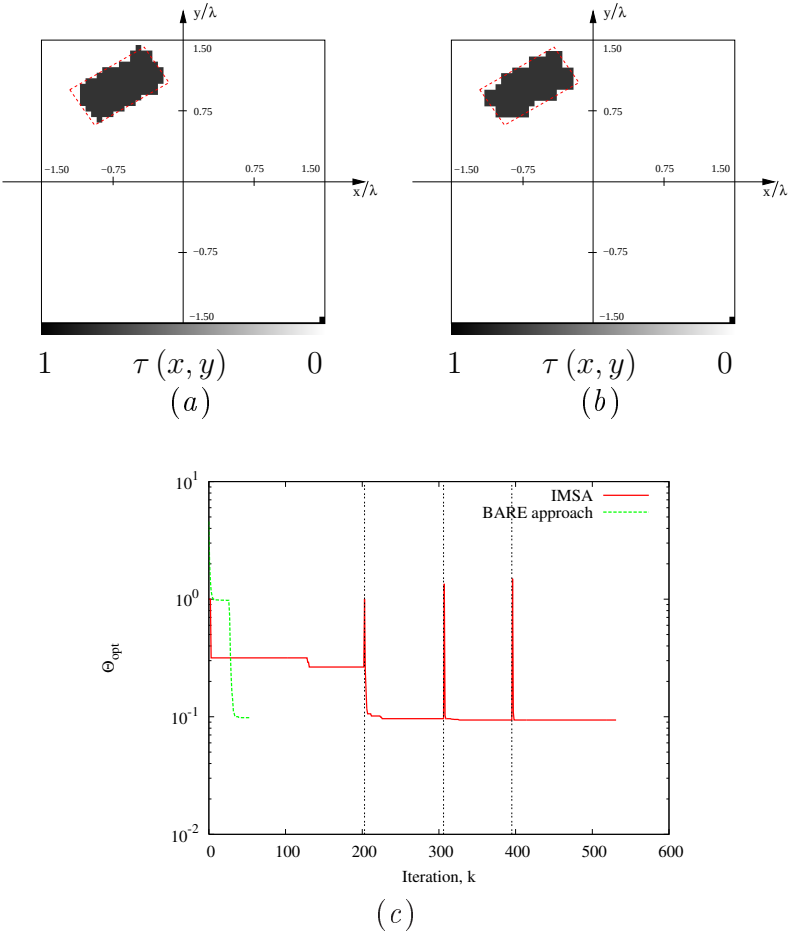

Figure 4.22: Numerical Data. Rectangular cylinder ($\epsilon_C = 1.8$, $L_D = 3\lambda$, *Noisy Case*). Reconstructions with *IMSA-LS* (a) and *Bare-LS* (b) for $SNR = 10\,dB$. (c) Behavior of the cost function versus the iteration index.

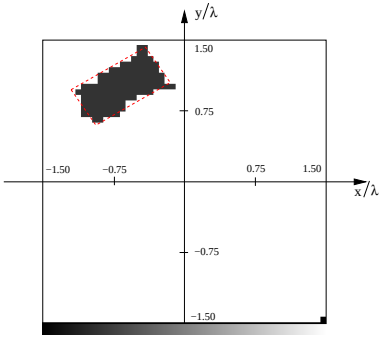

1 $\tau(x,y)$ 0

(a)

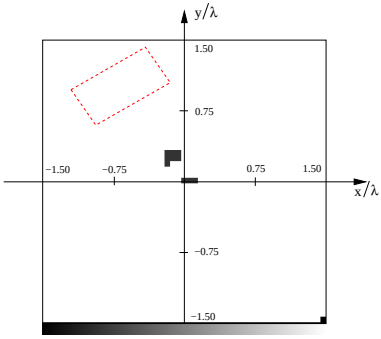

1 $\tau(x,y)$ 0

(b)

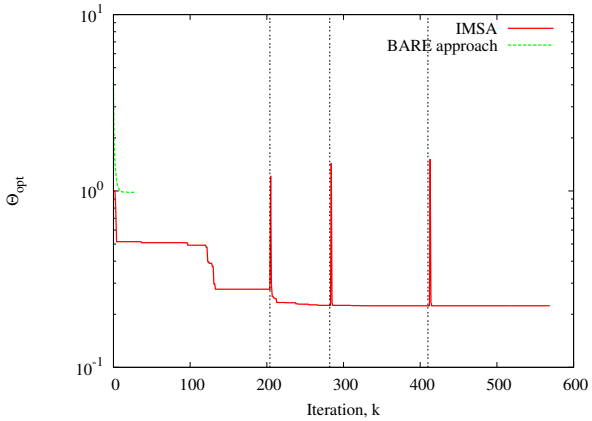

(c)

Figure 4.23: Numerical Data. Rectangular cylinder ($\epsilon_C = 1.8$, $L_D = 3\lambda$, *Noisy Case*). Reconstructions with *IMSA-LS* (a) and *Bare-LS* (b) for $SNR = 5\,dB$. (c) Behavior of the cost function versus the iteration index.

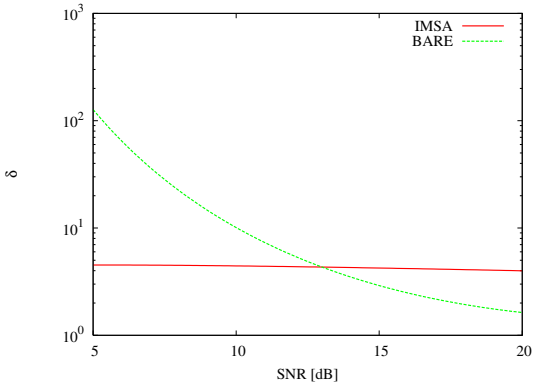

(a)

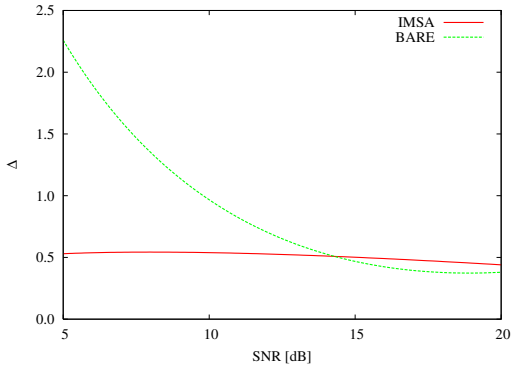

(b)

Figure 4.24: Numerical Data. Rectangular cylinder ($\epsilon_C = 1.8$, $L_D = 3\lambda$, *Noisy Case*). Values of the error figures versus SNR.

4.2.5 Hollow Cylinder

The third test case is concerned with the inversion of the data scattered by a higher-permittivity ($\epsilon_C = 2.5$) cylindrical ring centered at $x^c = y^c = \frac{3}{4}\lambda$, letting $L_D = 3\lambda$. The outer radius of the ring is $\rho_{ext} = \frac{2}{3}\lambda$, and the inner one is $\rho_{int} = \frac{\lambda}{3}$. By assuming the same arrangement of emitters and receivers as in Section 4.2.4, the investigation domain is discretized with $N_{IMSA} = 19{\times}19$ and $N_{Bare} = 35{\times}35$ square cells for the *IMSA-LS* and the *Bare-LS*, respectively. Moreover, Δt_1 is initialized to 0.003.

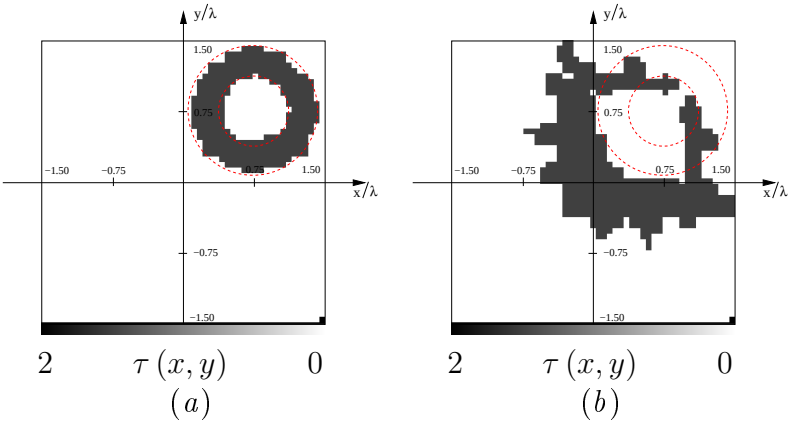

Figure 4.25: Numerical Data. Hollow cylinder ($\epsilon_C = 2.5$, $L_D = 3\lambda$, *Noisy Case*). Reconstructions with *IMSA-LS* (left column) and *Bare-LS* (right column) for $SNR = 20\,dB$.

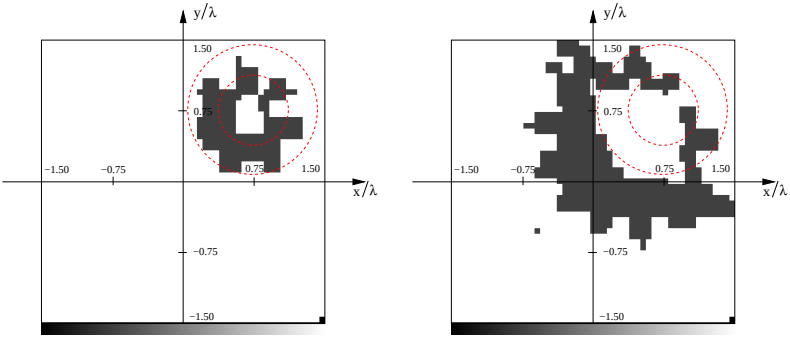

Figure 4.26: Numerical Data. Hollow cylinder ($\epsilon_C = 2.5$, $L_D = 3\lambda$, *Noisy Case*). Reconstructions with *IMSA-LS* (left column) and *Bare-LS* (right column) for $SNR = 10\,dB$.

As it can be observed from Figs. 4.25-4.26, where the profiles when $SNR = 20\,dB$ [Figs. $4.25(a)(b)$] and $SNR = 10\,dB$ [Figs. $4.26(a)(b)$] reconstructed by means of the *IMSA-LS* [Figs. 4.25-4.26(a)] and the *Bare-LS* [Figs. 4.25-4.26(b)] are shown, the integrated strategy overcomes the standard one both in locating the object and in estimating the shape. In particular, when $SNR = 20\,dB$, the distribution in Fig. $4.25(a)$ is a faithful estimate of the scatterer under test ($\delta\rfloor_{IMSA-LS} = 1.25$ and $\Delta\rfloor_{IMSA-LS} = 3.13$). On the contrary, the reconstruction with the *Bare-LS* is very poor ($\delta\rfloor_{Bare-LS} = 65.2$ and $\Delta\rfloor_{Bare-LS} = 34.39$). Certainly, a smaller SNR value impairs the inversion as shown in Fig. $4.26(a)$ [compared

to Fig. 4.25(a)]. However, in this case, the *IMSA-LS* is still able to properly locate the object ($\delta\rfloor_{IMSA-LS} = 1.7$ vs. $\delta\rfloor_{Bare-LS} = 65.9$) giving rough but useful indications about its shape ($\Delta\rfloor_{IMSA-LS} = 7.6$ vs. $\Delta\rfloor_{Bare-LS} = 34.55$).

4.3 Numerical Validation by means of Laboratory-Controlled Data

In order to further assess the effectiveness of the *IMSA-LS* also in dealing with experimental data, the multiple-frequency angular-diversity bi-static benchmark provided by *Institut Fresnel* in Marseille (France) has been considered. With reference to the experimental setup described in [100], the dataset "*dielTM_dec8f.exp*" has been processed. The field samples [$M(v) = 49$, $V = 36$] are related to an off-centered homogeneous circular cylinder $\rho = 15\,\text{mm}$ in diameter, characterized by a nominal value of the object function equal to $\tau(\underline{r}) = 2.0 \pm 0.3$, and located at $x_c = 0.0$, $y_c = -30\,\text{mm}$ within an investigation domain assumed in the following of square geometry and extension $30 \times 30\,\text{cm}^2$.

By setting $\epsilon_C = 3.0$, the reconstructions achieved are shown in Figs. 4.27-4.28 (*left column*) compared to those from the standard *LS* (*right column*) at $F = 4$ different operation frequencies. Whatever the frequency, the unknown scatterer is accurately localized and both algorithms yield, at convergence, structures that occupy a large subset of the true object. Such a similarity of performances, usually verified in synthetic ex-

	$f = 1\,GHz$		$f = 2\,GHz$	
	$IMSA-LS$	$Bare-LS$	$IMSA-LS$	$Bare-LS$
k_{tot}	506	69	532	200
f_{pos}	4.88×10^9	1.22×10^{11}	5.14×10^9	3.55×10^{11}

	$f = 3\,GHz$		$f = 4\,GHz$	
	$IMSA-LS$	$Bare-LS$	$IMSA-LS$	$Bare-LS$
k_{tot}	678	198	621	200
f_{pos}	6.55×10^9	3.51×10^{11}	5.99×10^9	3.55×10^{11}

Table 4.5: Experimental Data (Dataset "Marseille" [100]). Circular cylinder ("*dielTM_ dec8f.exp*"). Computational indexes.

periments when the value of SNR is greater than $20\,dB$, seems to confirm the hypothesis of a low-noise environment as it was already evidenced in [101].

Finally, also in dealing with experimental datasets, the *IMSA-LS* proves its efficiency since the overall amount of complex floating point operations still remains two orders in magnitude lower than the one of the *Bare-LS* (Tab. 5 - Figs. 4.30-4.29).

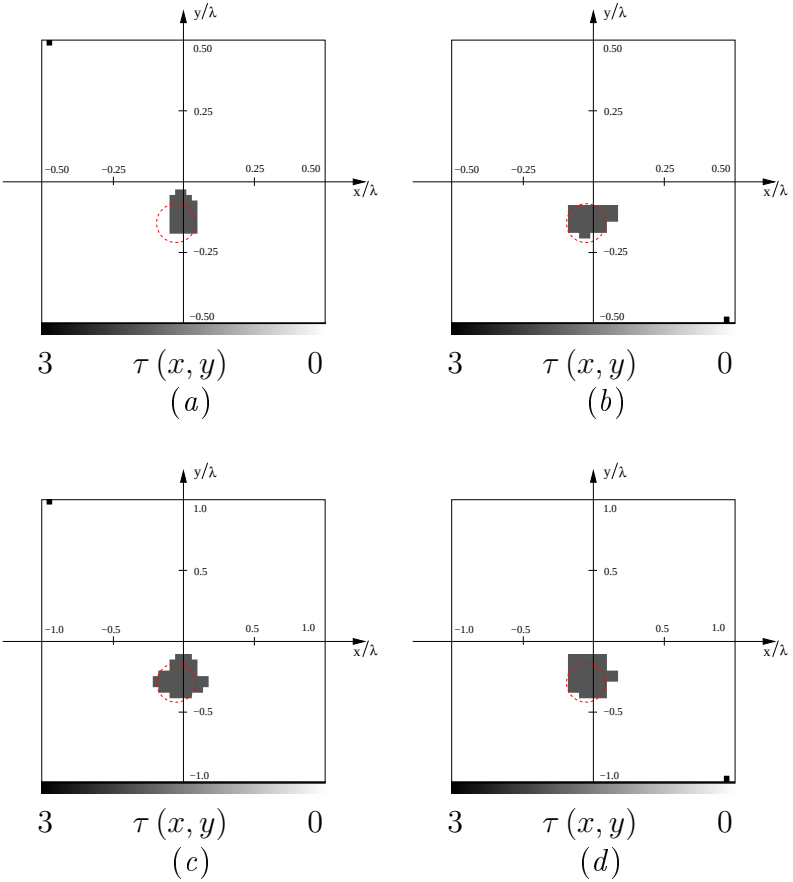

Figure 4.27: Experimental Data (Dataset "Marseille" [100]). Circular cylinder ("*dielTM_ dec8f.exp*"). Reconstructions with *IMSA-LS* (left column) and *Bare-LS* (right column) at different frequencies f [$f = 1\,GHz$ $(a)(b)$; $f = 2\,GHz$ $(c)(d)$].

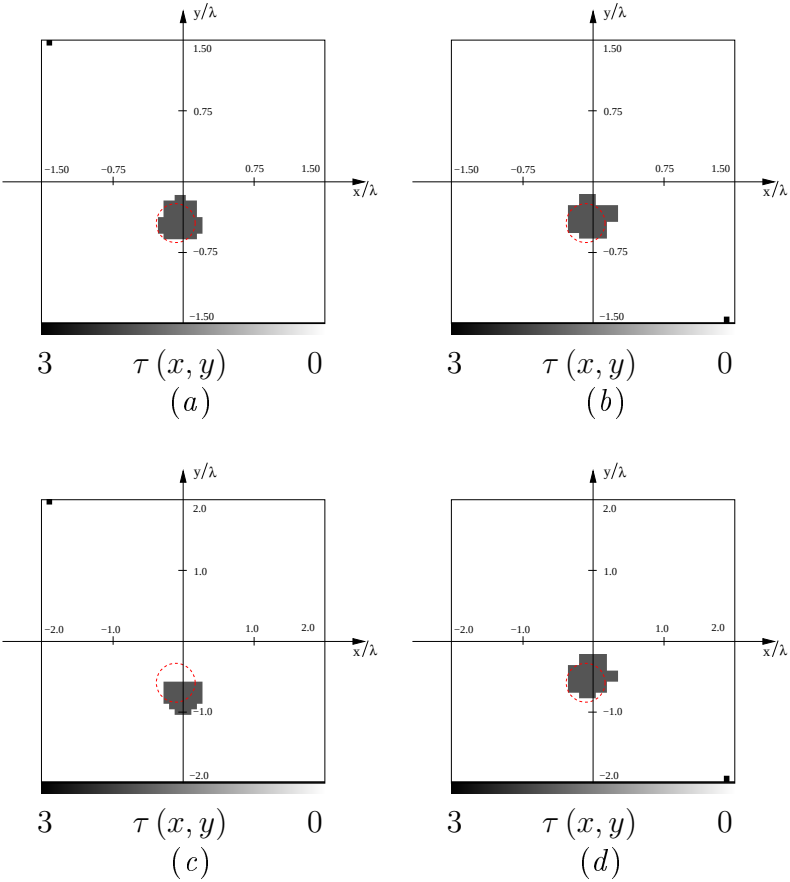

Figure 4.28: Experimental Data (Dataset "Marseille" [100]). Circular cylinder ("*dielTM_ dec8f.exp*"). Reconstructions with *IMSA-LS* (left column) and *Bare-LS* (right column) at different frequencies f [$f = 3\,GHz$ $(a)(b)$; $f = 4\,GHz$ $(c)(d)$].

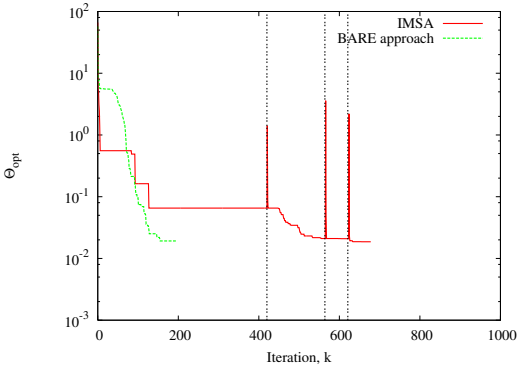

(a)

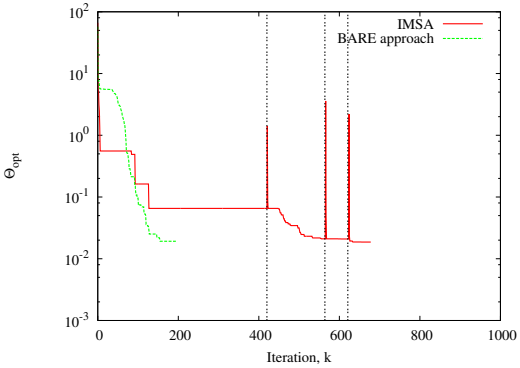

(b)

Figure 4.29: Experimental Data (Dataset "Marseille" [100]). Circular cylinder ("*dielTM_ dec8f.exp*"). Behavior of the cost function versus the number of iterations when (a) $f = 3\,GHz$, and (b) $f = 4\,GHz$.

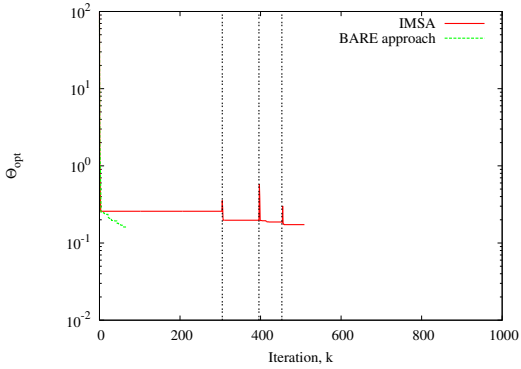

(a)

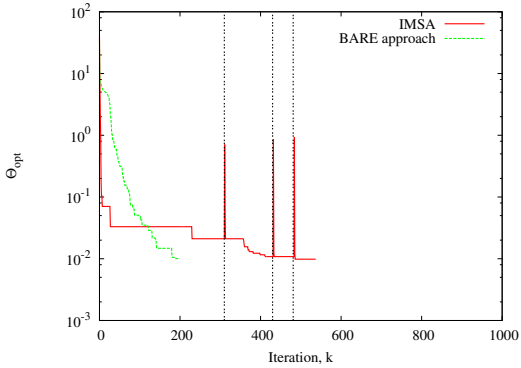

(b)

Figure 4.30: Experimental Data (Dataset "Marseille" [100]). Circular cylinder ("*dielTM_dec8f.exp*"). Behavior of the cost function versus the number of iterations when (a) $f = 1\,GHz$, and (b) $f = 2\,GHz$.

Chapter 5

The Multi-Region Approach

This chapter deals with the iterative multi-region multi-scaling approach with level-set-based minimization, customized for geometries characterized by multiple objects. After presenting the mathematical formulation by focusing onto the main differences with respect to the single-region version, the effectiveness of the approach is evaluated by means of the discussion of a selected set of results, when dealing both with numerical data and with laboratory-controlled data.

5.1 Mathematical Formulation

This section is aimed at presenting the multi-scaling multi-region approach (*IMSMRA*) integrated with level-set-based optimization (*LS*). Let us consider a set of P homogeneous obstacles with relative permittivity ϵ_C and conductivity σ_C that occupy the regions Υ_p, $p = 1, ..., P$, belonging to an investigation domain D_I. As in the previous chapter, such a scenario is probed by a set of V transverse-magnetic (TM) plane waves, with electric field $\underline{\zeta}^v(\underline{r}) = \zeta^v(\underline{r})\hat{\underline{z}}$ ($v = 1, \ldots, V$), $\underline{r} = (x, y)$. The scattered field, $\underline{\xi}^v(\underline{r}) = \xi^v(\underline{r})\hat{\underline{z}}$, is collected at $M(v)$, $v = 1, ..., V$, measurement points distributed in a region, called observation domain D_O, external to the investigation domain.

In order to retrieve the unknown position and shape of the target Υ_p, $p = 1, ..., P$, a multi-step procedure aimed at suitably increasing the spatial resolution only in a set of regions of interest (*RoI*s) containing the scatterers is considered [80][81]. With respect to the *IMSA-LS* discussed in Sect. 4.1, the strategy presented herein is able to deal with a set of $q = 1, ..., Q_{max}$ regions to better allocate the unknowns when the scenario is characterized by several objects distanced from one another. With reference to Fig. 5.1, at the first step ($s = 1$, s being the step index) an initial guess shape $\Upsilon_{s=1}$ belonging to D_I is chosen. Since no a-priori information on the scenario under test is assumed, the region of interest $R_s^{(q_s)}$, $q_s = 1, ..., Q_s$, at $s = 1$ (i.e., $R_{s=1}^{(q_s)} = D_I$, $Q_{s=1} = 1$) is partitioned into N_{MR} equal square sub-domains, N_{MR} being the number of degrees of freedom of the problem at hand [14]. The initialization of the level set function $\phi_s^{(q_s)}$, with $s = 1$ and $q_s = 1$, is carried

out by means of the oriented distance function (4.1) as in Sect. 4.1. Then, at each step s of the process ($s = 1, ..., S_{max}$), the following optimization procedure is repeated:

- ***Problem Unknown Representation*** - The problem unknown is represented at the k_s-th iteration, $k_s = 1, ..., k_s^{opt}$, as follows

$$\widetilde{\tau}_{k_s}\left(\underline{r}\right)\big|_{q_s} = \sum_{i=1}^{s}\sum_{q_i=1}^{Q_i}\sum_{n(q_i)=1}^{N(q_i)\rfloor_{MR}} \tau_{k_i}\big|_{q_i}\,\mathcal{B}\left(\underline{r}_{n(q_i)}\right) \quad \underline{r} \in D_I \tag{5.1}$$

where $N(q_i)\rfloor_{MR}$ is the number of sub-domains used to discretize $R_i^{(q_i)}$ and $\mathcal{B}\left(\underline{r}_{n(q_i)}\right)$ is a rectangular basis function whose support is the n-th sub-domain of the q_i-th region of interest at the i-th resolution level. Moreover, the coefficient $\tau_{k_i}^{(q_i)}$ is given by

$$\tau_{k_i}\big|_{q_i} = \begin{cases} \tau_C & \text{if } \Psi_{k_i}\left(\underline{r}_{n(q_i)}\right) \leq 0 \\ 0 & \text{otherwise} \end{cases} \tag{5.2}$$

letting

$$\Psi_{k_i}\left(\underline{r}_{n(q_i)}\right) = \begin{cases} \phi_{k_i}\left(\underline{r}_{n(q_i)}\right) & \text{if } i = s \\ \phi_{k_i^{opt}}\left(\underline{r}_{n(q_i)}\right) & \text{if } i < s \text{ and } \underline{r}_{n(q_i)} \in R_i^{(q_i)} \end{cases} . \tag{5.3}$$

- ***Field Distribution Updating*** - After updating the problem unknown $\tau_{k_i}^{(q_i)}$, the value of the electric field $E_{k_s}^v\left(\underline{r}\right)$ in the $n(q_i)$-th sub-domains of the q_i-th region of interest is

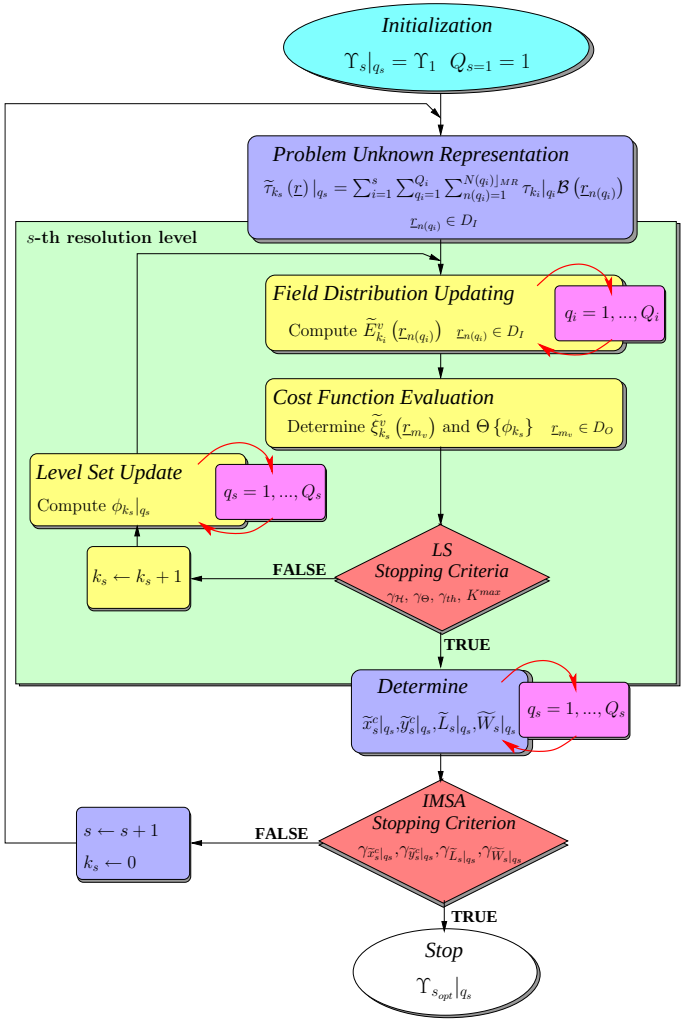

Figure 5.1: Block diagram description of the *IMSMRA-LS* zooming procedure.

computed by means of a customized numerical technique based on the point-matching version of the Method of Moments (MoM) [39] according to the following relationship

$$\widetilde{E}_{k_i}^{v}\left(\underline{r}_{n(q_i)}\right) = \\ = \sum_{q_i=1}^{Q_i}\sum_{n(q_i)=1}^{N(q_i)\rfloor_{MR}}\zeta^{v}\left(\underline{r}_{p_i}\right)\times \\ \times\left[1-\widetilde{\tau}_{k_i}\left(\underline{r}_{p(q_i)}\right)G_{2D}\left(\underline{r}_{n(q_i)}/\underline{r}_{p(q_i)}\right)\right]^{-1}, \\ \underline{r}_{n(q_i)},\underline{r}_{p(q_i)}\in D_I \\ n(q_i)=1,...,N(q_i)\rfloor_{MR}\ . \tag{5.4}$$

- ***Cost Function Evaluation*** - The reconstructed scattered field $\widetilde{\xi}_{k_s}^{v}\left(\underline{r}_{m(v)}\right)$ at the $m(v)$-th measurement point, $m(v)=1,...,M(v)$, is updated by the following relationship

$$\widetilde{\xi}_{k_s}^{v}\left(\underline{r}_{m(v)}\right)=\sum_{i=1}^{s}\sum_{q_i=1}^{Q_i}\sum_{n(q_i)=1}^{N(q_i)\rfloor_{MR}}\widetilde{\tau}_{k_i}\left(\underline{r}_{n(q_i)}\right)\times \\ \times\widetilde{E}_{k_i}^{v}\left(\underline{r}_{n(q_i)}\right)G_{2D}\left(\underline{r}_{m(v)}/\underline{r}_{n(q_i)}\right) \tag{5.5}$$

  where the total electric field distribution $\widetilde{E}_{k_i}^{v}\left(\underline{r}_{n(q_i)}\right)$ is given by (5.4). Then, the cost function is evaluated at the iteration k_s by considering the relationship (4.7).

- ***Minimization Stopping*** - The iterative process stops (i.e., $k_s^{opt}=k_s$ and $\widetilde{\tau}_s^{opt}=\widetilde{\tau}_{k_s}$) when a set of conditions concerned with the stability of the reconstruction becomes true or when the maximum number of iterations is

reached ($k_s = K_{max}$) or when the value of the cost function is smaller than a fixed threshold γ_{th}. As far as the stability of the reconstructions is concerned, the following double criterion is considered:

– The first condition is aimed at assessing if the shape of the trial solution does not change during the iterative process. In order to overcome the limitations characterizing the standard criterion (4.8) when the iterative solution is characterized by a "blinking" behavior[1], a new strategy based on the Hausdorff distance $\mathcal{L}$ [102]-[105] is adopted. More in detail, such a criterion is satisfied when in the region of interest $R_s^{(q_s)}$, $q_s = 1, ..., Q_s$, for a fixed number of iterations, $K_{\mathcal{L}}$, the value of the Hausdorff distance computed between the contour of the $(k_s - j)$-th trial solution, $j = 1, ..., K_{\mathcal{L}}$, and the contour of the current trial solution is smaller than a user defined threshold $\gamma_{\mathcal{L}}$. Accordingly, the following relationship is evaluated

$$\max_{j=1,...,K_{\mathcal{L}}} \frac{\mathcal{L}\left\{\partial\left(\widetilde{\tau}_{k_s}|_{q_s}\right), \partial\left(\widetilde{\tau}_{k_s-j}|_{q_s}\right)\right\}}{l_s|_{q_s}} < \gamma_{\mathcal{L}} \tag{5.6}$$

where the operator $\partial(\cdot)$ (Sect. B.1) performs the edge detection, providing the $B_{k_s}|_{q_s}$ contour sub-

[1] The iterative solution is characterized by a "blinking" behavior when a small amount of pixels of the reconstruction turns up intermittently (i.e., the level set emerges intermittently), without significantly modifying the estimated shapes.

domains of the reconstructed shapes, and $l_s|_{q_s}$ is the average value of the cell-sides in the region q_s at the step s, computed as follows

$$l_s|_{q_s} = \frac{\Delta x_s|_{q_s} + \Delta y_s|_{q_s}}{2} \tag{5.7}$$

Δx_s and Δy_s being the cell-side along $\underline{\hat{x}}$ and $\overline{\hat{y}}$, respectively. For the sake of completeness, the Hausdorff distance $\mathcal{L}$ is defined as

$$\begin{aligned} \mathcal{L}\left\{\partial\left(\widetilde{\tau}_{k_s}|_{q_s}\right), \partial\left(\widetilde{\tau}_{k_s-j}|_{q_s}\right)\right\} = \\ = \max\left\{\max_{\underline{r}_{b(q_s)}}\min_{\underline{r}_{p(q_s)}} d_{k_s,q_s,j,b,p}\ , \right. \\ \left. \max_{\underline{r}_{p(q_s)}}\min_{\underline{r}_{b(q_s)}} d_{k_s,q_s,j,b,p}\right\} \\ b(q_s) = 1, ..., B_{k_s}|_{q_s} \\ p(q_s) = 1, ..., B_{k_s-j}|_{q_s} \end{aligned} \tag{5.8}$$

where

$$\begin{aligned} d_{k_s,q_s,j,b,p} = \left[\left(x^B_{k_s}\big|_{b(q_s)} - x^B_{k_s-j}\big|_{p(q_s)}\right)^2 + \right. \\ \left. + \left(y^B_{k_s}\big|_{b(q_s)} - y^B_{k_s-j}\big|_{p(q_s)}\right)^2\right]^{\frac{1}{2}}, \end{aligned} \tag{5.9}$$

$\left(x^B_{k_s}\big|_{b(q_s)},\ y^B_{k_s}\big|_{b(q_s)}\right)$ and $\left(x^B_{k_s-j}\big|_{p(q_s)},\ y^B_{k_s-j}\big|_{p(q_s)}\right)$ being the coordinates of the $B_{k_s}|_{q_s}$ contour sub-domains detected by $\partial(\cdot)$.

  - The second criterion, about the stability of the reconstruction, is satisfied when the cost function becomes stationary within a window of K_Θ iterations as in (4.9).

- ***Iteration Update*** - The iteration index is updated ($k_s \rightarrow k_s + 1$).

- ***Level Set Update*** - As for *IMSA-LS*, the level set in the region q_s at the step s is updated by solving the following Hamilton-Jacobi equation

$$\begin{aligned}\phi_{k_s}\left(\underline{r}_{n(q_s)}\right) = \phi_{k_s-1}\left(\underline{r}_{n(q_s)}\right) - \\ - \Delta t_s|_{q_s}\, \mathcal{V}_{k_s-1}\left(\underline{r}_{n(q_s)}\right) \mathcal{H}\left\{\phi_{k_s-1}\left(\underline{r}_{n(q_s)}\right)\right\}\end{aligned} \tag{5.10}$$

where $\mathcal{H}\{\cdot\}$ is the Hamiltonian operator given as

$$\begin{aligned}&\mathcal{H}^2\left\{\phi_{k_s}\left(\underline{r}_{n(q_s)}\right)\right\} = \\ &= \begin{cases} \max^2\left\{\mathcal{D}_{k_s}^{x-}\big|_{q_s}; 0\right\} + \min^2\left\{\mathcal{D}_{k_s}^{x+}\big|_{q_s}; 0\right\} + \\ \quad +\max^2\left\{\mathcal{D}_{k_s}^{y-}\big|_{q_s}; 0\right\} + \min^2\left\{\mathcal{D}_{k_s}^{y+}\big|_{q_s}; 0\right\} \\ \qquad \text{if } \mathcal{V}_{k_s}\left(\underline{r}_{n(q_s)}\right) \geq 0 \\ \\ \min^2\left\{\mathcal{D}_{k_s}^{x-}\big|_{q_s}; 0\right\} + \max^2\left\{\mathcal{D}_{k_s}^{x+}\big|_{q_s}; 0\right\} + \\ \quad +\min^2\left\{\mathcal{D}_{k_s}^{y-}\big|_{q_s}; 0\right\} + \max^2\left\{\mathcal{D}_{k_s}^{y+}\big|_{q_s}; 0\right\} \\ \qquad \text{otherwise} \end{cases}\end{aligned} \tag{5.11}$$

with

- $\mathcal{D}_{k_s}^{x\pm}\big|_{q_s} = \frac{\pm\phi_{k_s}\left(x_{n(q_s)\pm1},y_{n(q_s)}\right)\mp\phi_{k_s}\left(x_{n(q_s)},y_{n(q_s)}\right)}{\Delta x_s|_{q_s}}$,
- $\mathcal{D}_{k_s}^{y\pm}\big|_{q_s} = \frac{\pm\phi_{k_s}\left(x_{n(q_s)},y_{n(q_s)\pm1}\right)\mp\phi_{k_s}\left(x_{n(q_s)},y_{n(q_s)}\right)}{\Delta y_s|_{q_s}}$.

Furthermore, $\mathcal{V}_{k_s}\left(\underline{r}_{n(q_s)}\right)$ is the value of the velocity function in the $n(q_s)$-th sub-domains of the q_s-th region of interest at the step s and $\Delta t_{k_s}\big|_{q_s}$ is the time-step chosen by means of the Courant-Friedrich-Leroy constraint [29][30] as follows

$$\Delta t_{k_s}\big|_{q_s} = \frac{\min\left\{\Delta x_s|_{q_s}\,,\,\Delta y_s|_{q_s}\right\}}{\max_{n(q_s)}\mathcal{V}_{k_s}\left(\underline{r}_{n(q_s)}\right)}\,. \tag{5.12}$$

In order to get the velocity function in the q_s-th region of interest, the adjoint problem of (5.4) is solved and starting from the adjoint field $\mathcal{F}_{k_s}^{v}\big|_{q_s}$ the following relationship is evaluated

$$\mathcal{V}_{k_s}\left(\underline{r}_{n(q_s)}\right) = -\Re\left\{\frac{\sum_{v=1}^{V}\tau_C\widetilde{E}_{k_s}^{v}\left(\underline{r}_{n(q_s)}\right)\mathcal{F}_{k_s}^{v}\left(\underline{r}_{n(q_s)}\right)}{\sum_{v=1}^{V}\sum_{m(v)=1}^{M(v)}\left|\xi_{k_s}^{v}\left(\underline{r}_{m(v)}\right)\right|^2}\right\},$$
$$n(q_i) = 1,...,\,N(q_i)\rfloor_{MR}\,. \tag{5.13}$$

- ***Level Set Re-Initialization*** - Unfortunately, the result of the update procedure on the level set is not a distance function, and, in general, the level set representation is not unique [32][106]. To restore the ori-

ented distance function thus reducing numerical problems concerned with the computations of the finite differences $\mathcal{D}_{k_s}$, a functional approach is considered herein. In particular, if $\mathcal{H}\left\{\phi_{k_s}\left(\underline{r}_{n(q_s)}\right)\right\}$, which is an approximation of $\left|\nabla\phi_{k_s}\left(\underline{r}_{n(q_s)}\right)\right|$, is greater than a certain threshold γ_ϕ, $n(q_s) = 1, ..., N(q_i)$, then the level-set function is reinitialized as

$$\phi_{k_s}\left(\underline{r}_{n(q_s)}\right) = \begin{cases} -\min_{b=1,...,B_{q_s}}\left\{d_{n(q_s),b}\right\} \\ \qquad\qquad \text{if } \tau\left(\underline{r}_{n(q_s)}\right) = \tau_C \\ \min_{b=1,...,B_{q_s}}\left\{d_{n(q_s),b}\right\} \\ \qquad\qquad \text{if } \tau\left(\underline{r}_{n(q_s)}\right) = 0\,, \end{cases} \tag{5.14}$$

where $d_{n(q_s),b}$ is the distance between $\underline{r}_{n(q_s)}$ and $\underline{r}_b$, $\underline{r}_b$ being b-th border-cell ($b = 1, \ldots, B_{q_s}$) of the trial shape reconstructed in the region q_s, $q_s = 1, ..., Q_s$.

At the end of the s-th minimization process, the contrast function is updated $\left[\widetilde{\tau}_s^{opt}\big|_{q_s} = \widetilde{\tau}_{k_s}\big|_{q_s},\ \underline{r} \in D_I \text{ and } q_s = 1, ..., Q_s\right]$ by means of (5.1) and the new regions of interest $R_s^{(q_s)}$, $q_s = 1, ..., Q_s$, are defined. To do so, the following set of operations is repeated for all the regions determined at the step s (Fig. 5.2):

- ***Find the Number of Seeds*** - Since the reconstructions provided by the level-set-based strategies are binary, the first step of the "morphological" processing[2] is

[2] The term "morphological" refers to the study of the shapes of the reconstructed scatterers in order to get the most suitable regions of interest.

aimed at counting the number of targets which have been reconstructed. Such a procedure, called *erosion* [80], consists in creating a new "image" $\widetilde{\tau}_s^E\big|_{q_s}$ of the shapes reconstructed in the q_s-th region, $q_s = 1, ..., Q_s$, as follows

$$\widetilde{\tau}_s^E\left(x_{n(q_s)},\, y_{n(q_s)}\right) = \\ = \begin{cases} \tau_C & \text{if } \widetilde{\tau}_s^{opt}\left(x_{n(q_s)},\, y_{n(q_s)}\right) = \tau_C \text{ and} \\ & \sum_{p=-1}^{1}\sum_{j=-1}^{1} \widetilde{\tau}_s^{opt}\left(x_{n(q_s)-p},\, y_{n(q_s)-j}\right) < 9\cdot\tau_C \\ 0 & \text{otherwise}\,. \end{cases} \tag{5.15}$$

The q_s-th arising image contains at least one pixel for each object [Fig. 5.2(b)]. Unfortunately, these pixels, called *seeds*, bring no information about the actual number of targets (e.g., a hollow disc has two seeds, the first on the inner contour and the second on the outer contour).

- ***Count the Number of Objects*** - Since the seeds are necessarily located on the contours of the reconstructed shapes, the number of objects is counted by exploiting both the information provided by the previous step and the edge detection operator $\partial(\cdot)$. That is, the contour $\partial\left(\widetilde{\tau}_s^{opt}\big|_{q_s}\right)$ of the shapes reconstructed in the q_s-th region of interest at the step s is found [Fig. 5.2(c)] and the boundaries of the reconstructed scatterers[3] are detected by "walking" along the arising edges starting from

[3] The term "boundary" refers to a contour of one object (e.g., the hollow cylinder has two boundaries).

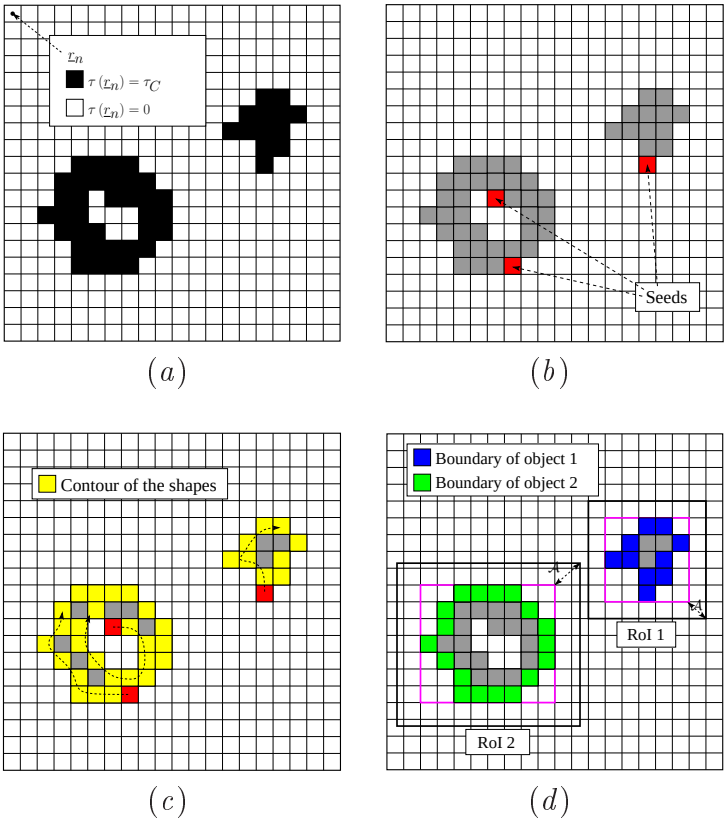

Figure 5.2: Graphical representation of the "morphological" processing: (a) profile reconstructed at step s ($Q_s = 1$), (b) detection of the *seeds* by means of the erosion procedure, (c) "walking" around the edges, and (d) detection of object's boundaries and of the regions of interest for the resolution level $s + 1$.

the seeds (more details about the algorithm are given in Sect. B.2). As a consequence, the actual number of objects is determined by counting the number of boundaries, neglecting those that are included within other contours [Fig. 5.2(d)].

- ***Define the Parameters of the Region of Interest*** - Q_{s+1} regions of interest are defined at the step $s+1$ by evaluating the maximum size of the boundaries detected in the previous step. In order to prevent the *RoI*s to be included in the objects or overlapping between adjacent regions, the coordinates of the center $\widetilde{x}^c_{s+1}\big|_{q_{s+1}}$, $\widetilde{y}^c_{s+1}\big|_{q_{s+1}}$ and the sides $\widetilde{L}_{s+1}\Big|_{q_{s+1}}$, $\widetilde{W}_{s+1}\Big|_{q_{s+1}}$ are computed by increasing the actual size of the regions by an allowance value $\mathcal{A}_{s+1}$, $s = 1, ..., S_{max} - 1$. Moreover, $\widetilde{L}_{s+1}\Big|_{q_{s+1}}$, $\widetilde{W}_{s+1}\Big|_{q_{s+1}}$ have to be chosen such that

$$\frac{\min\left(\widetilde{L}_{s+1}\Big|_{q_{s+1}}, \widetilde{W}_{s+1}\Big|_{q_{s+1}}\right)}{\max\left(\widetilde{L}_{s+1}\Big|_{q_{s+1}}, \widetilde{W}_{s+1}\Big|_{q_{s+1}}\right)} > \frac{3}{4} \tag{5.16}$$

in order to allow an accurate solution of the forward problem according to the point-matching version of the MoM [39], since the sides of the *RoI*s are discretized using the same number of sub-domains.

After the definition of the parameter of the *RoI*s, the step index

is increased ($s \leftarrow s+1$) and a convergence check of the multi-scaling procedure is performed. The reconstruction algorithm is stopped if both location and sides of the region of interest become stationary ($s_{opt} = s$) [19], i.e.,

$$\left\{ \frac{|\Omega_{s-1} - \Omega_s|}{|\Omega_{s-1}|} \times 100 \right\} < \gamma_\Omega, \quad \Omega = \widetilde{x}_s^c\big|_{q_s}, \widetilde{y}_s^c\big|_{q_s}, \widetilde{L}_s^c\Big|_{q_s}, \widetilde{W}_s^c\Big|_{q_s} \tag{5.17}$$

γ_Ω being a user defined threshold, or when a maximum number of steps ($s_{opt} = S_{max}$) is reached.

If the convergence check does not hold true, the total amount N_{MR} of available basis functions is split in the Q_s regions to keep the ratio between data and unknown constant, according to the following relationship

$$N(q_s)\rfloor_{MR} = \mathcal{L}\left\{ N_{MR} \frac{\widetilde{L}_s\big|_{q_s} \times \widetilde{W}_s\big|_{q_s}}{\sum_{p_s=1}^{Q_s} \widetilde{L}_s\big|_{p_s} \times \widetilde{W}_s\big|_{p_s}} \right\} \qquad q_s = 1, ..., Q_s \tag{5.18}$$

where the operator $\mathcal{L}$ returns the smaller integer part of its argument.

Finally, at the end of the multi-step process ($s = s_{opt}$), the problem solution is obtained as $\widetilde{\tau}^{opt}\left(\underline{r}_{n(q_i)}\right) = \widetilde{\tau}_s^{opt}\left(\underline{r}_{n(q_i)}\right)$, $n(q_i) = 1, ..., N(q_i)\rfloor_{MR}$, $q_i = 1, ..., Q_i$, $i = 1, ..., s_{opt}$.

5.2 Preliminary Validation

5.2.1 The IMSMRA-LS when dealing with Simple Geometries

In order to preliminary test the multi-region approach, this test case deals with the geometry considered in the second experiment of section 4.2.3, namely with the cylinder having radius $\lambda/4$ and centered at $x^c = -y^c = 7\lambda/15$ in an investigation square of side $L_D = 2\lambda$. The purpose of this section is twofold: on one hand, to assess the reconstruction capabilities of the multi-region approach when the geometry is characterized by a single object. On the other hand, to discuss the behavior of the multi-resolution level set during the iterative process, pointing out benefits and drawbacks of the update strategy adopted in the multi-region approach.

As for the initialization of the *IMSMRA-LS* technique, the initial guess is a circular scatterer of radius $\lambda/4$ centered in the investigation domain and sampled at the resolution level $s = 1$. The *RoI* is discretized in $N_{MR} = 13 \times 13$ sub-domains at each step of the iterative multi-region multi-resolution procedure, while the maximum number of *RoI* is set to $Q_{max} = 10$. The stopping criterion has been configured as follows: $\gamma_\phi = \sqrt{2}$ (maximum value for the numerical Hamiltonian), $S_{max} = 5$ (maximum number of steps), $\gamma^{\widetilde{x}^c} = \gamma^{\widetilde{y}^c} = 0.01$ and $\gamma^{\widetilde{L}} = 0.05$ (multi-step process thresholds), $K_{max} = 500$ (maximum num-

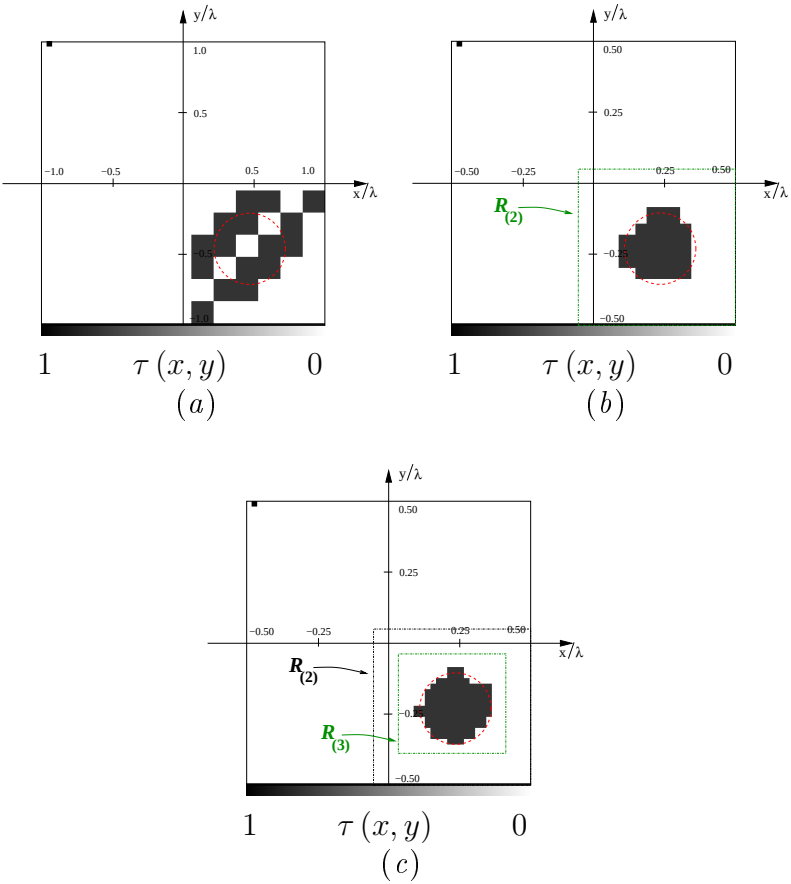

Figure 5.3: Numerical Data. Circular cylinder ($\epsilon_C = 1.8$, $L_D = 2\lambda$, *Noisy Case*). Reconstructions with *IMSMRA-LS* at (a) $s = 1$, (b) $s = 2$, and (c) $s = s_{opt} = 3$.

ber of optimization iterations), $\gamma_\Theta = 0.2$ and $\gamma_\mathcal{L} = 1.5$ (optimization thresholds), $K_\Theta = K_\mathcal{L} = 0.10\,K_{max}$ (stability counters), and $\gamma_{th} = 10^{-5}$ (threshold on the cost function). In addition, at the s-th step and in the q-th region the value $\Delta t_{k_s}|_{q_s}$ of the time-step, with $s = 1, ..., s_{opt}$ and $q_s = 1, ..., Q_{max}$, is chosen according to the CFL-based relationship, while the values of the allowance $\mathcal{A}_s$ for estimating the size of the regions of interest are set to $\mathcal{A}_{s=2} = 40\%$, $\mathcal{A}_{s=3} = 30\%$, and $\mathcal{A}_{s=4} = \mathcal{A}_{s=5} = 20\%$.

Figure 5.3 shows the reconstruction achieved when considering synthetic data blurred by noise characterized by $SNR = 5\,dB$. Because of the low SNR and of the coarse resolution level, the result obtained at the end of step $s = 1$ [Fig. 5.3(a)] appears to be inaccurate in terms of shape estimation, while the barycentre of the scatterer is quite accurately estimated. However, in spite of the inaccurate reconstruction at the first step, the behavior of the level set $\phi_{k_s}|_{q_s}$, $q_s = 1$, appears to be quite regular [Fig. 5.4(a)], especially if compared with the behavior of the level set at the first iterations of the second experiment of Sect. 4.2.3. Such a regular shape, even at the last iteration of the step, is mainly due to the re-initialization procedure described in Sect. 5.1 and to the CFL-based procedure for choosing $\Delta t_{k_s}|_{q_s}$.

Thanks to the increase of the spatial resolution achieved in the RoI at $s = 2$, the shape of the actual scatterer is better estimated [Fig. 5.3(b)]. Then, at the final step, $s = s_{opt} = 3$, the RoI is further focused on the area that contains the true object and the accuracy of the reconstruction is further improved [Fig. 5.3(c)]. Furthermore, Figs. 5.4(b) and (c) show

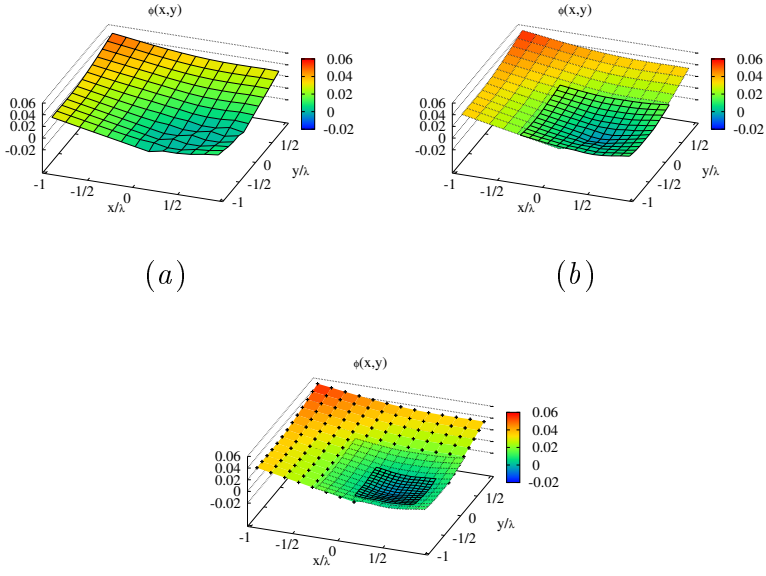

Figure 5.4: Numerical Data. Circular cylinder ($\epsilon_C = 1.8$, $L_D = 2\lambda$, *Noisy Case*). Behavior of the level set ϕ_{k_s} at the end of the step (a) $s = 1$, (b) $s = 2$, and (c) $s = s_{opt} = 3$.

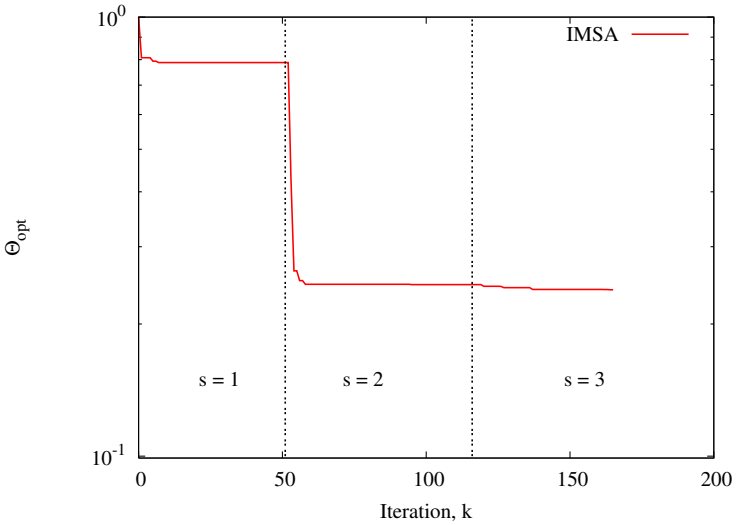

Figure 5.5: Numerical Data. Circular cylinder ($\epsilon_C = 1.8$, $L_D = 2\lambda$, $SNR = 5\,dB$). Behavior of the cost function when using *IMSMRA-LS*.

that the solving shape of ϕ^{opt}_{s,q_s}, when $s = 2$ and $s = s_{opt} = 3$ respectively, is quite symmetrical with respect to the center of the scatterer. As for the quality of the final reconstruction [Fig. 5.3(c)], the localization error is slightly higher than the one achieved in the reconstruction of Fig. 4.17(a) ($\delta\rfloor_{IMSMRA-LS} = 0.73$ vs. $\delta\rfloor_{IMSA-LS} = 0.59$), while the shape of the object is better retrieved ($\Delta\rfloor_{IMSMRA-LS} = 0.45$ vs. $\Delta\rfloor_{IMSA-LS} = 0.48$).

Finally, Figure 5.5 shows the behavior of the multi-resolution

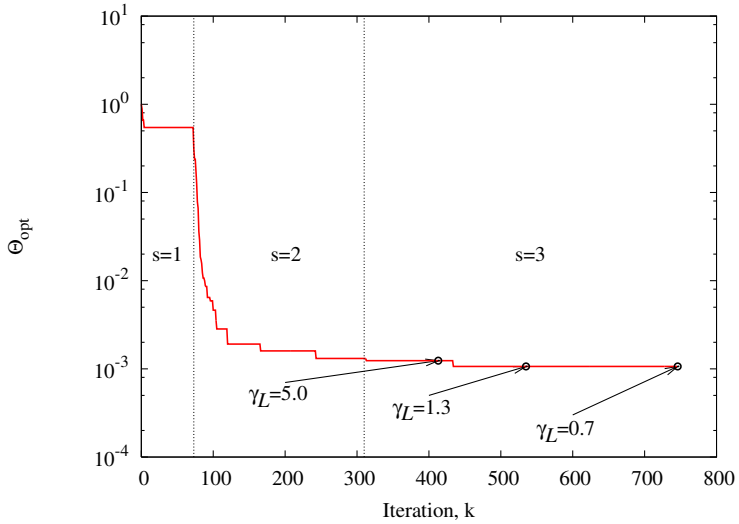

Figure 5.6: Numerical Data. Rectangular cylinder ($\epsilon_C = 1.8$, $L_D = 3\lambda$, *Noiseless Case*). Behavior of the cost function of *IMSMRA-LS* when varying $\gamma_{\mathcal{L}}$.

cost function Θ_{opt} when $Q = 1$. It is worth noting that the spikes between two adjacent steps characterizing *IMSA-LS*'s error curves have disappeared for *IMSMRA-LS*, since the field distribution is updated before the evaluation of $\Theta\left\{\Delta t_{k_s}|_{q_s}\right\}$, with $k_s = 1$. Furthermore, as the spatial resolution improves, the cost function is characterized by a "jump" whose amplitude is higher between $s = 1$ and $s = 2$ than between $s = 2$ and $s = s_{opt} = 3$.

5.2.2 Calibration of the Stopping Criterion

With reference to the mathematical formulation presented in Sect. 5.1, this section is aimed at discussing the calibration of the stopping criterion of *IMSMRA-LS*. More in detail, the following considerations will focus on the choice of the threshold $\gamma_{\mathcal{H}}$, since the values of the other parameters have already been discussed in Sect. 4.2.4.

In order to choose the proper value of $\gamma_{\mathcal{H}}$, the scattering configuration is the same as in Sect. 4.2.4, namely a rectangular scatterer ($L = 0.27\lambda$ and $W = 0.13\lambda$) characterized by a dielectric permittivity $\epsilon_C = 1.8$ and centered at $x^c = -\frac{2}{3}\lambda$, $y^c = \lambda$ within an investigation domain of side $L_D = 3\lambda$. Figure 5.6 shows the behavior of the cost function, while the reconstructions achieved by using different numerical values of $\gamma_{\mathcal{L}}$ are depicted in Fig. 5.7 [$\gamma_{\mathcal{L}} = 5.0$ - Fig. 5.7(a), $\gamma_{\mathcal{L}} = 1.5$ - Fig. 5.7(b), $\gamma_{\mathcal{L}} = 0.7$ - Fig. 5.7(c)]. As previously discussed (Sect. 4.2.4), the number of total iterations k_{tot} decreases as the value of the threshold decreases. As a matter of fact, $\gamma_{\mathcal{L}}$ represents the maximum Hausdorff distance (expressed in terms of $l_s|_{q_s}$) between the trial solution at iterations k_s and the one at k_s+1. Therefore, the smaller the value of $\gamma_{\mathcal{L}}$ is, the fewer the differences between two trial solutions should be in order to meet the requirements of the stopping criterion. Such more strict condition usually occurs when the iteration index increases. However, a good trade-off between the arising computational burden and the accuracy of the reconstruction can be achieved when setting $\gamma_{\mathcal{L}} = 1.5$ (i.e., the Hausdorff distance between two trial solutions can be $1.5 \times l_s|_{q_s}$ at most).

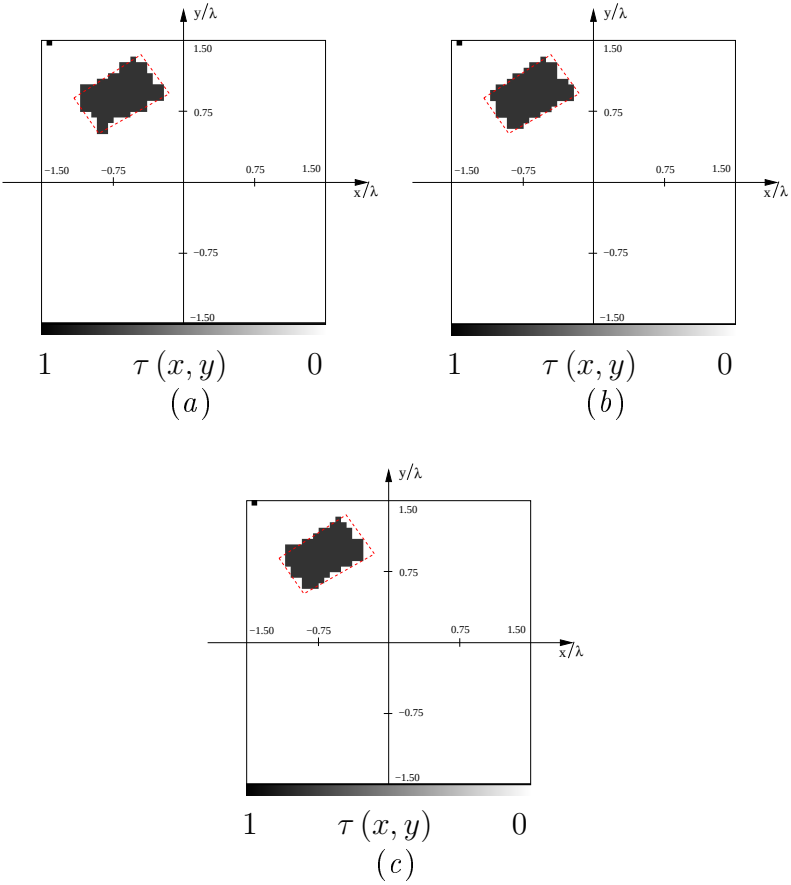

Figure 5.7: Numerical Data. Rectangular cylinder ($\epsilon_C = 1.8$, $L_D = 3\lambda$, *Noiseless Case*). Reconstructions obtained at the end of the iterative procedure with *IMSMRA-LS* when varying $\gamma_{\mathcal{L}}$ [(a) $\gamma_{\mathcal{L}} = 5.0$, (b) $\gamma_{\mathcal{L}} = 1.5$, (c) $\gamma_{\mathcal{L}} = 0.7$].

5.3 Numerical Validation: Synthetic Data

In order to assess the effectiveness of the *IMSMRA-LS* technique, some representative results concerned with geometries characterized by more than one object are presented in this section. In order to assess the accuracy of the reconstructions, the error figures described in Sect. 4.2 will be considered.

5.3.1 Inversion of Data scattered by Two Dielectric Cylinders

The first synthetic test case is characterized by two dielectric cylinders placed inside a square investigation domain of side $L_D = 3\lambda$. In the first experiment, $P = 2$ circular scatterers characterized by a radius $\rho = 7\lambda/15$ and a dielectric permittivity $\epsilon_C = 1.8$ are centered at $(x^c|_1 = 5\lambda/6,\ y^c|_1 = 5\lambda/6)$ and $(x^c|_2 = -5\lambda/6,\ y^c|_2 = -5\lambda/6)$. According to the guidelines pointed out in [15], the imaging setup is made up of $V = 30$ sources and $M = 30$ measurement points for each view v. Consequently, in order to fully exploit the multi-resolution approach, D_I is partitioned into $N_{MR} = 19 \times 19$ sub-domains.

Figure 5.8 shows the reconstructions achieved at the end of the steps of the multi-resolution process [Figs. 5.8(a)-(c)] and the optimal inversion (i.e., the true scatterer sampled at the spatial resolution used to generate data) [Fig. 5.8(d)]. The regions of interest defined at the resolution levels $s = 2$ and $s = s_{opt} = 3$ are traced by the green dashed line in Fig. 5.8(b)

and in Fig. 5.8(c), respectively. At step $s = 2$, only one RoI is detected ($Q_{s=2} = 1$), although two scatterers are found at the previous step. Such a behavior is due to the criterion used for the definition of the region of interest, whose size is computed with a variable allowance $\mathcal{A}$ in order to increase gradually the spatial resolution during the multi-step procedure. At step $s = 3$, when the allowance on the size of the RoIs decreases, the number of regions of interest increases as expected up to the number of scatterers ($Q_{s=3} = 2$). As for the quality of the reconstruction, the increment of the spatial resolution is obvious especially between the steps $s = 2$ and $s = s_{opt} = 3$. Both scatterers are better localized at s_{opt}, as confirmed by the localization errors: $\delta|_{1,\,s=2} = 1.30$ vs. $\delta|_{1,\,s=3} = 1.26$, $\delta|_{2,\,s=2} = 1.72$ vs. $\delta|_{2,\,s=3} = 0.26$. Moreover, the area error decreases when the spatial resolution increases: $\Delta|_{s=2} = 1.65$ vs. $\Delta|_{s=3} = 1.09$.

The improvement of the quality of the reconstructions during the multi-scaling procedure is also clearly visible in the behavior of the cost function, which is characterized by two "jumps" at the beginning of both steps $s = 2$ and $s = s_{opt} = 3$. For the sake of completeness, both regions of interest are discretized in $N(q_s)\rfloor_{MR} = 13 \times 13$ sub-domains at $s = s_{opt} = 3$, according to the multi-region procedure explained in Sect. 5.1. As a consequence, since the complexity of the algorithm is of the order of $\mathcal{O}\left(2 \times \eta_s^3\right)$, $\eta_s = \sum_{q_s=1}^{Q_s} N(q_s)\rfloor_{MR}$, the computational cost at each iteration of the step s_{opt} is lower than the cost at s_2, since $\eta_{s=2} = 361$ and $\eta_{s=3} = 338$.

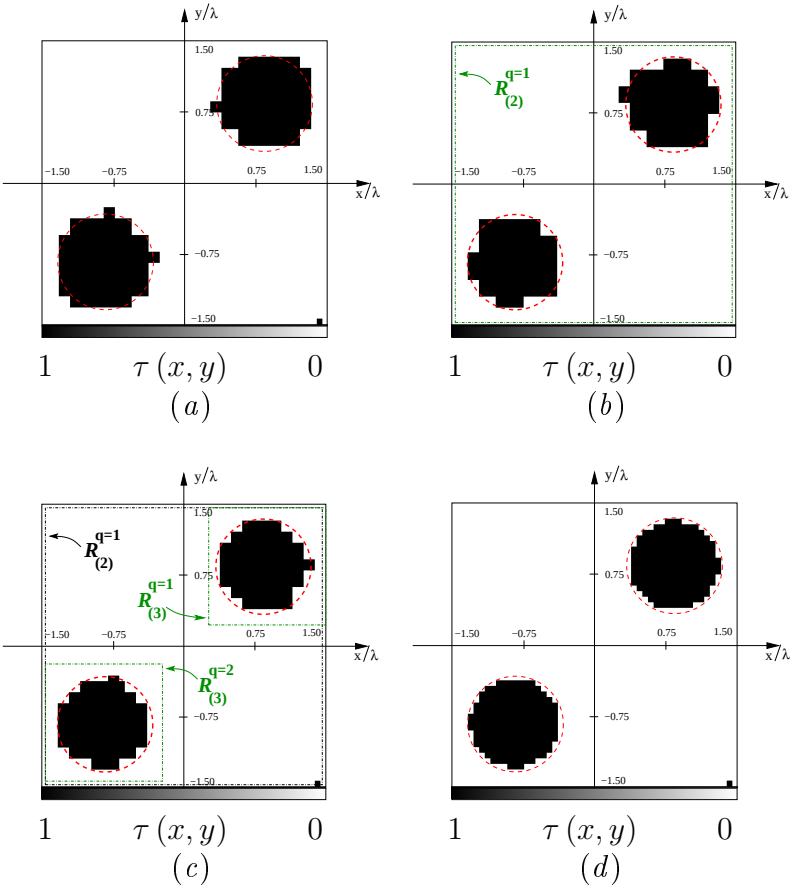

Figure 5.8: Numerical Data. Two discs ($\epsilon_C = 1.8$, $L_D = 3\lambda$, *Noiseless Case*). Reconstructions with *IMSMRA-LS* at (a) $s = 1$ and (b) $s = 2$, (c) $s = s_{opt} = 3$. Optimal inversion (d).

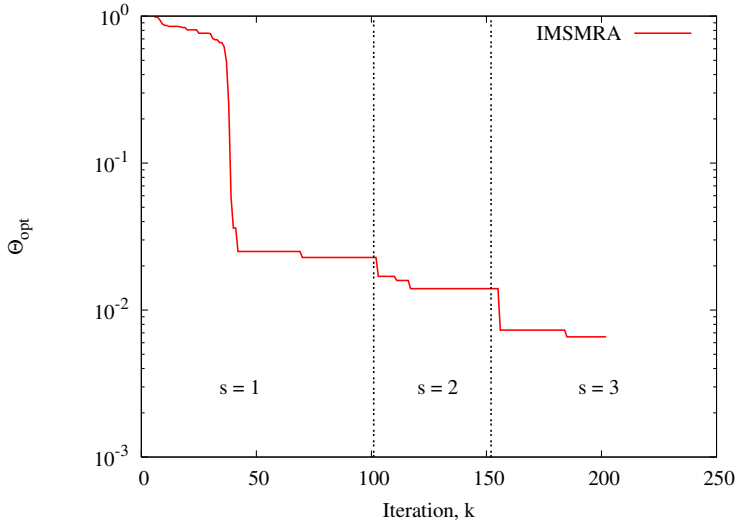

Figure 5.9: Numerical Data. Two discs ($\epsilon_C = 1.8$, $L_D = 3\lambda$, *Noiseless Case*). Behavior of the cost function when using *IMSMRA-LS*.

In order to further analyze the proposed approach, Figures 5.10-5.12 shows the reconstructions when dealing with noisy data [$SNR = 20\,dB$ - Figs. $5.10(a)$, $SNR = 10\,dB$ - $5.11(a)$, and $SNR = 10\,dB$ - $5.12(a)$]. The multi-region technique is compared with *IMSA-LS* [$SNR = 20\,dB$ - Figs. $5.10(b)$, $SNR = 10\,dB$ - $5.11(b)$, and $SNR = 10\,dB$ - $5.12(b)$] as well as the *Bare-LS* approach [$SNR = 20\,dB$ - Figs. $5.10(c)$, $SNR = 10\,dB$ - $5.11(c)$, and $SNR = 10\,dB$ - $5.12(c)$]. As previously discussed in Ch. 4, the multi-scaling approach usually appears to achieve better reconstructions than the *Bare-LS*

strategy when data are affected by a high level of noise. As expected, the quality of the reconstructions of *IMSMRA-LS* does not worsen when the SNR decreases, while the performance of the *IMSA-LS* is limited by the distance between the scatterers, since only a region of interest is exploited. Such a behavior is further confirmed by the reconstruction errors versus the SNR shown in Fig. 5.13. While the area error of *IMSA-LS* is about three times higher than the one of *IMSMRA-LS*, the localization errors of the multi-scaling techniques appears to be similar when $SNR = 5\,dB$. As for the *Bare* approach, barycentre and shape of the scatterers are usually accurately estimated and the reconstruction at $SNR = 20\,dB$ appears to be better than the one of *IMSMRA-LS*. As a matter of fact, the multi-scaling procedure of *IMSMRA-LS* stops at $s = 2$ when $SNR = 20\,dB$ and only one region of interest is detected ($Q_{s=2} = 1$). As a result, the spatial resolution is not increased, since the zooming on the regions of interest is not carried out. Such a situation is a consequence of the high value of the allowance $\mathcal{A}$ at $s = 2$ ($\mathcal{A}_{s=2} = 40\%$ vs. $\mathcal{A}_{s=3} = 30\%$). As a matter of fact, $\mathcal{A}$ has to be large enough to include correctly the estimated shapes in the regions of interest, but at the same time it should be as small as possible to enhance the spatial resolution.

In order to discuss the computational effectiveness of *IMSMRA-LS*, let us consider the behavior of the cost function when $SNR = 5\,dB$ (Fig. 5.14).

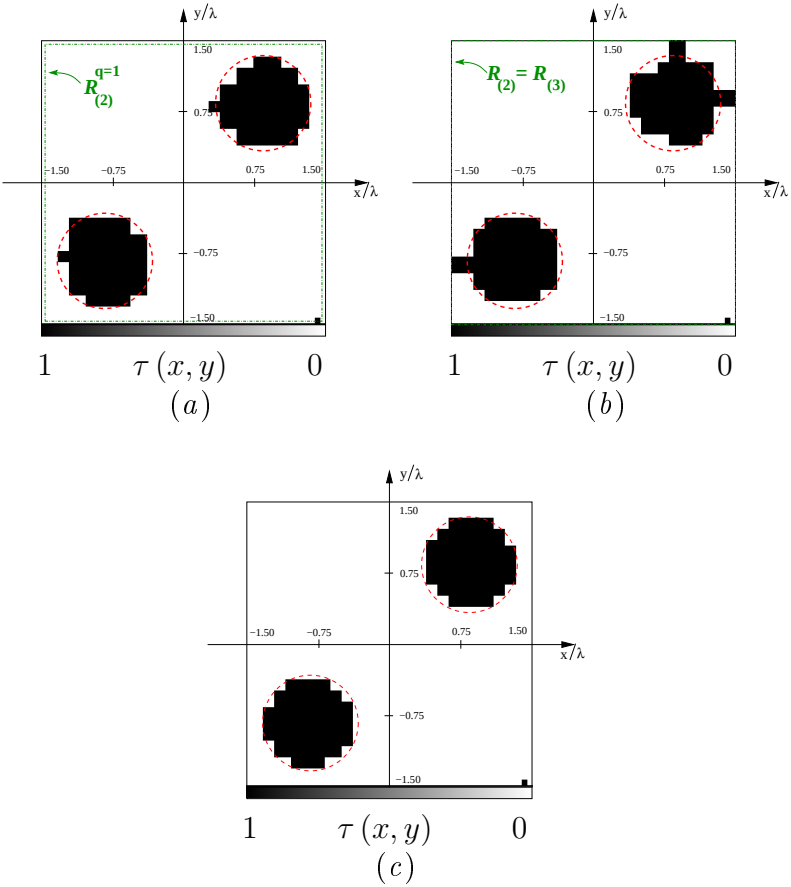

Figure 5.10: Numerical Data. Two discs ($\epsilon_C = 1.8$, $L_D = 3\lambda$, $SNR = 20\,dB$). Reconstructions with *IMSMRA-LS* (a), *IMSA-LS* (b), and *Bare-LS* (c).

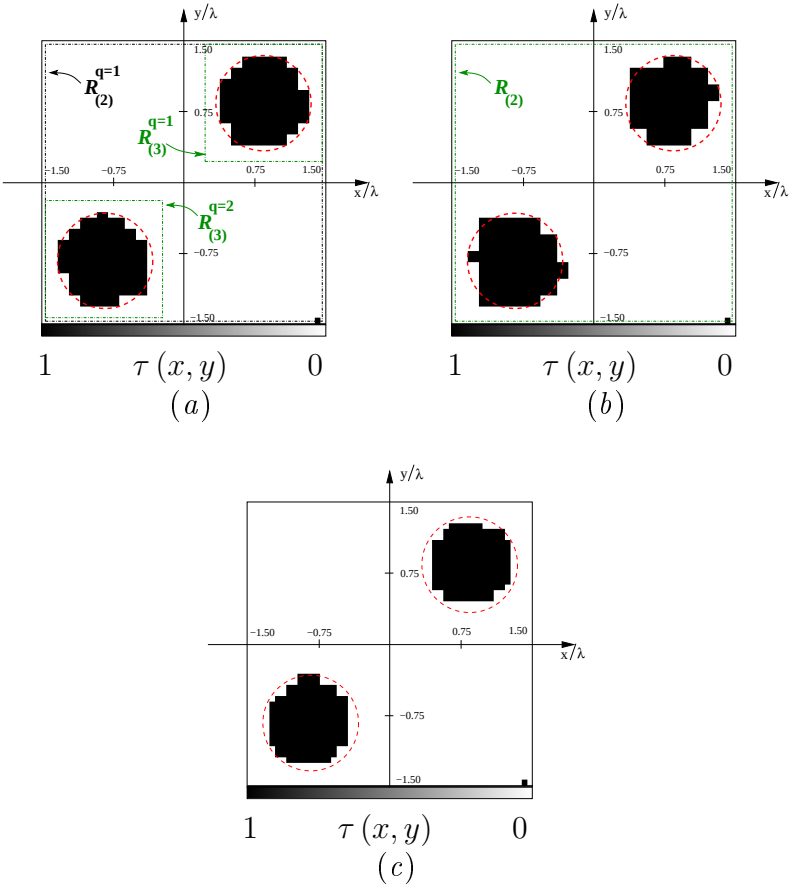

Figure 5.11: Numerical Data. Two discs ($\epsilon_C = 1.8$, $L_D = 3\lambda$, $SNR = 10\,dB$). Reconstructions with *IMSMRA-LS* (a), *IMSA-LS* (b), and *Bare-LS* (c).

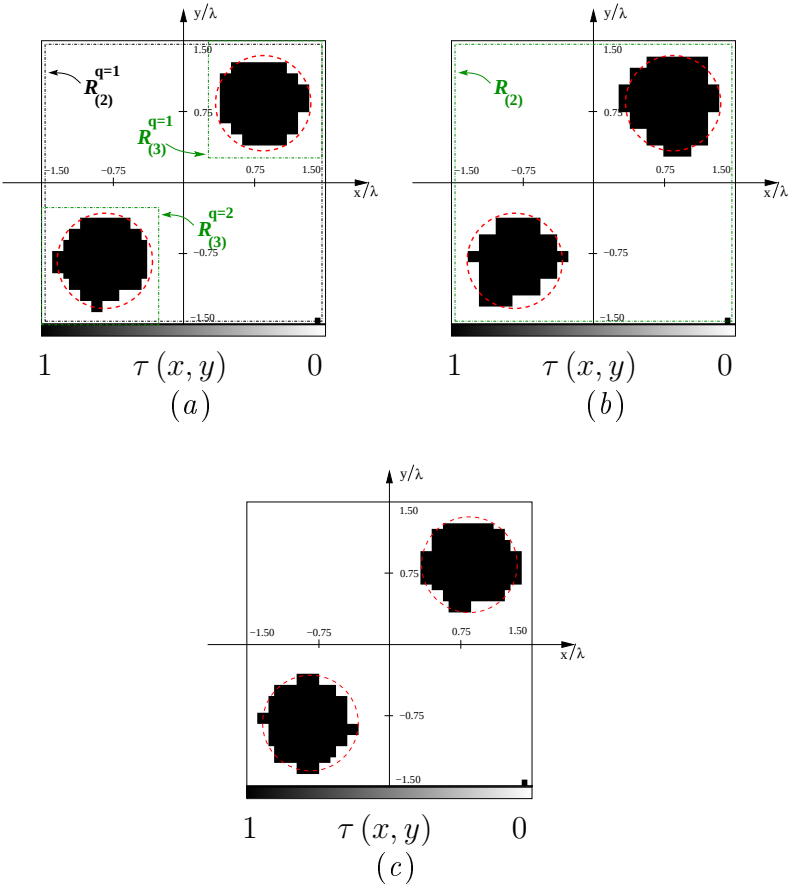

Figure 5.12: Numerical Data. Two discs ($\epsilon_C = 1.8$, $L_D = 3\lambda$, $SNR = 5\,dB$). Reconstructions with *IMSMRA-LS* (a), *IMSA-LS* (b), and *Bare-LS* (c).

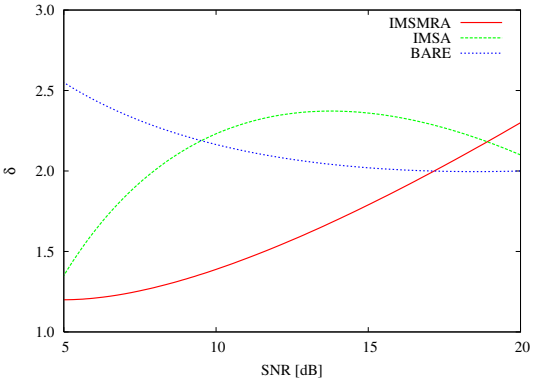

(a)

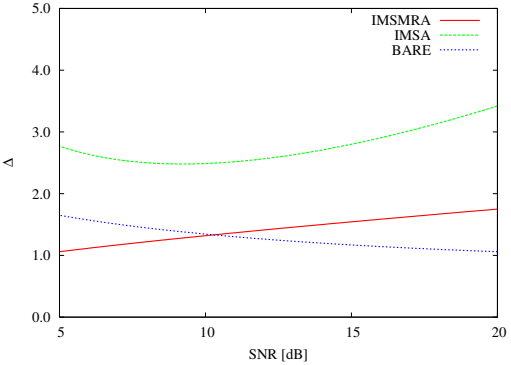

(b)

Figure 5.13: Numerical Data. Two discs ($\epsilon_C = 1.8$, $L_D = 3\lambda$, $SNR = 5\,dB$). Values of the error figures versus SNR.

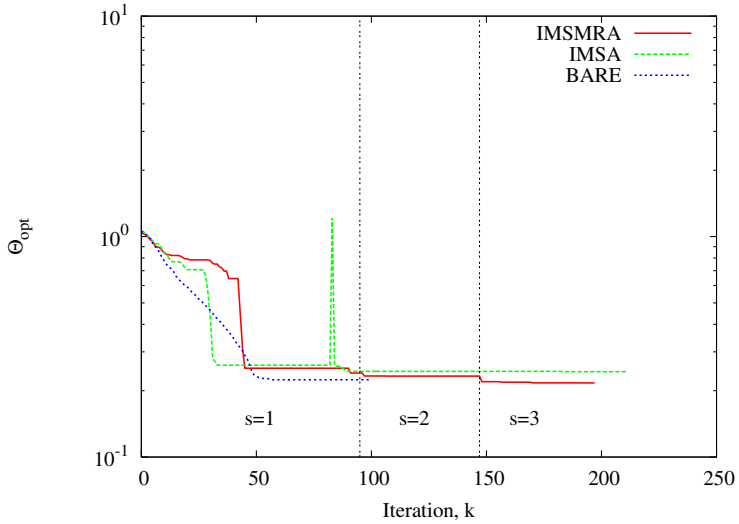

Figure 5.14: Numerical Data. Two discs ($\epsilon_C = 1.8$, $L_D = 3\lambda$, $SNR = 5\,dB$). Behavior of the cost function.

In agreement with the quality of the reconstructions and the error figures at the lowest SNR, the final value of the cost function of the multi-region approach is characterized by a lower value than those of the *Bare-LS* and *IMSA-LS*. Moreover, *IMSMRA-LS* requires less iterations to achieve the optimal solution ($k_{tot}\rfloor_{IMSMRA-LS} = 198$ vs. $k_{tot}\rfloor_{IMSA-LS} = 212$). On the other hand, *IMSMRA-LS* is not characterized by a faster convergence with respect to the *Bare* approach. However, the multi-region methodology appears to be, as expected, more computational effective than the other approaches. That

	$IMSMRA-LS$	$IMSA-LS$	$Bare-LS$
	$SNR = 5\,dB$		
$k_{s=1}^{opt}$	95	84	101
$N_{s=1}$	361	361	900
$k_{s=2}^{opt}$	53	84	–
$N_{s=2}$	361	361	–
$k_{s=3}^{opt}$	50	–	–
$N_{s=3}$	338	–	–
f_{pos}	8.89×10^9	9.97×10^9	7.36×10^{10}

Table 5.1: Numerical Data. Two discs ($\epsilon_C = 1.8$, $L_D = 3\lambda$, $SNR = 5\,dB$). Computational indexes.

is, the total number of complex floating point operations $f_{pos} = \sum_{s=1}^{s_{opt}} \mathcal{O}\left(2 \times \eta_s^3\right) \times k_s^{opt}$, $\eta_s = \sum_{q_s=1}^{Q_s} N(q_s)\rfloor_{MR}$, N_{IMSA}, $N_{Bare-LS}$, of *IMSMRA-LS* is lower than the ones of the other methods (Tab. 5.1).

In the second experiment, $P = 2$ rectangular scatterers ($L|_1 = \lambda/2$, $W|_1 = 5\lambda/6$, $L|_2 = 5\lambda/6$, and $W|_2 = \lambda/2$) are located inside a square investigation domain ($L_D = 3\lambda$) with barycentres ($x^c|_1 = 2\lambda/3$, $y^c|_1 = 2\lambda/3$) and ($x^c|_2 = -2\lambda/3$, $y^c|_2 = -2\lambda/3$). The reconstructions achieved by *IMSMRA-LS*, *IMSA-LS*, and *Bare-LS* when $SNR = 20\,dB$ are shown in Fig. 5.15. The result obtained in this experiment further confirms the effectiveness of the multi-region methodology, since both positions and shapes of the rectangular scatterers appear to be accurately estimated [Fig. 5.15(a)]. As a confirmation, the

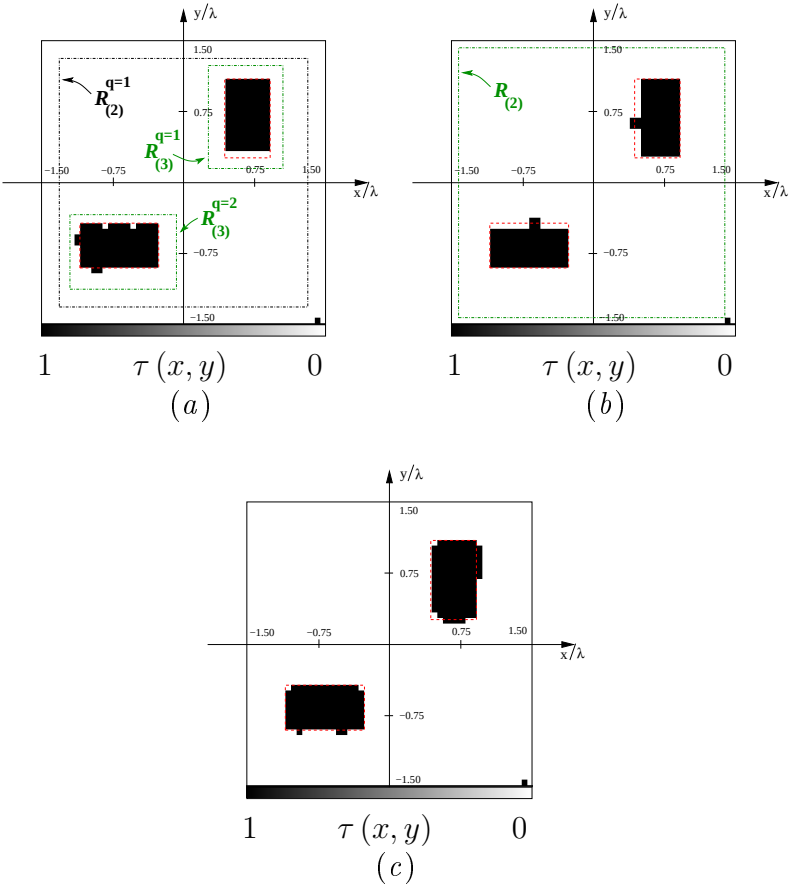

Figure 5.15: Numerical Data. Two rectangular scatterers ($\epsilon_C = 1.8$, $L_D = 3\lambda$, $SNR = 20\,dB$). Reconstructions with *IMSMRA-LS* (a), *IMSA-LS* (b), and *Bare-LS* (c).

	$IMSMRA-LS$	$IMSA-LS$	$Bare-LS$
	$SNR = 20\,dB$		
$< \delta >$	2.98	3.40	2.43
Δ	0.34	0.61	0.57

Table 5.2: Numerical Data. Two rectangular scatterers ($\epsilon_C = 1.8$, $L_D = 3\lambda$, $SNR = 20\,dB$).Values of the error indexes.

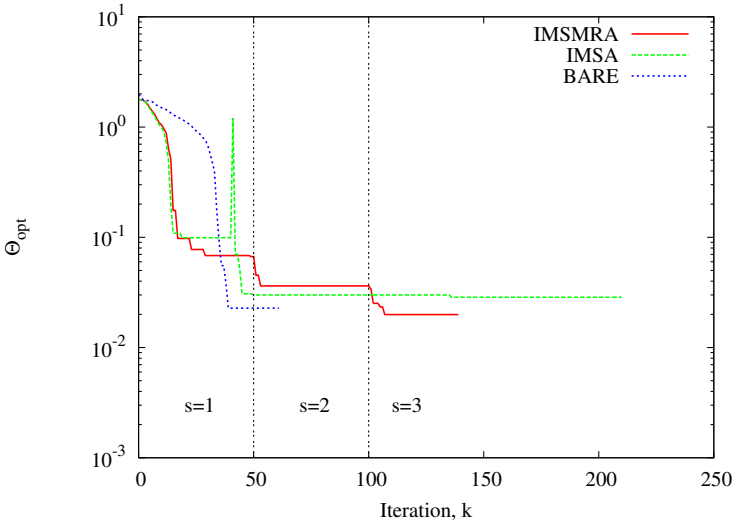

Figure 5.16: Numerical Data. Two rectangular scatterers ($\epsilon_C = 1.8$, $L_D = 3\lambda$, $SNR = 20\,dB$). Behavior of the cost function.

reconstruction errors of *IMSMRA-LS* are lower than those of the other methods, except for the average localization error which is of the same order of magnitude as the one of *Bare-LS*.

The behavior of the cost functions of *IMSMRA-LS*, *IMSA-LS*, and *Bare-LS* is depicted in Fig. 5.16. As just indicated, the final value of the error is lower than the ones of the other methods. As for the computational burden, the *IMSMRA-LS* is characterized by a faster convergence with respect to *IMSA-LS*. Furthermore, the arising total number of complex floating point operations appears to be the lowest ($f_{pos}\rfloor_{IMSMRA-LS} = 6.24 \times 10^9$ vs. $f_{pos}\rfloor_{Bare-LS} = 4.52 \times 10^{10}$).

5.3.2 Experiment with Three Objects

This experiment is aimed at illustrating the behavior of the *IMSA-LS* when dealing with $P = 3$ scatterers ($\epsilon_C = 2.0$) characterized by simple shapes but distanced from one another. The test geometry is characterized by an elliptic cylinder ($x^c|_1 = -\frac{4}{5}\lambda$, $y^c|_1 = -\frac{4}{5}\lambda$, and $\alpha|_1 = \frac{1}{2}\lambda$, $\beta|_1 = 0.43\lambda$ as axes), a circular scatterer ($x^c|_2 = 0$, $y^c|_2 = \frac{4}{5}\lambda$, $\rho|_2 = \frac{1}{4}\lambda$), and a square object ($x^c|_3 = \frac{4}{5}\lambda$, $y^c|_3 = \frac{4}{5}\lambda$, $L|_3 = 0.83\lambda$ and $W|_3 = \frac{1}{2}\lambda$) located in a square investigation domain characterized by $L_D = 3\lambda$. By adopting the same arrangement of emitters and receivers as in Section 5.2.2, the investigation do-

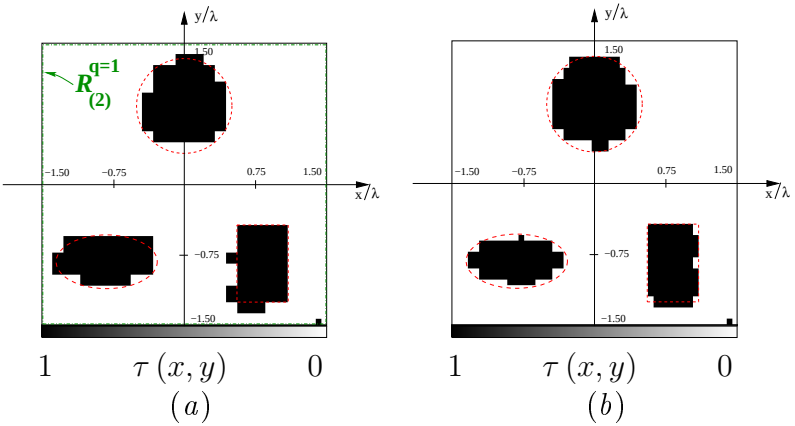

Figure 5.17: Numerical Data. Three scatterers ($\epsilon_C = 1.8$, $L_D = 3\lambda$, $SNR = 20\,dB$). Reconstructions with *IMSMRA-LS* (a) and *Bare-LS* (b).

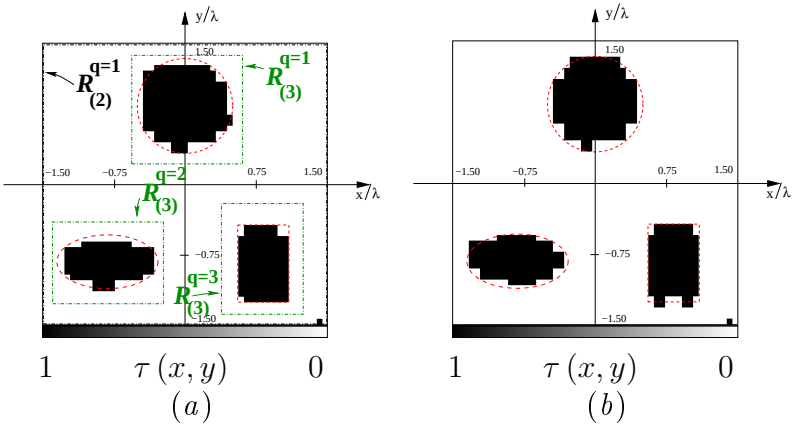

Figure 5.18: Numerical Data. Three scatterers ($\epsilon_C = 1.8$, $L_D = 3\lambda$, $SNR = 10\,dB$). Reconstructions with *IMSMRA-LS* (a) and *Bare-LS* (b).

main is discretized with $N_{MR} = 23\times23$ and $N_{Bare-LS} = 31\times31$ square cells for the *IMSMRA-LS* and the *Bare-LS*, respectively. Moreover, Δt_1 is set to 0.03.

Figures 5.17-5.20 show the results from the comparative study carried out in correspondence with different values of signal-to-noise ratio. As shown by the reconstructions (Figs. 5.17-5.19) and as expected, the multi-resolution approach provides more accurate results and appears to be more reliable than the *Bare-LS* especially with low SNR. This conclusion is further confirmed by the behavior of the reconstruction errors (Fig. 5.20), for which the *IMSMRA-LS* achieves a lower localization error as well as a lower area error than those of *Bare-LS,*

especially for $SNR = 5\,dB$ ($N(q_s)\rfloor_{MR} = 16{\times}16$, $q_s = 1, ..., Q_s$, with $s = s_{opt} = 3$ and $Q_{s=3} = 3$). On the other hand, both algorithms provide good estimates of the scatterer under test when inverting data affected by low noise [$SNR = 20\,dB$ - Fig. 5.17(a) vs. Fig. 5.17(b); Fig. 5.20(a) and (b)].

5.3.3 Experiments with Complex Shapes

The third test case with synthetic data is concerned with scatterers characterized by complex shapes. In the first experiment, two higher permittivity ($\epsilon_C = 2.5$) cylindrical rings are centered at ($x^c|_1 = \lambda/4$, $y^c|_1 = 3\lambda/4$) and ($x^c|_2 = \lambda$, $y^c|_2 = \lambda$)

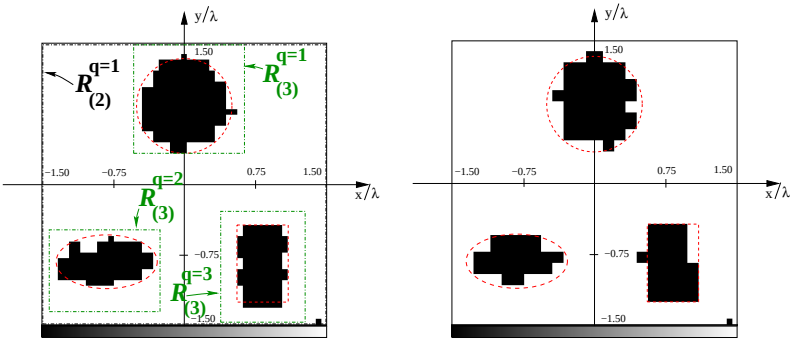

Figure 5.19: Numerical Data. Three scatterers ($\epsilon_C = 1.8$, $L_D = 3\lambda$, $SNR = 5\,dB$). Reconstructions with *IMSMRA-LS* (a) and *Bare-LS* (b).

in a square investigation domain of side $L_D = 5\lambda$. The external radius of the rings is $\rho_{ext} = \lambda/3$ and the internal one is $\rho_{int} = \lambda/6$, so that the scatterer are not joined. The imaging setup is made up of $V = 40$ sources and $M = 40$ measurement points for each view v, while the investigation domain is discretized in $N_{MR} = 29 \times 29$ and $N_{Bare-LS} = 50 \times 50$ for *IMSMRA-LS* and *Bare-LS*, respectively.

Figures 5.21 and 5.22 show the reconstruction achieved when considering $SNR = 20\,dB$ and $SNR = 10\,dB$, respectively. The multi-region approach obtains the final result at the end of the step $s = s_{opt} = 2$, with $Q_{s=2} = 1$. The *RoI* is characterized by a rectangular shape, in order to better represent the area where the scatterer are located. The reconstruction is characterized by a correct estimation of position and shape of the circular scatterer, even though the objects are not separated [Fig. 5.21(a)]. On the other hand, the result of *Bare-LS* is noticeably less accurate, since the symmetry of the true shapes is not retrieved [Fig. 5.21(b)]. However, the cost function of *Bare* ends up with an error lower than the value achieved by *IMSMRA-LS*.

The same conclusions hold true when increasing the level of noise on the data ($SNR = 10\,dB$ - Fig. 5.22). In such a case, the reconstruction obtained by the multi-region [Fig. 5.22(a)] appears to be as accurate as the result in Fig. 5.21(a). On the other hand, the *Bare* approach is not able to reconstruct the scatterer, even though the artifacts are mainly located on the discs. This result is further confirmed by the behavior of the error functions, since the final value of *IMSMRA-LS* is lower than that of *Bare-LS*.

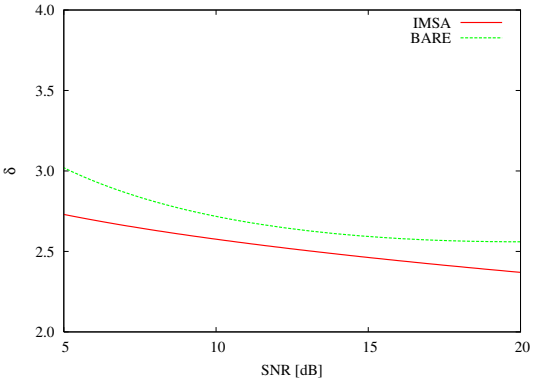

(a)

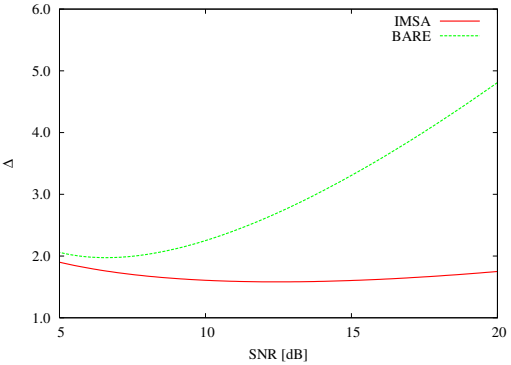

(b)

Figure 5.20: Numerical Data. Three scatterers ($\epsilon_C = 1.8$, $L_D = 3\lambda$, *Noisy Case*). Values of the error figures versus SNR.

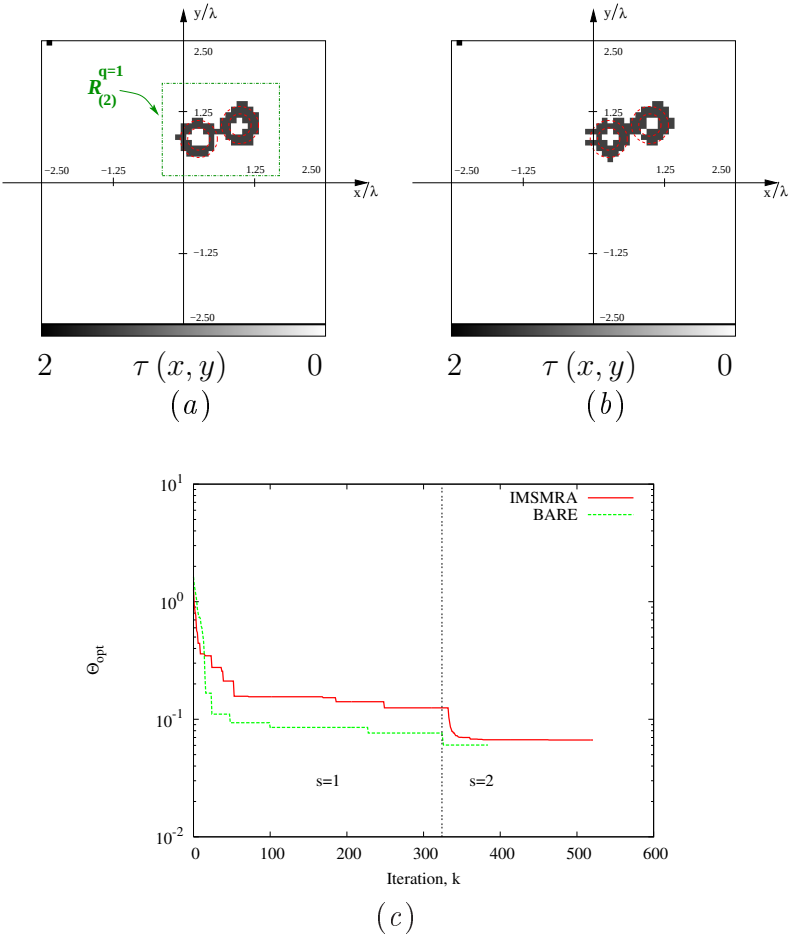

Figure 5.21: Numerical Data. Two hollow cylinders ($\epsilon_C = 2.5$, $L_D = 5\lambda$, $SNR = 20\,dB$). Reconstructions with (a) *IMSMRA-LS* and (b) *Bare-LS*. Behavior of the cost function (c).

The second experiment deals with three scatterers characterized by the complex shapes depicted by the red dashed line in Figs. 5.23(a) and 5.23(b). The objects are centered at ($x^c|_1 = -5\lambda/4,\ y^c|_1 = 6\lambda/5$), ($x^c|_2 = \lambda,\ y^c|_2 = \lambda$), and ($x^c|_2 = \lambda,\ y^c|_2 = \lambda$), letting $L_D = 5\lambda$. The measurement setup is the same as the one in the first experiment and the investigation domain is discretized in $N_{MR} = 29 \times 29$ and $N_{Bare-LS} = 50 \times 50$ for *IMSMRA-LS* and *Bare-LS*, respectively.

The reconstructions achieved when $SNR = 20\,dB$ are characterized by an accurate estimation of location and shape of the scatterer, both for *IMSMRA-LS* and *Bare-LS*. More in detail, the multi-region approach retrieves the shape of cross-shaped scatterer better than *Bare*, while the circular obstacle is sligthly overestimated ($N(q_s = 1)\rfloor_{MR} = 13 \times 13,\ N(q_s = 2)\rfloor_{MR} = 13 \times 13,\ N(q_s = 3)\rfloor_{MR} = 21 \times 21$, with $s = s_{opt} = 3$ and $Q_{s=3} = 3$). As for the rectangular scatterer, the reconstructions achieved by *IMSMRA-LS* and *Bare-LS* are similar. For what concerns the behavior of the cost function [Fig. 5.23(c)], the final error of *IMSMRA-LS* appears to be lower than that of *Bare-LS*. Furthermore, the total number of floating point operations required by the multi-region strategy is lower with respect to the single-region's case ($f_{pos}\rfloor_{IMSMRA-LS} = 5.78 \times 10^{11}$ vs. $f_{pos}\rfloor_{Bare-LS} = 2.52 \times 10^{12}$). Finally, the error figures [$< \delta >$ - Fig. 5.24(a), Δ - Fig. 5.24(b)] confirm that in general the multi-region approach is more effective in the estimation of the shape, especially with noisy data.

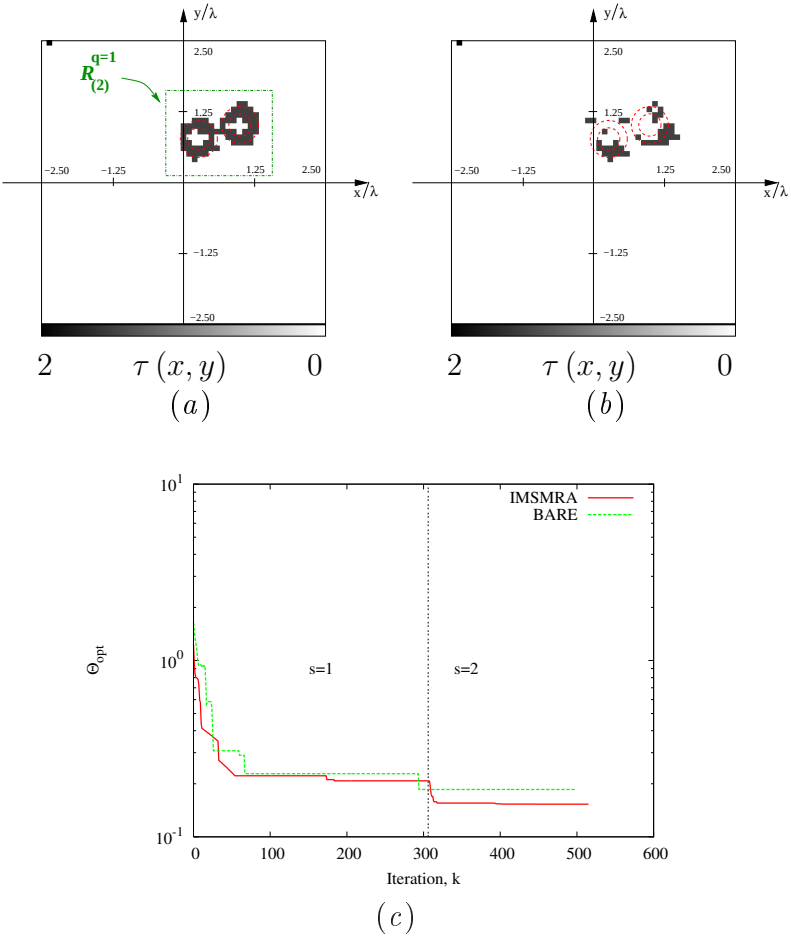

Figure 5.22: Numerical Data. Two hollow cylinders ($\epsilon_C = 2.5$, $L_D = 5\lambda$, $SNR = 10\,dB$). Reconstructions with (a) *IMSMRA-LS* and (b) *Bare-LS*. Behavior of the cost function (c).

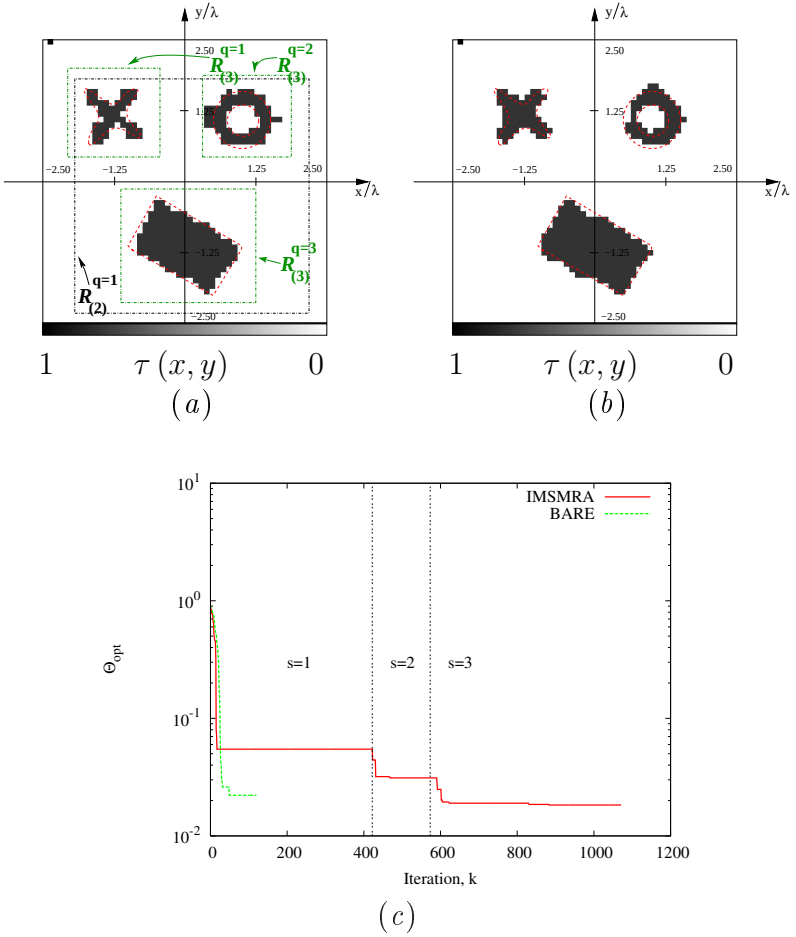

Figure 5.23: Numerical Data. Three objects characterized by complex shapes ($\epsilon_C = 1.8$, $L_D = 5\lambda$, $SNR = 20\,dB$). Reconstructions with (a) *IMSMRA-LS* and (b) *Bare-LS*. Behavior of the cost function (c).

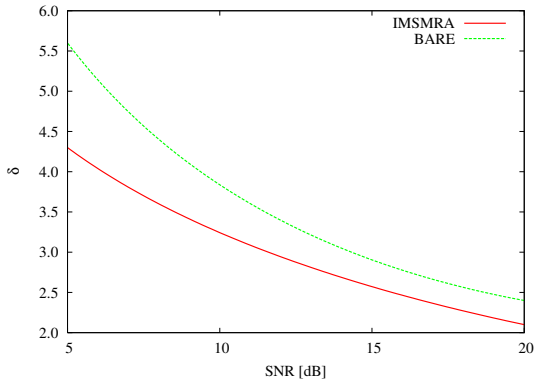

(a)

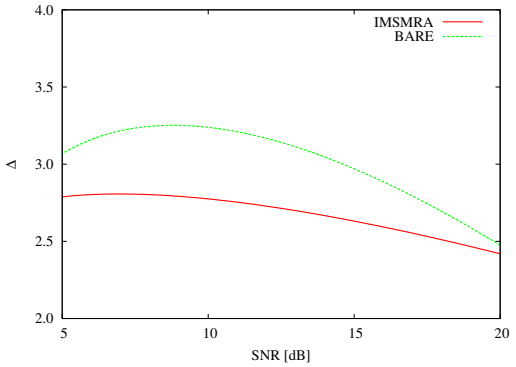

(b)

Figure 5.24: Numerical Data. Three objects characterized by complex shapes ($\epsilon_C = 1.8$, $L_D = 5\lambda$, *Noisy Case*). Values of the error figures versus SNR.

5.4 Validation by using Laboratory-Controlled Data

The last experiment of this thesis deals with the data collected at the laboratories of the *Institut Fresnel* in Marseille (France) in 1999 [100]. The multiple-frequency angular-diversity bistatic dataset "*twodielTM_4f.exp*" consists of the field samples scattered by two off-centered homogeneous circular cylinders ($\rho = 15\,\mathrm{mm}$) characterized by a nominal value of the object function equal to $\tau(\underline{r}) = 2.0 \pm 0.3$ and located in an investigation domain assumed in the following of square geometry and extension $30 \times 30\,\mathrm{cm}^2$. The field samples are collected in $M(v) = 49$ measurement points, according to the $V = 36$ different angular direction of the source ($v = 1, ..., V$).

In Fig. 5.25, the reconstructions achieved by *IMSMRA-LS* [Figs. 5.25(a) and (c)] are compared with those of *Bare-LS* [Figs. 5.25(b) and (d)] at $F = 2$ different frequencies. By setting $\epsilon_C = 3.0$, the scatterers are always accurately localized. On the other hand, the estimation of the shape of the targets appears to be less accurate, especially for the *Bare-LS* and at the highest frequency ($f = 4\,GHz$). However, the reconstructed structures cover in all cases a large part of the true object, depicted by the red dashed line in Fig. 5.25. These conclusions are further confirmed by the behavior of cost functions, reported in Fig. 5.26.

Such a good performance of both the reconstruction algorithms when dealing with laboratory-controlled data could depend on to the low level of noise characterizing the measure-

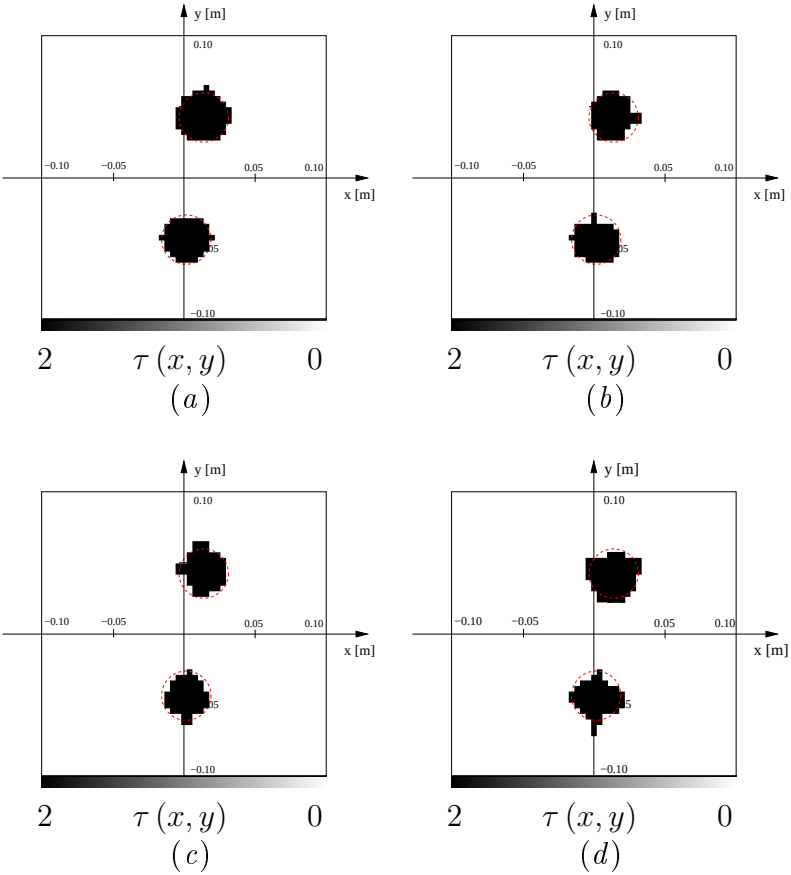

Figure 5.25: Experimental Data (Dataset "Marseille" [100]). Two circular cylinders ("*twodielTM_4f.exp*"). Reconstructions with *IMSMRA-LS* (left column) and *Bare-LS* (right column) at different frequencies f [$f = 2\,GHz$ $(a)(b)$; $f = 4\,GHz$ $(c)(d)$].

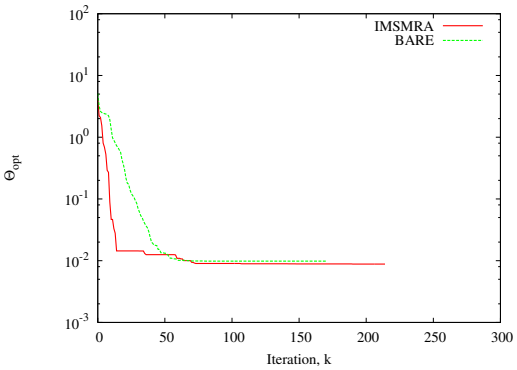

(a)

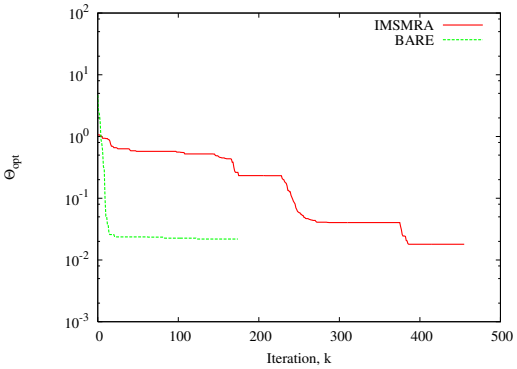

(b)

Figure 5.26: Experimental Data (Dataset "Marseille" [100]). Two circular cylinders ("*twodielTM_4f.exp*"). Behavior of the cost function versus the number of iterations when (a) $f = 2\,GHz$, and (b) $f = 4\,GHz$.

ments, thus further confirming the hypothesis of a low-noise environment as already evidenced in [101].

Chapter 6

Conclusions and Open Problems

In this chapter, some conclusions are drawn and further advances are envisaged in order to address the open problems.

In this thesis, a multi-resolution approach for qualitative imaging purposes based on shape optimization has been presented. The proposed strategy integrates the multi-scale method and the level set representation of the problem unknowns in order to profitably exploit the amount of information collectable from the scattering experiments as well as the available *a-priori* information on the scatterer under test. Two implementations have been presented in order to effectively deal with configurations characterized by one or multiple objects.

In general, the main key features of the multi-resolution level set approach can be summarized as follows:

- innovative multi-level representation of the problem unknowns in the shape-deformation-based reconstruction technique;
- effective exploitation of the scattering data through the iterative multi-step strategy;
- limitation of the risk of being trapped in false solutions thanks to the reduced ratio between data and unknowns;
- useful exploitation of the *a-priori* information (i.e., object homogeneity) about the scenario under test;
- enhanced spatial resolution limited to the region of interest.

From the validation concerned with different scenarios and both synthetic and experimental data, the following conclusions can be drawn:

- the *IMSA-LS* usually proved more effective than the single-resolution implementation, especially when dealing with corrupted data scattered from simple as well as complex geometries characterized by one target;
- the *IMSMRA-LS* appeared to be as effective as the single-region implementation when dealing with simple geometries, while the effective multi-region architectures improved the reconstruction accuracy when considering multiple scatterers;
- the integrated strategy (i.e., *IMSA-LS* and *IMSMRA-LS*) appeared less computationally-expensive than the standard approach in reaching a reconstruction with the same level of spatial resolution within the support of the object.

However, the actual implementation is still characterized by open problems. For instance, the regularity of the level set function needs to be preserved during the level set update according to the distance-function-based initialization. Furthermore, different velocity functions should be considered in order to find the optimal compromise between the reconstruction accuracy and the numerical stability. These and other related aspects will have to be further investigated, especially to deal with the more attractive but also more numerically complicated three-dimensional inverse scattering problem.

References

[1] P. J. Shull, *Nondestructive Evaluation: Theory, Techniques and Applications.* CRC Press, Boca Raton, 2002.

[2] J. Baruchel, J.-Y. Buffière, E. Maire, P. Merle, and G. Peix, *X-Ray Tomography in Material Science.* Hermes Science, Paris, 2000.

[3] L. W. Schmerr, *Fundamentals of Ultrasonic Nondestructive Evaluation: A Modeling Approach.* Springer, Berlin, 1998.

[4] B. A. Auld and J. C. Moulder, "Review of advances in quantitative eddy current nondestructive evaluation", *J. Nondestructive Evaluation*, vol. 18, no. 1, pp. 3-36, Mar. 1999.

[5] S. Kharkovsky and R. Zoughi, "Microwave and millimeter wave nondestructive testing and evaluation - Overview and recent advances," *IEEE Instrum. and Meas. Mag.*, vol. 10, pp. 26-38, Apr. 2007.

[6] R. Zoughi, *Microwave Nondestructive Testing and Evaluation*. Dordrecht, The Netherlands: Kluwer Academic Publishers, 2000.

[7] J. Ch. Bolomey, "Microwave imaging techniques for NDT and NDE," *Proc. Training Workshop on Advanced Microwave NDT/NDE Techniques*, Supelec/CNRS, Paris, Sept. 7-9, 1999.

[8] J. Ch. Bolomey. *Frontiers in Industrial Process Tomography*. Engineering Foundation, New York, 1995.

[9] T. Rubk, P. M. Meaney, P. Meincke, and K. D. Paulsen, "Nonlinear microwave imaging for breast-cancer screening using Gauss-Newton's method and the CGLS inversion algorithm," *IEEE Trans. Antennas Propagat.*, vol. 55, pp. 2320-2331, Aug. 2007.

[10] F. Soldovieri, R. Solimene, and G. Prisco, "A multiarray tomographic approach for through-wall imaging," *IEEE Trans. Geosci. Remote Sensing*, vol. 46, pp. 1192-1199, Apr. 2008.

[11] A. Franchois, A. Joisel, C. Pichot, and J. C. Bolomey, "Quantitative microwave imaging with a 2.45 GHz planar microwave camera," *IEEE Trans. Medical Imaging*, vol. 17, pp. 550-561, Aug. 1998.

[12] O. M. Bucci and T. Isernia, "Electromagnetic inverse scattering: retrievable information and measurement

strategies," *Radio Sci.*, vol. 32, pp. 2123-2138, Nov.-Dec. 1997.

[13] M. Bertero and P. Boccacci, *Introduction to Inverse Problems in Imaging*. IOP Publishing Ltd, Bristol, 1998.

[14] O. M. Bucci and G. Franceschetti, "On the spatial bandwidth of scattered fields," *IEEE Trans. Antennas Propagat.*, vol. 35, no. 12, pp. 1445-1455, Dec. 1987.

[15] T. Isernia, V. Pascazio, and R. Pierri, "On the local minima in a tomographic imaging technique," *IEEE Trans. Antennas Propagat.*, vol. 39, no. 7, pp. 1696-1607, Jul. 2001.

[16] O. M. Bucci, L. Crocco, T. Isernia, and V. Pascazio, "Subsurface inverse scattering problems: quantifying, qualifying, and achieving the available information," *IEEE Trans. Geosci. Remote Sensing*, vol. 39, pp. 2527-2537, Nov. 2001.

[17] E. L. Miller, and A. S. Willsky, "A multiscale, statistically based inversion scheme for linearized inverse scattering problems," *IEEE Trans. Antennas Propagat.*, vol. 34, no. 2, pp. 346-357, Mar. 1996.

[18] A. Baussard, E. L. Miller, and D. Lesselier, "Adaptive muliscale reconstruction of buried objects," *Inverse Problems*, vol. 20, pp. S1-S15, Dec. 2004.

[19] S. Caorsi, M. Donelli, and A. Massa, "Detection, location, and imaging of multiple scatterers by means of the iterative multiscaling method," *IEEE Trans. Microwave Theory Tech.*, vol. 52, no. 4, pp. 1217-1228, Apr. 2004.

[20] A. Litman, "Reconstruction by level sets of n-ary scattering obstacles," *Inverse Problems*, vol. 21, pp. S131-S152, Dec. 2005.

[21] S. Caorsi, A. Massa, M. Pastorino, and M. Donelli, "Improved microwave imaging procedure for nondestructive evaluations of two-dimensional structures," *IEEE Trans. Antennas Propagat.*, vol. 52, pp. 1386-1397, Jun. 2004.

[22] M. Benedetti, M. Donelli, and A. Massa, "Multicrack detection in two-dimensional structures by means of GA-based strategies," *IEEE Trans. Antennas Propagat.*, vol. 55, no. 1, pp. 205-215, Jan. 2007.

[23] V. Cingoski, N. Kowata, K. Kaneda, and H. Yamashita, "Inverse shape optimization using dynamically adjustable genetic algorithms," *IEEE Trans. Energ. Convers.*, vol. 14, no. 3, pp. 661-666, Sept. 1999.

[24] L. Lizzi, F. Viani, R. Azaro, and A. Massa, "Optimization of a spline-shaped UWB antenna by PSO," *IEEE Antenn. Wireless Propag. Lett.*, vol. 6, pp. 182-185, 2007.

[25] I. T. Rekanos, "Shape reconstruction of a perfectly conducting scatterer using differential evolution and particle

swarm optimization," *IEEE Trans. Geosci. Remote Sensing*, vol. 46, pp. 1967-1974, Jul. 2008.

[26] J. Cea, S. Garreau, P. Guillame, and M. Masmoudi, "The shape and topological optimizations connection," *Comput. Methods Appl. Mech. Eng.*, vol. 188, no. 4, pp. 713-726, 2000.

[27] G. R. Feijoo, A. A. Oberai, and P. M. Pinsky, "An application of shape optimization in the solution of inverse acoustic scattering problems," *Inverse Problems*, vol. 20, pp. 199-228, Feb. 2004.

[28] M. Masmoudi, J. Pommier, and B. Samet, "The topological asymptotic expansion for the Maxwell equations and some applications," *Inverse Problems*, vol. 21, pp. 547-564, Apr. 2005.

[29] S. Osher and J. A. Sethian, "Fronts propagating with curvature-dependent speed: algorithms based on Hamilton-Jacobi formulations," *J. Comput. Phys.*, 79, pp. 12-49, Nov. 1988.

[30] J. A. Sethian, *Level Set and Fast Marching Methods*. Cambridge University Press, Cambridge, UK, 2nd ed., 1999.

[31] F. Santosa, "A level-set approach for inverse problems involving obstacles," *ESAIM: COCV*, vol. 1, pp. 17-33, Jan. 1996.

[32] O. Dorn and D. Lesselier, "Level set methods for inverse scattering," *Inverse Problems*, vol. 22, pp. R67-R131, Aug. 2006.

[33] A. Litman, D. Lesselier, and F. Santosa, "Reconstruction of a two-dimensional binary obstacle by controlled evolution of a level-set," *Inverse Problems*, vol. 14, pp. 685-706, Jun. 1998.

[34] O. Dorn, E. L. Miller, C. M. Rappaport, "A shape reconstruction method for electromagnetic tomography using adjoint fields and level sets," *Inverse Problems*, vol. 16, pp. 1119-1156, May 2000.

[35] G. Franceschetti, *Electromagnetics: Theory, Techniques, and Engineering Paradigms*. Springer, New York, 1997.

[36] D. Colton and R. Kress, *Inverse Acoustic and Electromagnetic Scattering Theory*, 2nd Edition. Springer, Berlin, 1998.

[37] J. Sokolowski and J.-P. Zolésio, *Introduction to Shape Optimization: Shape Sensivity Analysis*, Springer Series in Computational Mathematics. Springer, Berlin, 1992.

[38] A. N. Tikhonov and V. Y. Arsenin, *Solutions of Ill-Posed Problems*. Winston/Wiley, Washington, 1977.

[39] J. H. Richmond, "Scattering by a dielectric cylinder of arbitrary cross-section shape," *IEEE Trans. Antennas Propagat.*, vol. 13, pp. 334-341, May 1965.

[40] D. T. Davis, J. N. Hwang, and L. Tsang, "Solving inverse problems using Bayesian modeling to incorporate information sources," *Proc. IEEE Int. Symp. Geosci. Remote Sensing*, pp. 1394-1396, 1994.

[41] P. M. van den Berg and R. E. Kleinman, "A contrast source inversion method," *Inverse Problems*, vol. 13, pp. 1607-1620, Dec. 1997.

[42] P. M. van den Berg and A. Abubakar, "Contrast source inversion method: state of art," *Progress In Electromagnetics Research*, vol 34, pp. 189-218, 2001.

[43] H. W. Engl and A. Neubauer, "Convergence rate for Tichonov regularization in finite dimensional subspaces of Hilbert scales," *Proc. Amer. Math. Soc.*, vol. 102, pp. 587-592, 1988.

[44] A. Abubakar, and P.M. Van den Berg, "Total variation as a multiplicative constraint for solving inverse problems," *IEEE Trans. Image Processing*, vol. 10, pp. 1384-1392, Sept. 2001.

[45] A. Abubakar, P.M. Vand den Berg, T.M. Habashy, and H. Braunisch, "A multiplicative regularization approach for deblurring problems," *IEEE Trans. Image Processing*, vol. 13, pp. 1524-1532, Nov. 2004.

[46] H. J. Kim, K. Choi, H. B. Lee, H. K. Jung, and S. Y. Hahn, "A new algorithm for solving ill conditioned linear

systems," *IEEE Trans. Magn.,* vol. 32, pp. 1373-1376, May 1996.

[47] V. Solo, "Limits to estimation in stochastic ill-conditioned inverse problems," *IEEE Trans. Information Theory,* vol 46, pp. 1872-1880, Aug. 2000.

[48] A. Neubauer, "Tikhonov regularization for nonlinear ill-posed problems: Optimal convergence rates and finite-dimensional approximation," *Inverse Problems*, vol. 5, pp. 541-557, 1989.

[49] J.-Y. Koo, "Optimal rates of convergence for nonparametric statistical inverse problems," *Ann. Statist.*, vol. 21, pp. 590-599, 1993.

[50] C. W. Groetsch, *The Theory of Tikhonov Regularization for Fredholm Equations of the First Kind.* London, U.K., Pitman, 1984.

[51] J. B. Keller, "Accuracy and validity of the Born and Rytov approximations," *J. Opt. Soc. Am. A*, vol. 59, pp. 1003-1004, 1969.

[52] F. Li, Q. H. Liu, and L.-P. Song, "Three-dimensional reconstruction of objects buried in layered media using Born and distorted Born iterative methods," *IEEE Geosci. Remote Sensing Lett.*, vol. 1, pp. 107-111, 2004.

[53] T. J. Cui, W. C. Chew, A. A. Aydiner, and S. Chen, "Inverse scattering of two-dimensional dielectric objects

buried in a lossy earth using the distorted Born iterative method," *IEEE Trans. Geosci. Remote Sensing*, vol. 39, pp. 339-346, 2001.

[54] R. E. Kleinman and P. M. van den Berg, "A modified gradient method for two-dimensional problems in tomography," *J. Computat. Appl. Math.*, vol. 42, pp. 17-35, Jan. 1992.

[55] H. Harada, D. J. N. Wall, T. T. Takenaka, and T. Tanaka, "Conjugate gradient method applied to inverse scattering problem," *IEEE Trans. Antennas Propagat.*, vol. 43, pp. 784-792, Aug. 1995.

[56] H. Gan and W. C. Chew, "A discrete BCG-FFT algorithm for solving 3D inhomogeneous scatterer problems," *Jour. Elec. Waves Appl.*, vol. 9, pp. 1339-1357, 1995.

[57] Z. Q. Zhang and Q. H. Liu, "Three-dimensional weak-form conjugate- and biconjugate-gradient FFT methods for volume integral equations," *Microwave Opt. Technol. Lett.*, Vol. 29, pp. 350-356, Jun. 2001.

[58] Z. Q. Zhang and Q. H. Liu, "Applications of the BiCGS-FFT method to 3-D induction well logging problems," *IEEE Geosci. Remote Sensing*, vol. 41, pp. 998-1004, May 2003.

[59] Y. Saad and M. H. Schultz, "GMRES: a generalized minimal residual algorithm for solving nonsymmetric linear

systems," *SIAM J. Sci. Stat. Comput.*, vol. 7, pp. 856-869, Jul. 1986.

[60] R. Freund and N. Nachtigal, "QMR: a quasi-minimal residual method for non-hermitian linear systems," *Numer. Math.*, vol. 60, pp. 315-339, 1991.

[61] L. Garnero, A. Franchois, J.-P. Hugonin, Ch. Pichot, and N. Joachimowicz, "Microwave imaging-complex permittivity reconstruction by simulated annealing," *IEEE Trans. Microwave Theory Tech.*, vol. 39, pp. 1801-1807, 1991.

[62] S. Caorsi, A. Massa, and M. Pastorino, "A computational technique based on a real-coded genetic algorithm for microwave imaging purposes," *IEEE Trans. Geosci. Remote Sensing*, vol. 38, pp. 1697-1708, Jul. 2000.

[63] A. Quing, L. K. Ching, and J. Lang, "Electromagnetic inverse scattering of two-dimensional perfectly conducting objects by real-coded genetic algorithm," *IEEE Trans. Geosci. Remote Sensing*, vol. 39, pp. 665-676, 200.

[64] S-Y. Yang, H-K. Choi, and J-W. Ra, "Reconstruction of a large and high-contrast penetrable object by using the genetic and Levenberg-Marquardt algorithms," *Microwave Opt. Technol. Lett.*, vol. 6, pp. 17-21, Sept. 1997.

[65] M. Donelli and A. Massa, "A computational approach based on a particle swarm optimizer for microwave imaging of two-dimensional dielectric scatterers," *IEEE*

Trans. Microwave Theory Tech., vol. 53, no. 5, pp. 1761-1776, 2004.

[66] R. L. Haupt and S. H. Haupt, *Practical genetic algorithms*, 2nd edition. Wiley-Interscience, New York, 2004.

[67] J. Kennedy, R. C. Eberhart, and Y. Shi, *Swarm Intelligence.* Morgan Kaufmann Publishers, San Francisco, 2001.

[68] J. R. Robinson and Y. Rahmat-Samii, "Particle swarm optimization in electromagnetics," *IEEE Trans. Antennas Propagat.*, vol. 52, pp. 771-778, Mar. 2004.

[69] S. Caorsi, G. L. Gragnani, and M. Pastorino, "An electromagnetic imaging approach using a multi-illumination technique," *IEEE Trans. Biomedical Eng.*, vol. 41, no. 4, pp. 406-409, 1994.

[70] S. Caorsi, G. L. Gragnani, and M. Pastorino, "A multiview microwave imaging system for two-dimensional penetrable objects," *IEEE Trans. Microwave Theory Techn.*, vol. 39, pp. 845-851, May 1991.

[71] D. Franceschini and A. Massa, "On the enhancement of the reconstruction accuracy obtained with a multisource/multi-illumination inverse scattering technique," *IEEE Antenn. Wireless Propag. Lett.*, vol. 4, pp. 194-197, 2005.

[72] W. C. Chew and J. H. Lin, "A Frequency-Hopping Approach for Microwave Imaging of Large Inhomogeneous Bodies," *IEEE Microwave Guided Wave Lett.*, vol. 5, pp. 439-441, Dec. 1995.

[73] S. Caorsi, G. L. Gragnani, M. Pastorino, and M. Rebagliati, "A model-driven approach to microwave diagnostics in biomedical applications," *IEEE Trans. Microwave Theory Tech.*, vol. 44, pp. 1910-1920, 1996.

[74] O. M. Bucci and G. Franceschetti, "On the degrees of freedom of scattered fields," *IEEE Trans. Antennas Propagat.*, vol. 37, pp. 918-926, Jul. 1989.

[75] J. G. Webster, *Electrical Impedance Tomography,* Adam Hilger, Bristol and New York, 1990.

[76] Q. Zhu, N.-G. Chen, and S. H. Kurtzman, "Imaging tumor angiogenesis by use of combined near-infrared diffusive light and ultrasound," *Optics Letters*, vol. 28, pp. 337-339, Mar. 2003.

[77] M. Molinari, S. J. Cox, B. H. Blott, and G. J. Daniell, "Adaptive mesh refinement techniques for electrical impedance tomography," *Physiological Measurement,* vol. 22, pp. 91-96, Feb. 2001.

[78] E. L. Miller, "Statistically based methods for anomaly characterization in images from observations of scattered fields," *IEEE Trans. Image Processing*, vol. 8, pp. 92-101, Jan. 1999.

[79] S. Caorsi, M. Donelli, D. Franceschini, and A. Massa, "A new methodology based on an iterative multiscaling for microwave imaging," *IEEE Trans. Microwave Theory Tech.*, vol. 51, app. 1162-1173, Apr. 2003.

[80] D. Franceschini, A. Rosani, M. Donelli, A. Massa, and M. Pastorino, "Morphological processing of electromagnetic scattering data for enhancing the reconstruction accuracy of the iterative multi-scaling approach," *Proc. IEEE Int. Work. Imaging Systems Tech.*, pp. 157-162, Apr. 2006.

[81] D. Franceschini, M. Donelli, R. Azaro, and A. Massa, "A robustness analysis of the iterative multi-scaling approach integrated with morphological operations," *Progress in Industrial Mathematics at ECMI 2006*, vol.12, pp. 126-139, Springer, 2007.

[82] P. Dubois, C. Dedeban, and J.-P. Zolésio, "Antenna's shape optimization and reconstruction by level-set 3D," *Proc. IEEE Int. Symp. Antennas Propag. Soc.*, pp. 581-584, Albuquerque, 2006.

[83] M. Benedetti, M. Donelli, G. Franceschini, M. Pastorino, and A. Massa, "Effective exploitation of the a-priori information through a microwave imaging procedure based on the SMW for NDE/NDT applications," *IEEE Trans. Geosci. Remote Sensing*, vol. 43, pp. 2584-2592, 2005.

[84] S. Osher and R. Fedkiw, *Level Set Methods and Dynamic Implicit Surfaces*. Springer, New York, 2003.

[85] M. Lien, I. Berre, and T. Mannseth, "Combined adaptive multiscale and level set parameter estimation," *Multiscale Model. Simul.*, vol. 4, pp. 1349-1372, 2006.

[86] I. Berre, M. Lien, and T. Mannseth, "A level-set corrector to an adaptive multiscale permeability prediction," *Comput. Geosci.*, vol. 11, pp. 27-42, Mar. 2007.

[87] K. van den Doel and U. M. Asher, "Dynamic level set regularization for large distributed parameter estimation problems," *Inverse Problems*, vol. 23, pp. 1271-1288, Jun. 2007.

[88] G. Sapiro, *Geometric Partial Differential Equations and Image Analysis*. Cambridge University Press, New York, 2001.

[89] S. Osher and N. Paragios, *Geometric Level Set Methods in Imaging, Vision and Graphics.* Springer, Berlin, 2003.

[90] J. C. Ye, Y. Bresler, and P. Moulin, "A self-referencing level-set method for image reconstruction from sparse Fourier samples," *International Journal of Computer Vision*, vol. 50, pp. 253-270, Nov. 2004.

[91] S. Garg, K. U. Kiran, R. Mohan, and U. S. Tiwary, "Multilevel medical image fusion using segmented image by level set evolution with region competition," *Proc. IEEE Int. Conf. Engineering in Medicine and Biology Society*, pp. 7680-7683, Shangai, 2005.

[92] M. Wasilewski, "Active contours using level sets for medical image segmentation," *http://www.cgl.uwaterloo.ca/~mmwasile/cs870.*

[93] R. L. Van Uitert and R. M. Summers, "Automatic correction of level set based subvoxel precise centerlines for virtual colonoscopy using the colon outer wall," *IEEE Trans. Medical Imaging*, vol. 26, pp. 1069-1078, Aug. 2007.

[94] E. T. Chung, T. F. Chan, X. C. Tai, "Electrical impedence tomography using level set representation and total variational regularization," *J. Comput. Phys.*, vol. 205, no. 2, pp. 707-723, May 2005.

[95] S. Leung and J. Qian, "Transmission traveltime tomography based on paraxial Liouville equations and level set formulations," *Inverse Problems*, vol. 23, pp. 799-821, Apr. 2007.

[96] K. Ito, K. Kunisch, and Z. Li, "Level-set approach to an inverse interface problem," *Inverse Problems*, vol. 17, pp. 1225-1242, Oct. 2001.

[97] C. Ramananjaona, M. Lambert, D. Lesselier, and J. P. Zolésio, "Shape reconstruction of buried obstacles by controlled evolution of a level-set: from a min-max formulation to a numerical experimentation," *Inverse Problems*, vol. 17, pp. 1087-1111, Dec. 2001.

[98] R. Ferrayé, J.-Y. Dauvignac, and C. Pichot, "An inverse scattering method based on contour deformations by means of a level set method using frequency hopping technique," *IEEE Trans. Antennas Propagat.*, vol. 51, no. 5, pp. 1100-1113, May 2003.

[99] O. Dorn and R. Villegas, "History matching of petroleum reservoirs using a level set technique," *Inverse Problems*, vol. 24, pp. 1-29, Jun. 2008.

[100] K. Belkebir and M. Saillard, "Testing inversion algorithms against experimental data," *Inverse Problems*, vol. 17, pp. 1565-1702, Dec. 2001.

[101] M. Testorf and M. Fiddy, "Imaging from real scattered field data using a linear spectral estimation technique," *Inverse Problems*, vol. 17, pp. 1645-1658, Dec. 2001.

[102] D. P. Huttenlocher, G. A. Klanderman, and W. J. Rucklidge, "Comparing images using the Hausdorff distance," *IEEE Trans. Pattern Analysis and Machine Intelligence*, vol. 15, pp. 850-863, Sep. 1993.

[103] D.-G. Sim, O.-K. Kwon, and R.-H. Park, "Object matching algorithms using robust Hausdorff distance measures," *IEEE Trans. Image Processing*, vol. 8, pp. 425-429, Mar. 1999.

[104] J. P. Bustos, F. Donoso, A. Guesalaga, and M. Torres, "Matching radar and satellite images for ship trajec-

tory estimation using the Hausdorff distance," *IET Radar Sonar Navigation*, vol. 1, pp. 50-58, Feb. 2007.

[105] P. Gastaldo and R. Zunino, "Hausdorff distance for robust and adaptive template selection in visual target detection," *Electron. Lett.*, vol. 38, pp. 1651-1653, Dec. 2002.

[106] J. Gomes and O. Faugeras, "Reconciling Distance Functions and Level Sets," *Scale-Space Theories in Computer Vision*, Lecture Notes in Computer Science. Springer, Berlin, 1999.

Appendix A

The Adjoint Problem

The adjoint field $\mathcal{F}^v(\underline{r})$ is defined by the following relationship

$$\begin{cases} \nabla^2\mathcal{F}^v(\underline{r}) - \kappa_C^2(\underline{r})\mathcal{F}^v(\underline{r}) = -\left[\widetilde{\xi}_{k_s}^v\left(\underline{r}_{m(v)}\right) - \xi_{k_s}^v\left(\underline{r}_{m(v)}\right)\right]^* \delta_{m(v)} \\ \qquad\qquad\qquad\qquad\qquad\qquad\qquad\qquad \underline{r} \in \Upsilon \\ \\ \nabla^2\mathcal{F}^v(\underline{r}) - \kappa_0^2(\underline{r})\mathcal{F}^v(\underline{r}) = 0 \\ \qquad\qquad\qquad\qquad\qquad\qquad\qquad\qquad \underline{r} \notin \Upsilon \end{cases} \tag{A.1}$$

where $\kappa_C(\underline{r}) = 2\pi f\sqrt{\mu_o\epsilon_o\left[\tau_C + 1\right]}$ is the wavenumber in the region inside the scatterer characterized by a contrast function τ_C, $\kappa_0(\underline{r}) = 2\pi f\sqrt{\mu_o\epsilon_o}$ is the free-space wavenumber, and $\delta_{m(v)}$ is the Kronecker delta, $m(v) = 1, ..., M(v)$, $v = 1, ..., V$. In order to determine $\mathcal{F}^v(\underline{r})$, let us consider the adjoint incident

field $\mathcal{I}^v(\underline{r})$ which is the solution of

$$\nabla^2\mathcal{I}^v(\underline{r}) - \kappa_0^2(\underline{r})\mathcal{I}^v(\underline{r}) = -\left[\widetilde{\xi}^v_{k_s}\left(\underline{r}_{m(v)}\right) - \xi^v_{k_s}\left(\underline{r}_{m(v)}\right)\right]^* \delta_{m(v)} \tag{A.2}$$

with $r_n \in D_I$. By assuming that $\mathcal{I}^v(\underline{r})$ satisfies the Sommerfeld radiation condition, namely

$$\lim_{|\underline{r}|\to+\infty} \sqrt{|\underline{r}|}\left(\frac{\partial\mathcal{I}^v(\underline{r})}{\partial|\underline{r}|} - j\kappa_0(\underline{r})\mathcal{I}^v(\underline{r})\right) = 0\,, \tag{A.3}$$

it can be determined by solving the following equation

$$\mathcal{I}^v(\underline{r}) = \sum_{m(v)=1}^{M(v)}\left[\widetilde{\xi}^v_{k_s}\left(\underline{r}_{m(v)}\right) - \xi^v_{k_s}\left(\underline{r}_{m(v)}\right)\right]^* G_{2D}\left(\underline{r}_{m(v)}/\underline{r}\right)$$

$$\underline{r}_{m(v)} \in D_O\,, \tag{A.4}$$

that can be achieved by replacing $\xi^v(\underline{r})$ with $\mathcal{I}^v(\underline{r})$ and $j\omega\mu_0 J^v(\underline{r})$ with the right member of (A.2) in equation (2.5). Consequently, $\mathcal{F}^v(\underline{r})$ is obtained by solving the following relationship

$$\mathcal{I}^v(\underline{r}) = \mathcal{F}^v(\underline{r}) - \left(\tfrac{2\pi}{\lambda}\right)^2 \int_{D_I} \tau(\underline{r}')\,\mathcal{F}^v(\underline{r}')\,G_{2D}(\underline{r}/\underline{r}')\,d\underline{r}'$$

$$\underline{r} \in D_I\,, \tag{A.5}$$

for a given $\tau(\underline{r})$, $\underline{r} \in D_I$.

Appendix B

Algorithms

B.1 The Edge Detection Operator $\partial(\cdot)$

Let us consider a contrast function τ defined in the investigation domain D_I by the following relationship

$$\tau\left(\underline{r}_n\right) = \begin{cases} \left(\epsilon_C - 1\right) - j\frac{\sigma_C}{2\pi f \varepsilon_0} & \underline{r}_n \in \Upsilon \\ 0 & \text{otherwise} \end{cases} \qquad n = 1, ..., N \tag{B.1}$$

where Υ is the shape of a scatterer located in D_I and characterized by the permettivity ϵ_C and the conductivity σ_C. In order to retrieve the contour of the shape Υ, the function $\tau^B\left(\underline{r}_n\right)$ is

computed as follows

$$\tau^B\left(\underline{r}_n\right) = \partial\left[\tau\left(\underline{r}_n\right)\right] =$$

$$= \begin{cases} \left\lceil 1 - \frac{\sum_{p=n-1}^{n+1}\sum_{b=n-1}^{n+1}\tau(x_p,y_b)}{9\tau_C} \right\rceil & \tau\left(x_n,\, y_n\right) = \tau_C \\ \\ 0 & \text{otherwise} \end{cases} \tag{B.2}$$

where $\lceil\cdot\rceil$ is the ceiling function

$$\lceil\upsilon\rceil = \min\left\{\varsigma \in \mathbb{Z} \,|\, \upsilon \leq \varsigma\right\} \tag{B.3}$$

and

$$\tau_C = (\epsilon_C - 1) - j\frac{\sigma_C}{2\pi f \varepsilon_0} \tag{B.4}$$

More in detail, $\tau^B\left(\underline{r}_n\right) = 1$ only when $\underline{r}_n$ is a border subdomain of Υ. Such pixels are then grouped in a set Π defined as

$$\Pi := \left\{\underline{r}_n^B = \left(x_n^B,\, y_n^B\right) \,|\, \tau^B\left(\underline{r}_n^B\right) = 1\right\}. \tag{B.5}$$

B.2 How to Count the Number of Objects

Let us consider a contrast function τ, the set of contour subdomains, $\Pi := \left\{\underline{r}_n^B = \left(x_n^B,\, y_n^B\right) \,|\, \tau^B\left(\underline{r}_n^B\right) = 1\right\}$, and the $\mathcal{N}_{seeds}$ "seeds" $\underline{r}_i^E$, $i = 1, ..., \mathcal{N}_{seeds}$. τ^B and τ^E can be achieved by means of the operators $\partial(\cdot)$ and *erosion*, respectively. The

number of objects in the reconstruction can be estimated according to the pseudo-code lines reported in Alg. 1 and in Alg. 2. More in detail, the program described in Alg. 1 returns the number of regions Q in the contrast function τ. If the objects are separated enough from each other, then Q is equal to the number of objects.

Algorithm 1 Pseudo-code lines describing how the number of objects in a reconstruction τ is counted.

function $Q = \text{count-the-number-of-objects}\left(\tau^B, \tau^E\right)$

$i = 1$
$\mathcal{M} = \mathcal{N}_{seeds}$
while $i < \mathcal{M}$
  $\Sigma_i = \text{walk-along-}\tau^B\text{-starting-from}\left(\underline{r}_i^E\right)$
  if there are other seeds $\underline{r}_j^E$
      $j = 1, ..., i-1, i+1, ..., \mathcal{N}_{seeds}$, in the set Σ_i **then**
    remove those seeds from the set Σ_i
    update $\mathcal{M}$
  endif
  find the region R_i that holds Σ_i
  $i = i + 1$
end
while $i < \mathcal{M}$
  if R_i is overlapping other regions **then**
    redefine R_i
    update $\mathcal{M}$
  endif
  $i = i + 1$
end

return $\mathcal{M}$

Algorithm 2 Pseudo-code lines describing the function "walk-along-τ^B-starting-from$\left(\underline{r}_i^E\right)$".

function Σ = walk-along-τ^B-starting-from $\left(\underline{r}^E\right)$

find the seed $\underline{r}^E$ in the set Π
define the first pixel $\underline{r}_{i=1}^{\Sigma}$ of the boundary Σ as $\underline{r}_{i=1}^{\Sigma} = \underline{r}^E$
$i = 2$
while T = TRUE
  find the adjacent pixel $\underline{r}_i^{\Sigma}$ such that $\tau^B\left(\underline{r}_i^{\Sigma}\right) = 1$
  if $\underline{r}_i^{\Sigma} \notin \Sigma$ **then**
    add $\underline{r}_i^{\Sigma}$ to Σ
  else
    T = FALSE
  endif
  $i = i + 1$
end

return Σ